

3-2020

Piezoelectric Energy Harvesting Suspension System for a Half Car Model: Analytical and Experimental Study

Doaa Ali Nasser Al-Yafeai

Follow this and additional works at: https://scholarworks.uaeu.ac.ae/mechan_theses



Part of the [Mechanical Engineering Commons](#)

Recommended Citation

Al-Yafeai, Doaa Ali Nasser, "Piezoelectric Energy Harvesting Suspension System for a Half Car Model: Analytical and Experimental Study" (2020). *Mechanical Engineering Theses*. 8.
https://scholarworks.uaeu.ac.ae/mechan_theses/8

This Thesis is brought to you for free and open access by the Mechanical Engineering at Scholarworks@UAEU. It has been accepted for inclusion in Mechanical Engineering Theses by an authorized administrator of Scholarworks@UAEU. For more information, please contact fadl.musa@uaeu.ac.ae.

United Arab Emirates University

College of Engineering

Department of Mechanical Engineering

PIEZOELECTRIC ENERGY HARVESTING SUSPENSION SYSTEM
FOR A HALF CAR MODEL: ANALYTICAL AND EXPERIMENTAL
STUDY

Doaa Ali Nasser Al-Yafeai

This thesis is submitted in partial fulfilment of the requirements for the degree of
Master of Science in Mechanical Engineering

Under the Supervision of Dr. Tariq Darabseh

March 2020

Declaration of Original Work

I, Doaa Ali Nasser Al-Yafeai, the undersigned, a graduate student at the United Arab Emirates University (UAEU), and the author of this thesis entitled “*Piezoelectric Energy Harvesting Suspension System for a Half Car Model: Analytical and Experimental Study*”, hereby, solemnly declare that this thesis is my own original research work that has been done and prepared by me under the supervision of Dr. Tariq Darabseh, in the College of Engineering at UAEU. This work has not previously been presented or published, or formed the basis for the award of any academic degree, diploma or a similar title at this or any other university. Any materials borrowed from other sources (whether published or unpublished) and relied upon or included in my thesis have been properly cited and acknowledged in accordance with appropriate academic conventions. I further declare that there is no potential conflict of interest with respect to the research, data collection, authorship, presentation and/or publication of this thesis.

Student's Signature:  _____

Date: 09/04/2020

Copyright © 2020 Doaa Ali Nasser Al-Yafeai
All Rights Reserved

Advisory Committee

1) Advisor: Dr. Tariq Darabseh

Title: Associate Professor

Department of Mechanical Engineering

College of Engineering

2) Co-advisor: Prof. Abdel-Hamid I. Mourad

Title: Professor

Department of Mechanical Engineering

College of Engineering

Approval of the Master Thesis

This Master Thesis is approved by the following Examining Committee Members:

- 1) Advisor (Committee Chair): Dr. Tariq Darabseh

Title: Associate Professor

Department of Mechanical Engineering

College of Engineering

Signature Tariq Darabseh

Date April 12, 2020

- 2) Member: Dr. Farag Omar

Title: Associate Professor

Department of Mechanical Engineering

College of Engineering

Signature Farag Omar

Date 12/4/2020

- 3) Member (External Examiner): Dr. Peter Glynne-Jones

Title: Associate Professor

Department of Mechanical Engineering

Institution: University of Southampton, United Kingdom

Signature Tariq Darabseh

Date April 12, 2020

This Master Thesis is accepted by:

Dean of the College of Engineering: Professor Sabah Alkass

Signature Sabah Date 15/4/2020

Dean of the College of Graduate Studies: Professor Ali Al-Marzouqi

Signature Ali Hassan Date 15/4/2020

Copy ____ of ____

Abstract

One of the essential techniques for energy harvesting is the clean energy collection from ambient vibration. Recently, piezoelectric energy harvesting systems became a hot topic and attracted many researchers. This is due to their simple structure, relatively high output power among the other mechanisms (electromagnetic and electrostatic), compatibility with MEMS, and operation in a wide frequency range. The main objective of the current work is to develop a mathematical model to evaluate the potential of harvesting power from the car suspension system. Quarter and half car models with a built-in piezoelectric stack were modeled mathematically using Laplace transformation and simulated using MATLAB/Simulink. The piezoelectric stack was installed in series with the suspension spring to maintain the performance of the original suspension system in ride quality and comfortability. The harvested voltage and power were tested in both time and frequency domain approaches. The results from a quarter car model showed that, the maximum generated voltage and power under harmonic excitation with an acceleration amplitude of 0.5 g and frequency of 1.46 Hz were 19.11 V and 36.74 mW, respectively. By comparing the quarter car model with a half car model, the results illustrated that the output voltage and power of the half car models were increased to 33.56 V and 56.35 mW (75.6% and 53.4%), respectively. Furthermore, the quarter and half car models were subjected to random excitation and tested under three different road classes (A, C, and H). The findings confirmed that the harvested voltage and power were increased with the road roughness levels and car velocity. From very smooth to very rough road levels, the harvested power was increased by 434 mW for quarter car model and 537 mW for half car model. The influence of the different parameters of the piezoelectric stack (number

of stack layers and area to thickness) and car suspension (sprung and unsprung stiffness, damping coefficients, and masses) were examined for half car model subjected to harmonic excitation. Also, the effect of road amplitude unevenness was considered. The analytical results of the quarter car model were verified with the experimental test under harmonic excitation. The results exhibited good agreement with the analytical results at different excitation frequencies (0 – 25 Hz). A significant contribution of this work is developing a half car model with a built-in piezoelectric stack. The findings of this work illustrated that there is a significant potential for harvesting energy from the car suspension system. This energy could be utilized in different ways. The study will encourage automobile manufacturers to develop and produce cars that are equipped with multiple energy harvesters to make the dissipated energy available for utilization. Such utilization of regenerated energy improves the fuel efficiency and the economy significantly.

Keywords: Energy harvesting, piezoelectric stack method, car suspension system, half car model, analytical modelling, experimental analysis.

Title and Abstract (in Arabic)

حصاد الطاقة الكهروضغطية من نظام التعليق لنموذج نصف سيارة: دراسة تحليلية وتجريبية.

الملخص

واحدة من التقنيات الأساسية لجمع الطاقة هي جمع الطاقة النظيفة من الاهتزازات المحيطة. في الآونة الأخيرة، أصبحت أنظمة حصاد الطاقة كهروضغطية (Piezoelectric) موضوعاً هاماً وجذبت العديد من الباحثين ويرجع ذلك إلى هيكلها البسيط، والطاقة الإنتاجية العالية نسبياً بين الآليات الأخرى (الكهرومغناطيسية والكهروستاتيكية) (Electromagnetic and electrostatic)، والتوافق مع الأنظمة الكهروميكانيكية الصغرى، والتشغيل في نطاق تردد واسع. الهدف الرئيسي من العمل الحالي هو تطوير نموذج رياضي لتقييم إمكانات حصاد الطاقة من نظام تعليق السيارة. تم تصميم نماذج ربع ونصف سيارة التي تحتوي على مجموعة كهروضغطية مدمجة بطريقة رياضية باستخدام تحويل لابلاس (Laplace) وتمت محاكاتها باستخدام برنامج ماتلاب/سمولينك (MATLAB/Simulink). تم تثبيت مجموعة كهروضغطية بالتوالي مع زنبرك التعليق للحفاظ على أداء نظام التعليق في جودة الركوب والراحة. تم اختبار الجهد والقدرة المحصورة من كل نموذج في المجال الزمني والتردد. أوضحت النتائج التي توصل إليها نموذج ربع السيارة أن الحد الأقصى للجهد المتولد والطاقة تحت الحركة التوافقية بمعدل تسارع 0.5 من الجاذبية الأرضية (0.5 g) وتردد 1.46 هرتز (1.46 Hz) كانت 19.11 فولت (19.11 V) و36.74 ميلي واط (36.74 mW) التوالي. بمقارنة نموذج ربع سيارة بنموذج سيارة نصف، أوضحت النتائج أن الجهد الناتج والطاقة لنموذج نصف سيارة زاد إلى 33.56 فولت (33.56 V) و56.35 ميلي واط (56.35 mW)، على التوالي. علاوة على ذلك، تعرضت نماذج ربع ونصف سيارة لإثارة عشوائية وتم اختبارها تحت

ثلاث فئات طرق مختلفة (A و C و H). أكدت النتائج أن الجهد والطاقة التي تم حصادها زادت مع مستويات خشونة الطريق وسرعة السيارة. من مستويات الطرق شديدة السلاسة إلى مستويات الطرق الوعرة للغاية، تم زيادة الطاقة المحصودة بمقدار 434 ميلي واط (434 mW) لنموذج ربع سيارة و 537 ميلي واط (537 mW) لنموذج نصف سيارة. تم فحص تأثير المعاملات المختلفة لمجموعة الكهروضغطية (عدد الطبقات ونسبة المساحة إلى السمك) ونظام تعليق السيارة (معامل الصلابة، معامل التخميد، الكتلة) لنموذج نصف سيارة تحت تأثير الحركة التوافقية. أيضا، تم النظر في مدى تأثير ارتفاع موجة الطريق على حصاد الجهد والطاقة. تم التحقق من النتائج التحليلية لنموذج ربع سيارة بإجراء اختبار تجريبي تحت الإثارة التوافقية. أظهرت النتائج اتفاق جيد مع النتائج التحليلية تحت تأثير ترددات مختلفة (0 - 25 هرتز). المساهمة المهمة من عملنا هي تصميم نموذج نصف سيارة يحتوي على مجموعة كهروضغطية مدمجة. وضحت نتائج هذا العمل أن هناك إمكانية كبيرة لحصد الطاقة من نظام تعليق السيارة. يمكن استخدام هذه الطاقة بطرق مختلفة. على سبيل المثال، ستشجع الدراسة شركات صناعة السيارات على تطوير وإنتاج المركبات المزودة بحصادات الطاقة المتعددة. هذا الاستخدام للطاقة المتجددة سيحسن من كفاءة استهلاك الوقود والاقتصاد بشكل كبير.

مفاهيم البحث الرئيسية: حصاد الطاقة، طريقة الكهروضغطية، نظام تعليق السيارة، نموذج نصف السيارة، التحليل النظري، التحليل التجريبي.

Acknowledgements

I would like to express my appreciation to all of whom supported me in completing this master thesis. A special thanks and gratitude go to my main advisor Dr. Tariq Darabseh, and co-advisor Prof. Abdel-Hamid I. Mourad from Mechanical Engineering Department for their valuable guidance, encouragement, and unlimited support. Without their knowledge, experience, and endless ideas, this work would not have been possible. It was a great honor to work under their supervision.

I would like to give thanks the lab members, Eng. Abdul Rahman Mohamed, and Eng. Muthanna A. Aziz from the Mechanical Engineering Department, for their assistance in conducting the experimental work. I would extend my thanks to the Eng. Ahmed Abd-Rabou from the Electrical Engineering Department for his assistant in conducting the electrical part of the experiment.

My sincere thanks to all my friends for their continued encouragement and advice. A special thanks go to my best friend, Eng. Mai Rabie, who supported me morally, psychologically, and emotionally throughout my master years.

Finally, I owe heartfelt thanks to my parents, my lovely sisters and brothers for their consistent support, understanding, and motivation. Their passionate encouragement was a great help during all the phases of this thesis. I always knew that they believed in me and wanted the best for me.

Dedication

To my beloved parents. The reason of what I become today.

Table of Contents

Title	i
Declaration of Original Work	ii
Copyright	iii
Advisory Committee	iv
Approval of the Master Thesis	v
Abstract	vii
Title and Abstract (in Arabic)	ix
Acknowledgements	xi
Dedication	xii
Table of Contents	xiii
List of Tables.....	xv
List of Figures	xvi
List of Abbreviations.....	xvi
List of Symbols	xxii
Chapter 1: Introduction	1
1.1 Motivation	1
1.2 Statement of the problem	1
1.3 Objectives.....	3
1.4 Thesis structure	4
Chapter 2: Literature Review	5
2.1 Background	5
2.2 Piezoelectric material	9
2.2.1 Piezoelectric characteristics	9
2.2.2 Piezoelectric different configurations	13
2.3 Energy harvesting from different vibrations	16
2.4 Car suspension system	21
2.4.1 Mathematical car models	21
2.4.2 Energy harvesting from car suspension system	31
2.5 Electronic circuit of piezoelectric harvesting system.....	47
2.6 Utilization of the harvested energy	50
Chapter 3: Mathematical Models	52
3.1 Mathematical models without piezoelectric stack	52
3.1.1 Quarter car model (QCM)	52
3.1.2 Half car model (HCM)	53
3.2 Mathematical models with piezoelectric stack	55

3.2.1 Piezoelectric stack model	55
3.2.2 Quarter car model (QCM) with PZT stack.....	59
3.2.3 Half car model (HCM) with PZT stack.....	62
Chapter 4: Experimental Setup	70
4.1 Quarter car model with piezoelectric stack	70
4.2 Vibration source input.....	72
4.3 Data acquisition system.....	73
4.4 Electrical circuit	73
Chapter 5: Results and Discussions	75
5.1 Analytical results.....	75
5.1.1 Quarter vs. half car models	75
5.1.2 Effect of different parameters on the HCM	101
5.2 Experimental results	110
Chapter 6: Conclusion and Recommendations	115
6.1 Conclusion	115
6.2 Recommendations for future studies.....	118
References	119
List of Publications	139

List of Tables

Table 1: Power density of different energy sources	5
Table 2: Advantages and disadvantages of the conversion mechanisms	8
Table 3: Comparison of 31 and 33 modes	15
Table 4: Harvested power from human motion	17
Table 5: Levels of acceptability of ride quality	29
Table 6: Different energy harvesting of CSS with their specifications and important outcomes	44
Table 7: Piezoelectric parameters.	58
Table 8: Piezoelectric stack material properties.....	72
Table 9: Parameters used in the mathematical model of the quarter and half car suspension systems.....	77
Table 10: Natural frequencies of QCM and HCM.....	79
Table 11: Road roughness level according to ISO 8608.....	92
Table 12: Summarized results for quarter and half car models	101
Table 13: Suspension parameters used in the experiment.	111

List of Figures

Figure 1: Power density vs. voltage of different energy harvesting mechanisms.....	7
Figure 2: Energy harvesting from different mechanical systems and its applications.....	9
Figure 3: Direction of polarization for a piezoelectric material.....	11
Figure 4: Modes of a piezoelectric material.....	12
Figure 5: Different configuration of bimorph and unimorph.....	15
Figure 6: Two methods of harvesting energy from the shoe PVDF under the ball foot and PZT materials under the heel.....	17
Figure 7: Power-generating floor at Tokyo Station's Marunouchi North Exit.....	18
Figure 8: Energy harvester from road traffic.	20
Figure 9: Two DOF model.....	23
Figure 10: Different experimental setups of QCM as real tires.	24
Figure 11: Different experimental setups of QCM as moving plates.	25
Figure 12: Four DOF model.....	27
Figure 13: Different experimental setups of HCM.	28
Figure 14: Four DOF model.....	29
Figure 15: QCM with built in piezoelectric material in parallel connection.	32
Figure 16: HCM with built in piezoelectric material in parallel connection.	33
Figure 17: QCM with built in piezoelectric material in series connection.	34
Figure 18: Dual mass piezoelectric bar harvester of QCM.....	35
Figure 19: Car suspension with piezoelectric cantilever beam.....	36
Figure 20: Three piezoelectric materials located on the tire.	36
Figure 21: A nanogenerator NG in the inner surface of the tire.	37
Figure 22: Energy harvester at the center of the tire..	38
Figure 23: A piezoelectric material inside the tire surface at the right-hand side and its voltage converter circuit at the left-hand side.	39
Figure 24: Three different piezoelectric energy harvesters.....	39
Figure 25: Piezoelectric material on the shock absorber.	40
Figure 26: Energy harvesting system of piezoelectric vibration absorber.....	41

Figure 27: Piezoelectric stack inside the shock absorber tube.	42
Figure 28: QCM with ML PZT VEH mechanism.	43
Figure 29: Schematic of battery charging circuit.	47
Figure 30: Piezoelectric energy harvesting system.	50
Figure 31: Quarter car model (QCM).	53
Figure 32: Half car model (HCM).	55
Figure 33: Equivalent stiffness in different connections.	56
Figure 34: Piezoelectric energy harvesting circuit.	57
Figure 35: Equivalent electric circuit.	59
Figure 36: QCM with PZT stack.	62
Figure 37: HCM with PZT stack.	69
Figure 38: Experimental setup of QCM with piezoelectric stack.	70
Figure 39: QCM attached to the shaker.	71
Figure 40: Vibration source input.	72
Figure 41: LABVIEW program used in the experiment.	73
Figure 42: Electrical circuit connection.	74
Figure 43: Simulation scheme for the energy harvesting models.	76
Figure 44: Displacement ratio of sprung and unsprung masses with respect to the input displacement in frequency domain for QCM.	78
Figure 45: Displacement ratio of sprung and unsprung masses with respect to the input displacement in frequency domain for HCM.	78
Figure 46: The variation of the average dissipated power by the suspension damper for QCM in the frequency domain.	80
Figure 47: The variation of the average dissipated power by the suspension damper for HCM in the frequency domain.	81
Figure 48: The variation of the average dissipated power by the suspension damper for QCM in different car velocities.	82
Figure 49: The variation of the average dissipated power by the suspension damper for HCM in different car velocities.	83
Figure 50: Harvested voltage and power in the time domain for QCM.	84
Figure 51: Harvested voltage and power in the time domain for HCM.	85
Figure 52: Harvested voltage and power in the frequency domain for QCM.	86
Figure 53: Harvested voltage and power in the frequency domain for HCM.	87

Figure 54: Harvested voltage and power at different car velocities for QCM.....	88
Figure 55: Harvested voltage and power at different car velocities for HCM.....	88
Figure 56: Harvested voltage and power in different car velocities at the non-resonance frequency for QCM.....	89
Figure 57: Harvested voltage and power in different car velocities at the non-resonance frequency for HCM.....	90
Figure 58: Simulation scheme for road roughness input.	93
Figure 59: Road roughness signals.	94
Figure 60: Harvested voltage and power on a road of class A for both QCM and HCM.	96
Figure 61: Harvested voltage and power on a road of class C for both QCM and HCM.	97
Figure 62: Harvested voltage and power on a road of class H for both QCM and HCMs.	98
Figure 63: Harvested voltage and power on a road of class C for QCM with different car velocities.	99
Figure 64: Harvested voltage and power on a road of class C for HCM with different car velocities.	100
Figure 65: Harvested voltage and power vs. different amplitudes of road unevenness at excitation frequency of 1.46 Hz.	102
Figure 66: The effect of the number of layers of the piezoelectric stack on the harvested power.	103
Figure 67: The effect of area/thickness ratio of the piezoelectric stack on the harvested power.	104
Figure 68: Effect of the sprung stiffness coefficient on the harvested power.	105
Figure 69: Effect of the unsprung stiffness coefficient on the harvested power.	105
Figure 70: Effect of the sprung and unsprung stiffness coefficient on the output sprung resonant frequency and power.	106
Figure 71: Effect of the sprung damping coefficient on the harvested power.	107

Figure 72: Effect of the unsprung damping coefficient on the harvested power.	107
Figure 73: Effect of the sprung/unsprung damping coefficient on the output sprung resonant frequency and power.	108
Figure 74: Effect of the sprung mass on the harvested power.	109
Figure 75: Effect of the unsprung mass on the harvested power.	109
Figure 76: Effect of the sprung and unsprung masses on the output sprung resonant frequency and power.....	110
Figure 77: Sprung and unsprung resonant frequencies.	112
Figure 78: Input road acceleration at 0.05 g.	112
Figure 79: The analytical and experimental voltage in frequency domain for QCM.	113
Figure 80: The magnified experimental output voltage and power in frequency domain.	114

List of Abbreviations

AC	Alternating Current
BaTiO ₃	Barium Titanate
CSS	Car Suspension system
DAQ	Data Acquisition System
DC	Direct Current
DOF	Degree of Freedom
FCM	Full Car Model
HCM	Half Car Model
IDE	Interdigitate Electrode
ISO	International Organization for Standardization
LED	Light Emitting Diode
MEMS	Micro-Electro-Mechanical Systems
ML PZT VEH	Multilayer Piezoelectric Vibration Energy Harvesting
PMMA	Poly(methyl methacrylate)
PSD	Power Spectral Density
PVDF	Polyvinylidene Fluoride

PZT	Lead Zirconate Titanate
QCM	Quarter Car Model
RMS	Root Mean Square

List of Symbols

English symbols:

A	Surface Area (m^2)
a	Amplitude (m)
b	Damping Coefficient (N.s/m)
C	Capacitor (F)
d_{33}	Strain Coefficient (m/V)
E	Young's Modulus (N/m^2)
e	Electric Field (N/C)
F	Force (N)
f	Natural Frequency (Hz)
G	Road Roughness Coefficient (m^2/m^{-1})
h	Thickness (m)
I	Moment of Inertia (kg.m^2)
i	Current (A)
K	Spring Coefficient (N/m)
k	Electromechanical Coupling Coefficient
L	Wheelbase (m)

l	Total Length (m)
M	Mass (kg)
N	Number of Layers
n	Spatial Frequency (m^{-1})
P	Power (W)
Q	Electric Charge (C)
R	Resistor (Ω)
S	Strain (m/m)
t	Time (s)
u	Car Velocity (m/s)
V	Voltage (V)
W	Waviness
w	Gaussian White Noise
Y	Vertical Displacement (m)

Greek symbols:

α	Force Factor (N/V)
ϵ_{33}	Dielectric Permittivity (F/m)
λ	Wavelength (m)

ω	Angular Frequency (rad/s)
ρ	Density (g/cm ³)
σ	Stress (N)
τ	Time Delay(s)
θ	Angular Displacement (rad)

Subscripts:

avg	Average
e	External
f	Front
p	Piezoelectric
R	Road
r	Rear
s	Sprung
us	Unsprung

Chapter 1: Introduction

1.1 Motivation

Over the last decade, green manufacturing has been attracted a great deal of attention in the worldwide. Different types of renewable energy could replace the use of traditional fossil fuel that harms both environment and public health [1], [2]. For instance, the use of petroleum as a fuel for transportation causes global warming from the emissions of carbon dioxide. Achieving clean energy could be attained through scavenging the waste energy from the ambient environment and converting it into useful energy. This technology is also used in the field of powering wireless sensors to avoid the use of conventional batteries which are needed to be periodically replaced or recharged. The electrical energy for running different types of devices could be obtained from various potential energy available in the ambient environment as for example the solar energy [3]–[5], thermal energy [6]–[8], mechanical vibration energy [9]–[11] like wind energy [12], [13], acoustic energy [14]–[16] and ocean waves [17]–[19]. Harvesting these energies will help in providing infinite lifetime energy of power generation. Currently, most automobiles have a large number of sensors where batteries are preferred to be replaced by different energy harvesting techniques. These energy harvesters could scavenge the dissipated energy from the car suspension system (CSS) and convert it to useful energy.

1.2 Statement of the problem

In 2018, the Energy Information Administration (EIA) stated that there is about 92% of petroleum products consumed for the transportation sector, while only 10 – 20% is utilized to drive the cars [20], [21]. The car suspension system (CSS) is an

essential component in automobiles, yet it is the primary source of energy dissipation due to the dampening of vibrations. Velinsky and White [22] reported that this dissipated power is affected by different factors such as the road profile, car speed, and car parameters such as the car mass, spring stiffness, and damper coefficients. Wei and Taghavifar [23] showed that, the power dissipated by the front CSS was approximately 35% higher than the rear suspension due to greater values of the mass, spring, and damper of the front suspension than the rear one. Also, Jacota [24] stated that, increasing the mass of the car as well as the damping coefficient corroborated by decreasing the stiffness coefficient will provide higher dissipation energy for the dampers.

Furthermore, the road profile affects the amount of energy dissipated from the suspension system, as shown in the references [23], [24]. According to Abdelkareem et al. [25], the traditional shock absorber at a speed of 20 - 50 km/h with no bumps road can dissipate power in a range of 10 - 90 W. While having at least one bump will increase the power dissipation to 40 - 140 W at the same speed. On a weak road profile, Segel and Lu [26] indicated that about 200 W was dissipated from the four dampers of a passenger car at a speed of 13 m/s. Wei and Taghavifar [23] studied the possible energy harvesting from the CSS through different road profiles. For instance, in the harmonic excitation, the greatest average power of 57.84 W was recorded at the car speed of 13 km/h and 39 km/h. While in the random excitation, different road surfaces were categorized based on the power spectral density function. The various road surfaces are categorized in the smooth runway, rough runway, smooth highway, and highway with gravel. They reported that, the predicted power dissipation from the highway with gravels was recorded as 2000 W while, in the smooth highway, the dissipated power was around 200 W. This huge difference was due to the high relative

velocity of the suspension system (2 m/s) for the highway with gravel compared to the smooth road (0.75 m/s). According to Jacota [24], the road profile was divided into two categories, macrostructure, and microstructure. The macrostructure is the longitudinal profile of the road, which is categorized when the car has a speed in the range of 25 – 120 km/h. While the microstructure represents the uneven humps of tread, which is felt by the car passengers. He concluded that, the microstructure road profile has the most significant impact on the suspension excitation which dissipates more energy. These previously mentioned results indicate that, this amount of dissipated power should not be ignored. Accordingly, the work aims to evaluate the energy that can be harvested from the mechanical vibrations of CSS and the possibility of converting it into useful energy.

1.3 Objectives

The main objectives of this work are firstly to build both analytical and experimental models in order to evaluate the possible harvested energy from the car suspension system. Secondly, to conduct a comparison between these two different models and thirdly, to study the effect of different parameters on the harvested voltage and power.

To accomplish the above objectives, the piezoelectric stack harvester will be installed in series with the suspension springs in order to harvest the dissipated power. The equations of motion for different car models (quarter and half) will be derived mathematically using Laplace transformation. Piezoelectric energy harvesting system for a quarter and half car models will be modelled through MATLAB/Simulink. The harvested voltage and power from the piezoelectric stack will be studied in time and frequency domains. The investigation will be extended to study the influence of the

car parameters (mass, stiffness coefficient, and damping coefficient) as well as the piezoelectric parameters (area, thickness, and number of layers) on the output harvested power. The car suspension system will be subjected to and tested under harmonic and random excitation inputs. Finally, the experimental study will be carried out in order to verify the analytical results.

1.4 Thesis structure

The thesis is divided into six chapters, including this introduction with its motivation, problem statement and objectives (chapter 1). The literature of different existing vibrational applications utilizing piezoelectric energy harvesting techniques as well as a state of art review of car suspension-based piezoelectric energy harvesting systems are presented in chapter 2. In chapter 3, a detailed mathematical derivation of the quarter and half car systems without and with piezoelectric stacks using Laplace transformation method are discussed. The experimental setup of the quarter car model used in this work is described in chapter 4. The analytical and experimental results of the harvested voltage and power from car suspension models are found in chapter 5. The chapter also illustrates a parametric study of a half car model under harmonic excitation. Finally, the findings obtained from this study along with some recommendations proposed for future are dedicated in chapter 6.

Chapter 2: Literature Review

2.1 Background

Many research works were conducted in reviewing several energy harvesting technologies [27]–[34]. The results summarized in Table 1 shows that, solar power provides the most significant power density in direct sunlight. However, this energy is an unsuitable source of energy for indoor environments. Mechanical vibration through the piezoelectric element is the most appropriate alternative source of energy harvesting due to their availability in many different environments.

Table 1: Power density of different energy sources [27], [28].

Energy source	Power density ($\mu\text{W}/\text{cm}^3$)
Solar (outdoors)	15,000 - direct sun, 150 - cloudy day
Solar (indoors)	6 - office desk
Vibrations (piezoelectric conversion)	250
Vibrations (electrostatic conversion)	50
Acoustic noise	0.003 at 75 dB, 0.96 at 100 dB
Temperature gradient	15 at 10°C gradient

One of the most effective methods of implementing a power harvesting system is to utilize the strain energy from various mechanical vibrations. There are different types of mechanical vibrations existing in the environment like vibrating structures, moving objects, or vibration induced by fluid flow. A significant amount of energy is dissipated in the ambient vibrations in several forms like heat, and friction. Harvesting these dissipated energies into useful electrical energy could be through different methods, including the use of piezoelectric material, electromagnetic, and electrostatic transducer. All the proposed methods could provide a significant amount of useful

energy, while piezoelectric materials received the most attention from many researchers in the last decade. The reason behind this attention is that, the piezoelectric materials have an ability to directly transfer the applied stress into electrical energy with ease implementation into the system. Further, it can be easily fabricated with multiple structures due to its simple and flexible configuration without requiring any additional tools.

The piezoelectric transducer is the most effective and preferable method, and it produces the highest power density, and operates in the full frequency ranges [29], [35]–[37]. Priya [35] stated that the generated power density of the piezoelectric transduction was more than three times greater than the other two transductions. Different researchers reported the value of the maximum harvested power density. Jeon et al. [38] found that the highest power density from a thin film piezoelectric material subjected to the external vibrational source was $37 \mu\text{W}/\text{mm}^3$. For the electromagnetic effect, Saha et al. [39] showed that $4.375 \mu\text{W}/\text{mm}^3$ could be generated from the electromagnetic based generator subjected to the vibrating beam. Despesse et al. [40] built a system to convert the surrounding mechanical vibrations into electrical energy using the electrostatic transducer. The experimental results showed that, the maximum power density from the electrostatic material was about $0.584 \mu\text{W}/\text{mm}^3$ which is the least among the other two convertors. Therefore, it is clearly shown that the piezoelectric material has the highest power density.

Also, Gonzalez et al. [41] observed that, the piezoelectric transducer has a higher significant bandwidth than the electromagnetic transducer. These results were confirmed in studying the power density concerning voltage among different transducers, as shown in Figure 1. It can be noticed that, the piezoelectric material has

the widest power density versus the voltage compared to the electromagnetic transducer. Moreover, most of the energy harvesting mechanisms have a low voltage output that often-required multistage post-processing to produce a usable voltage. In contrast, piezoelectric energy harvesters produce enough amount of voltage that can be used directly.

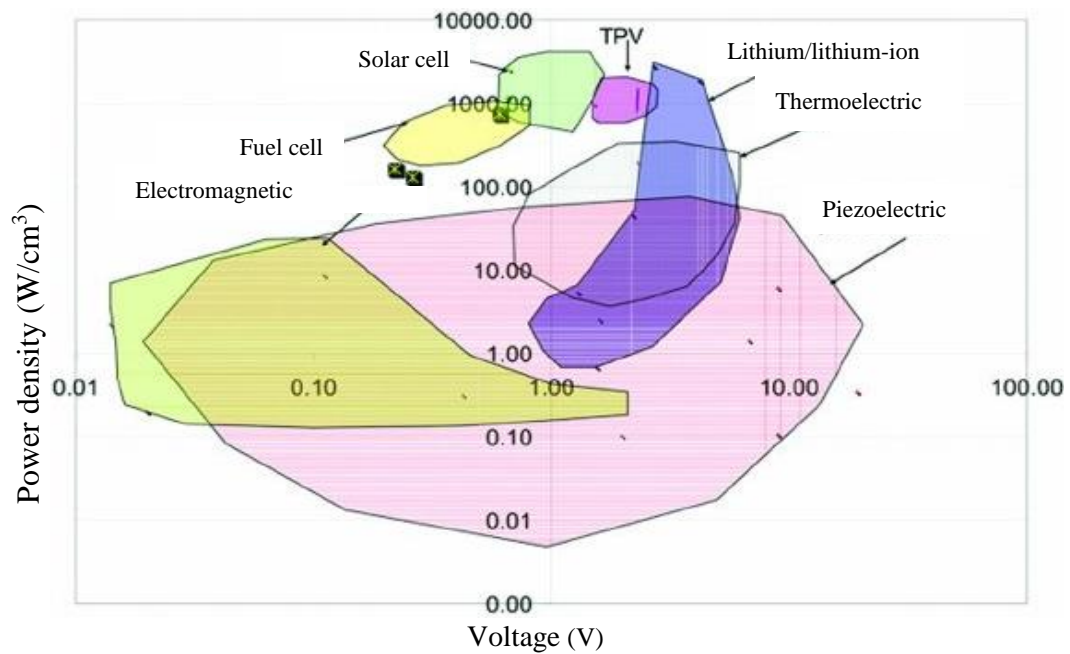


Figure 1: Power density vs. voltage of different energy harvesting mechanisms [41].

In addition, piezoelectric materials do not require any additional voltage input, unlike the electrostatic harvesters, which need an initial pre-charged of the variable capacitors by having an external polarization source for the initiation of the conversion process. Another important advantage of the piezoelectric materials is their compatibility with the macro and microstructures due to the thick and thin films fabrication techniques. However, the limitation of the electromagnetic harvesters to be fabricated in the micro-scale is due to the permanent magnets' poor characteristics and the limited number of the planar coil turns [42]. Table 2 summaries the advantages and

disadvantages of the three different transducers. Accordingly, the piezoelectric material is the best harvester method to be focused on in this article.

Table 2: Advantages and disadvantages of the conversion mechanisms [43].

Type	Advantages	Disadvantages
Electromagnetic	<ul style="list-style-type: none"> • No external voltage sources • No mechanical constraints needed • High output current 	<ul style="list-style-type: none"> • Difficult to integrate with MEMS fabrication process. • Poor performance in microscale • Low output voltage
Piezoelectric	<ul style="list-style-type: none"> • Simple structure • No external voltage sources • Compatible with MEMS • High output voltage • No mechanical constraints needed • Wide frequency range 	<ul style="list-style-type: none"> • Thin films have poor coupling • High output impedance • Charge leakage • Low output current
Electrostatic	<ul style="list-style-type: none"> • Easy to integrate with MEMS fabrication processes • High output voltage 	<ul style="list-style-type: none"> • Mechanical constraints needed • External voltage source or electrical recharged needed • High output impedance • Low output current

So, after harvesting the energy via piezoelectric material, the harvested energy can be used in powering various applications mainly in the wireless remote sensors. As reported by Tayahi et al. [44], the use of ten piezoelectric stacks were able to power a temperature sensor that operates in a current of less than 3 mA. The wireless sensors can be distributed and utilized in different applications such as industrial [45], [46], medical [47], [48], civil and military [49]–[51], agriculture and food industry [52]. For instance, in smart home and health applications, the monitoring sensors can be used in

home lighting or sleep and heart beating monitoring. Figure 2 describes the idea of energy scavenging from mechanical energy and its applications.

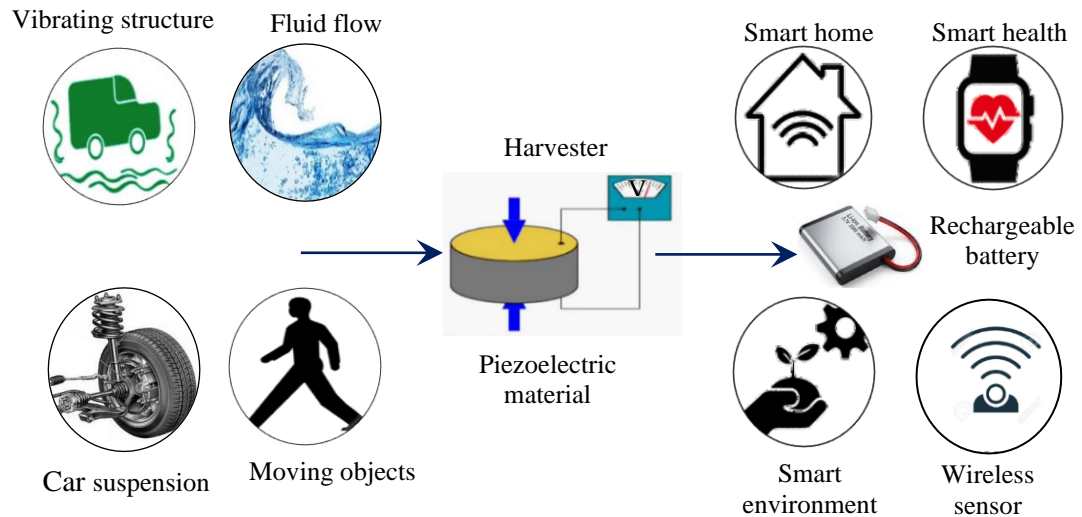


Figure 2: Energy harvesting from different mechanical systems and its applications.

2.2 Piezoelectric material

The piezoelectric material is being selected as a harvesting method since it is the best option among the other mechanisms. It can be implemented in a large variety of mechanical applications such as roads, cars, and human motions. Piezoelectric material has different types and configurations that will be discussed in the next sections.

2.2.1 Piezoelectric characteristics

The word piezoelectric came from the Greek word *piezo*, which means press or squeeze. It was first discovered in 1880 by French physicists Pierre and Jacques Curie [53]. The piezoelectric materials have a crystalline structure as they held together by an ionic bond. Another characteristic of the piezoelectric material is its anisotropic characteristic, which means that the material properties depend on the

force's direction and polarization electrodes orientation. The unique characteristic of the piezoelectric materials is the reversibility, exhibiting the direct piezoelectric effect (sensing) and reverse piezoelectric effect (actuation). When the material is unstressed, the piezoelectric crystal will be neutrally charged yielding dipole moments, which is a charge balance with positive and negative polarization. However, applying stress on the material will distort the dipoles or polarization, and creating an electrical charge. This process is labeled as the direct piezoelectric effect. Conversely, subjecting the piezoelectric material to an external electric field will create an unbalance in the neutral charge state that generates mechanical stress or strain, and it is called the reverse piezoelectric effect. The mechanical and electrical behavior of the piezoelectric materials can be defined using the following constitutive equations [54]:

$$D_i = d_{ij}\sigma_j + \varepsilon_{ij}^T e_i \quad (1)$$

$$\delta_j = s_{ij}^E \sigma_j + d_{ij} e_i \quad (2)$$

where D is the electric charge density (C/m^2), d is a piezoelectric charge constant (m/V or C/N), σ is the applied mechanical stress (N/m^2), ε is a permittivity of piezoelectric element (F/m), e is the electric field (N/C), δ is the mechanical strain, s is the elastic compliance coefficient of the piezoelectric element (m^2/N). The superscripts in the equation represent mechanical or electrical boundary conditions (constant stress or constant electric field), whereas the subscripts represent the direction of the mechanical and electrical parameters.

As mentioned earlier, piezoelectric materials are anisotropic materials, so their physical parameters (e.g., charge constant d_p , permittivity ε_{33} , and modulus of elasticity E_p) depend on the direction of the applied mechanical force and electric charge collected. Figure 3 illustrates the direction indexes of the constant parameters

in a rectangular crystallographic system with positive polarization along the z-axis. The first index represents the electric field direction and the second one represents the direction of the mechanical stress or strain. The notations 1, 2, and 3 identify the directions in the piezoelectric material along the three axes X, Y, and Z, whereas the shear constants are described using 4, 5, and 6 notations.

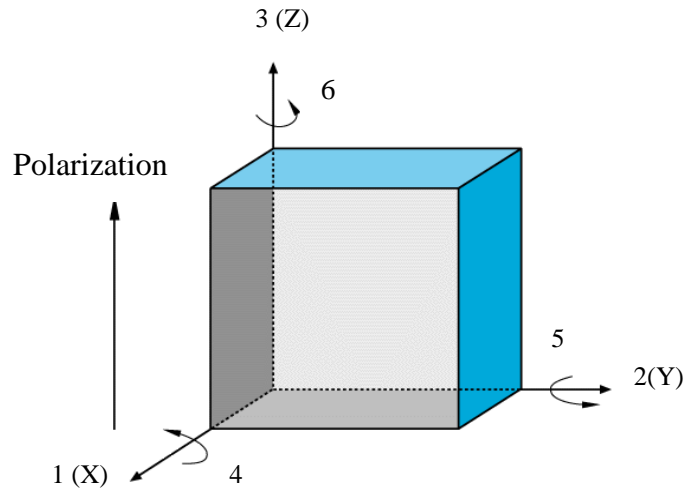


Figure 3: Direction of polarization for a piezoelectric material.

There are two commonly coupling modes of operation for piezoelectric materials. The transverse mode 31 which is depicted in Figure 4 (a) and the longitudinal mode 33 which is shown in Figure 4 (b). In mode 31, the mechanical lateral force is applied perpendicular to the polarization axis. However, in mode 33 the applied force is applied in the direction of the polarization axis as a compression force. Choosing the appropriate mode for maximizing the power output is dependent on the force applied to the piezoelectric material. Mode 31 is commonly used for energy harvester, especially for the piezoelectric cantilever beam structures where the lateral stress on the beam can be easily coupled to the piezoelectric material [55], [56]. On the other hand, Calì et al. [57] noted that mode 33 is suited for automotive and machinery for producing a higher output power. The most common piezoelectric

configurations applied in the energy harvesting are mode 31 (bimorph) and mode 33 (stack).

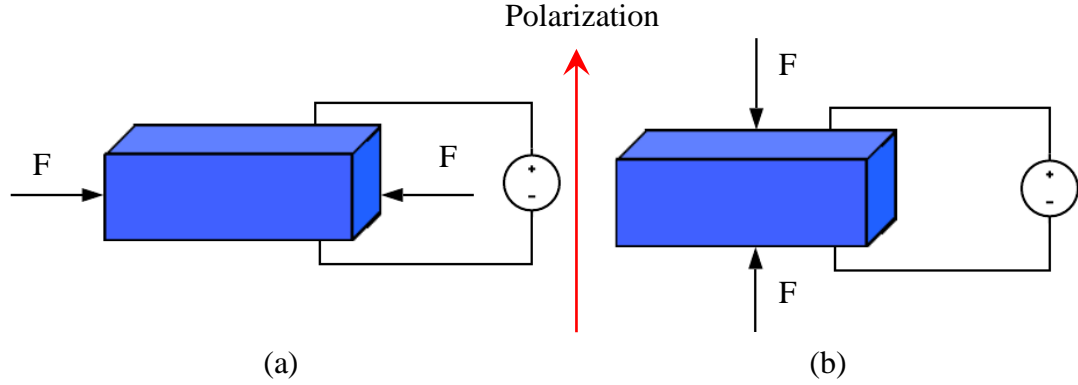


Figure 4: Modes of a piezoelectric material. (a) Mode 31. (b) Mode 33.

Piezoelectric materials are widely available in various forms as natural or human-made. The most common natural piezoelectric material is quartz, while the most active and used is ceramic, which is human-made material. Mainly, piezoelectric materials are categorized into four main groups depending on their structural characteristics, and those are ceramics, polymers, mono-crystals, and composites. Nevertheless, the two primary materials used in harvesting energy are piezo-ceramics like Lead Zirconate Titanate (PZT) or Barium Titanate (BaTiO_3), and piezo-polymers like Polyvinylidene Fluoride (PVDF) [58]. PZT is the most common type of ceramics, and when they deformed by 0.1% from the original dimensions, they will have the ability to generate enough piezoelectricity. Conversely, subjecting PZT material to an external electric charge will cause a change of 0.1% from the static material's dimension [59]. PZT material has higher power output per unit area under a high temperature compared to the PVDF. As reported by Makki and Iliev [60], PZT has harvested power output per unit area of $9.37 \times 10^{-3} \text{ mW/mm}^2$ while, PVDF has harvested a lower value of $5.31 \times 10^{-4} \text{ mW/mm}^2$. Moreover, the PZT films coefficients

are at least two times greater than PVDF and BaTiO₃ materials and therefore generating the higher power output [58].

2.2.2 Piezoelectric different configurations

2.2.2.1 Bimorph and unimorph cantilever

The piezoelectric design is being selected based on the direction of the applied force on the material as compression, bending, and shear mode. The most used design in the vibration energy harvesting is bending mode with cantilever structure. The cantilever beam is a simple structure and has two different configurations based on the location of the piezoelectric material. A piezoelectric layer can be on one or both sides of the elastic layer that is known as unimorph and bimorph configurations, respectively. The detailed comparison between these different types was illustrated by Ng and Liao [61].

In the case of bimorph configuration, two piezoelectric materials are bonded together with a metal layer in between, as shown in Figure 5. The bonded piezoelectric layers can be connected in series or parallel depending on the accumulated voltage and current respectively [57]. The most common bimorph operating mode is 31 bending mode so that the top and bottom layers undergo opposite direction: in compression and tension.

Another cantilever configuration is the unimorph design, where one piezoelectric material is attached to the metal layer. This design is mostly used for the microstructure applications, and it can be operated in both 31 and 33 modes [62]. As mentioned in the literature, the d_{33} piezoelectric coefficient is two times larger than the d_{31} , and consequently, the generated voltage will be higher assuming same structure

parameters [62]–[64]. The direct relationship between the piezoelectric coefficient and the output open circuit voltage is illustrated by the following equation (3)

$$V_{oc} = \frac{d_{ij}}{\epsilon_r \epsilon_0} \sigma_{ij} g_e \quad (3)$$

where the open circuit voltage V_{oc} is proportional to the piezoelectric coefficient d_{ij} , applied stress σ_{ij} and the gap distance between the electrodes g_e . ϵ_r , and ϵ_0 are the relative dielectric constant and vacuum permittivity. Another factor affecting the output voltage is the gap distance between the electrodes. The piezoelectric layer in mode 31 is between top and bottom electrodes, whereas in mode 33, the electrode is on the top of the piezoelectric layer [65]. As the thickness of the piezoelectric layer in unimorph design is very thin, the electrode distance in mode 31 is shorter than the electrode distance in mode 33. The experimental results of Kim et al. [66] showed that, a dielectric constant of d_{33} mode was two times higher than the d_{31} mode which consequently resulting in higher output voltage. Moreover, they concluded that with the smaller area of mode 33 compared to mode 31, the mode 33 can generate higher output power of $\approx 2.23 \mu\text{W}$ by enhancing an interdigitate electrode IDE configuration through reducing the finger width to $2 \mu\text{m}$. Table 3 shows the complete comparison between 31 and 33 modes as discussed by Kim et al. [66].

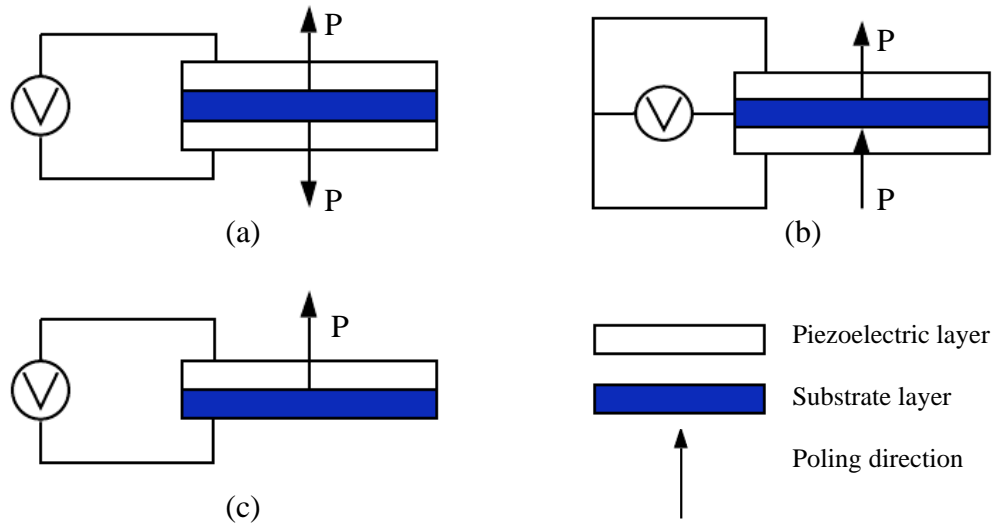


Figure 5: Different configuration of bimorph and unimorph. (a) Bimorph configuration in series connection. (b) Bimorph configuration in parallel connection. (c) Unimorph configuration.

Table 3: Comparison of 31 and 33 modes [66].

Parameter	31 mode	33 mode
Electrode area (mm^2)	2.88	0.154
Electrode gap (μm)	1	12
Volume of piezoelectric layer (mm^3)	0.00288	0.00205
Output power (μW)	2.15	2.23
Power density ($\mu\text{W}/\text{mm}^3$)	8.09	8.39

2.2.2.2 Piezoelectric stack

A piezoelectric stack is a multilayer piezoelectric sheet stacked on the top of each other. These layers (represented by N) are connected mechanically in series and electrically in parallel. The piezoelectric stack is operated in mode 33 where the mechanical force is applied along the polarization axis while the electric charge is collected on the surface perpendicular to the polarization axis, as shown in Figure 4 (b). Stacks are more preferable to be utilized in low-frequency ranges and high force

excitation [67]. The stack geometry helps in amplifying the charge production compared to the single layer. Equation (4) shows the relationship between the number of piezoelectric layers N , force F and voltage V with the stack output current Q [68],

$$Q_{stack} = Nd_{33}F + C_pV \quad (4)$$

Piezoelectric stacks can withstand large mechanical forces that enable them to achieve higher output power than piezoelectric cantilever [69]. Liu et al. [62] also stated that the output power from the piezoelectric stack is higher than the cantilever design. Though, it needs large applied force because of the high stiffness coefficient K_p that depends on the modulus of elasticity E_p , surface area A_p , and thickness h_p of the piezoelectric stack.

2.3 Energy harvesting from different vibrations

By utilizing the property of piezoelectric materials of generating electricity, several scientific researchers have been investigated the piezoelectric energy harvester types in a wide variety of applications. In general, harvesting energy from mechanical sources providing an output power of 4 W to 800 W [28]. The vibrations could be observed from human activities such as walking [70]–[73], heart beating [74], and breathing, where the energy will be detected from the expansion of the chest [75]. Different ways are available to bond the piezoelectric material. For instance, piezoelectric material could be bond with the shoe to harvest the dissipated energy from the ball foot using PVDF material under the shoe or foot strike using PZT flatten layer under the heel. These two approaches were discussed by Shenck and Paradiso [70] and are shown in Figure 6. Choi et al. [71], summarized the possibilities of locating piezoelectric material in different human joints in order to harvest the

dissipated energy from human motions. Table 4 shows the harvested power from each joint location considering human walks at a speed of 1.3 - 7.8 km/h.

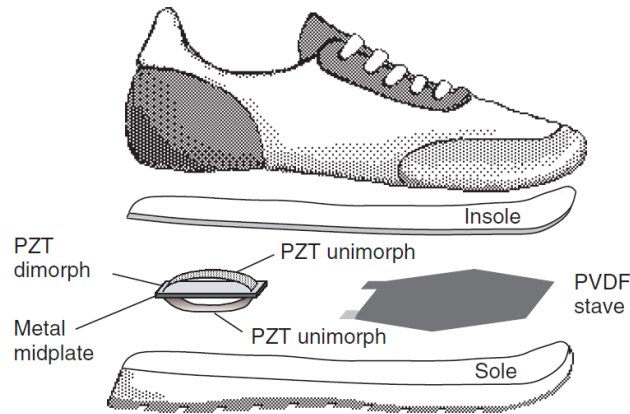


Figure 6: Two methods of harvesting energy from the shoe PVDF under the ball foot and PZT materials under the heel [70].

Table 4: Harvested power from human motion [71].

Joint/Motion	Power (W)	Work (J/step)
Foot strike	2-20	1-5
Ankle	66.8	33.4
Knee	36.4	18.2
Hip	38	8.96
Elbow	2.1	1.07

Mitcheson et al. [76] also reported that the power harvested by human breathing was around 78 mW. Another way for harvesting energy is by installing the piezoelectric material underneath the floor material so it will capture the vibrations resulted from the passenger's movement. East Japan Railway Company applied this mechanism by conducting a real experiment in Tokyo station from the period of January 19 to March 7, 2008. The piezoelectric material was installed in the ticket gate area as shown in Figure 7, where considered as a very high traffic. The daily harvested

power was about 10 kW, which is sufficient to run the automatic ticket gates and electronic displays [77]. However, after a period of three weeks of passing more than 800,000 people, the total output power decreased due to degradation in the piezoelectric material durability.



Figure 7: Power-generating floor at Tokyo Station's Marunouchi North Exit [77].

Another application of harnessing energy is from the footsteps is the dance clubs. In 2008, the first sustainable dance club in the world was opened in Rotterdam and named Club Watt [78]. The dance floor was embedded by the piezoelectric materials to absorb the vibrations from the dancer's steps and generating energy. Also, London established an eco-nightclub at Bar Surya, where the dancing floor was made of a series of springs and piezoelectric blocks [79]. As the dancers moved up and down on the bouncing dance floor, the piezoelectric blocks squeezed and generated current to power some parts at the club.

Besides, vibrations absorbed from buildings are another type of ambient energy source. Aminzahed and Jabbari [80] designed a piezoelectric energy harvester placed on the ceiling of each top floor of a five-story wooden building. The outcomes from their model showed that increasing the input frequency on the first floor from 15 - 40

Hz led to increasing the harvested power from 0.25 - 0.7 mW in the building floors. These results were also confirmed by Kan et al. [81] by developing a piezoelectric energy harvesting system to harvest energy from a wood floor vibration induced by human activities. The piezoelectric harvester should be placed in a proper way to maximize the harvested power. This was addressed by Elhalwagy et al. [82] by studying how to get the maximum benefits from the harvested energy in buildings' interior spaces. The study was according to the different types of applications, and other different factors such as the needed power, number of steps, and the cost of electricity kilowatt. Piezoelectric sensors were connected in series and parallel and placed in the tile where the pressure is applied in the floors of the building. The high generated power tiles could power an LED lighting system, and the low generated power tiles could help in controlling the self-powered sensors. The power could also be harvested from the building's ducting system, as mentioned by Yatim et al. [83]. Their piezoelectric model converter was able to harvest the power of approximately 2 W, which could be adequate for mini home devices.

Moreover, the energy could be harvested from road traffic as well. Jiang et al. [84] conducted a theoretical and experimental investigation of energy harvesting from the roadway. In each harvesting unit, three piezoelectric multilayer stacks shown in Figure 8 (a) were insulated in-between the road pavement, and they deformed once the car tires pass through it. The experimental results verified the theoretical analysis, and they indicated that each single harvesting unit could generate a power up to 1 W with a car's speed of 100 km/h. This power output can power a wireless sensor system.

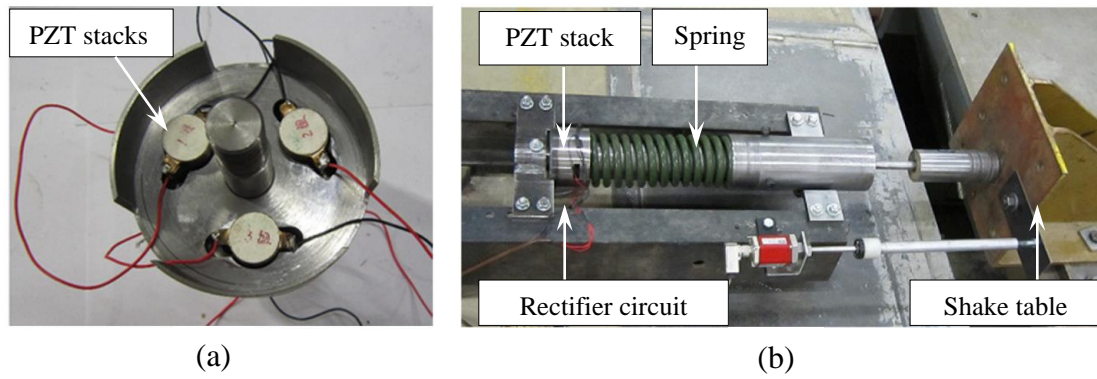


Figure 8: Energy harvester from road traffic. (a) Piezoelectric stack. (b) Experimental setup [84].

Li et al. [85] introduced a single piezoelectric vibrator mounted between the upper and middle layers of the asphalt roadbed structure. According to their theoretical results, each piezoelectric energy harvester was able to generate a power of 0.67 mW. Abramovich et al. [86] invented a device that was made of a piezoelectric generator for harvesting energy from roads, highways, and airport runways. The deformation of the piezoelectric material was due to the weight of passing cars. This product was produced in an energy harvesting company called Innowattech [87]. In 2009, the company applied a test by embedding the piezoelectric harvester device 5 cm below the road surface. The results claimed that, energy production was around 200 kWh in 1 km per lane of the road. Environmental Transport Association ETA has published that, if an appropriate harvester is installed in a every stretch of British motorway, the generated energy will be able to run about 34,500 small cars [88]. Among these different applications, the focus in this work is harvesting energy from the CSS as there is an enormous amount of power dissipated from its dampers. This issue will be discussed in detail in section 2.4.

2.4 Car suspension system

The most mechanical vibrations that have been extensively explored are the car suspension system (CSS). It can suppress uncomfortable situations from different road profiles to provide good road handling, stability and comfortability to the passengers. Modeling CSS theoretically and experimentally will be presented in the following sections.

2.4.1 Mathematical car models

Several mathematical models have been utilized for analyzing car dynamics. These models can also be called lumped parameter models, and they can study the behavior and the performance of the CSS. A mathematical car model is derived from the fundamental law of physics, such as Newton's Laws or conservation principle. The CSS can be modeled as a quarter car model (QCM), half car model (HCM), and full car model (FCM).

The QCM (shown in Figure 9) is frequently used in the car suspension analysis due to its simplicity and can provide the main essential characteristics of the full model. Thus, many researchers were focused on the analysis of the QCM. Vaishnav et al. [89] derived a mathematical model of the QCM by using transfer function and Cramer's rule. Sharma et al. [90] designed two DOF of a QCM with state-space representation by using MATLAB. The car was excited with step input of 0.1 m that resulted in a high overshoot of the sprung mass (80%) and unsprung mass (30%). These values were not satisfied with the ride comfort and quality. To overcome this problem, the authors proposed using a controller to keep the car move within the ride comfort ranges. Moreover, Jamali et al. [91] developed a QCM for an electric car in order to

evaluate the car's isolations to road disturbance. The study was focused on comparing the displacement and acceleration amplitudes of the sprung and unsprung masses with the road amplitude at different damping coefficients. Throughout the Simulink MATLAB program, the minimum frequency response occurred when the damping constant equal to the optimal damping constant b_{opt} that can be calculated by the following equation:

$$b_{opt} = \sqrt{\frac{K_s M_s}{2}} \sqrt{\frac{K_{us} + 2K_s}{K_{us}}} \quad (5)$$

where M_s is the sprung mass, K_s and K_{us} are the stiffness coefficient for sprung and unsprung masses, respectively.

Florin et al. [92] simulated a QCM by MATLAB Simulink and compare it to the state space model and transfer function. The results obtained from the three different methods were identical with the same values of suspension parameters. Hassaan [93] examined a QCM passing a circular hump with sustaining a comfortable ride. The mathematical model was derived by using a state model and analyzed by MATLAB Software. In order to achieve a comfortable ride, the study showed that, the car speed should not exceed 7 km/h when passing a circular hump. Prabhakar and Arunachalam [94] have conducted a comparison between the conventional passive suspension and passive suspension with different parameters of damping and stiffness coefficients of a QCM. For providing the best ride comfort as well as the car handling, an optimum value for the sprung damping and stiffness coefficients were found to be 1500 N.s/m and 13 kN/m respectively. Gao et al. [95] investigated the effect of the randomness of a QCM parameters on the dynamic analysis. The results from the study illustrated that, the randomness of the mode shapes is highly independent of tire

stiffness, while it is dependent on the sprung and unsprung masses. Moreover, the first natural frequency is influenced by the uncertainty sprung mass, and the second natural frequency is affected by the uncertainty unsprung mass system.

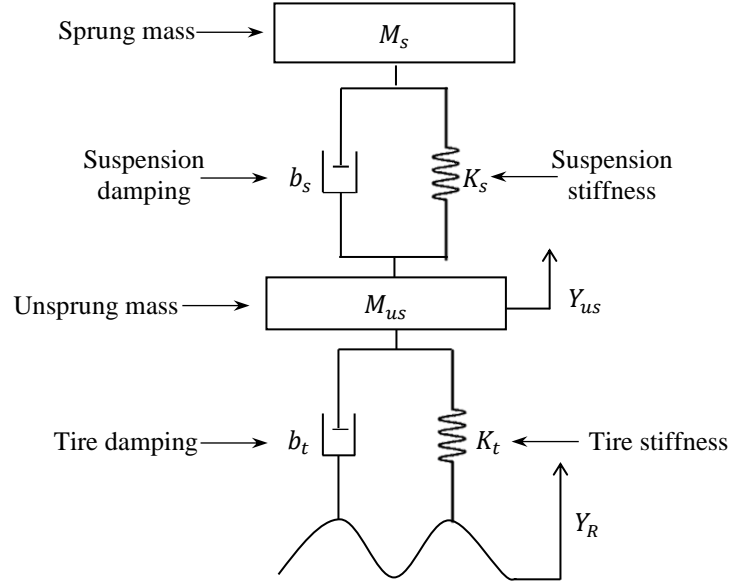


Figure 9: Two DOF model.

QCM can be easily modeled for the experimental work. The most common model has two moving plates which representing the sprung and unsprung masses connected to the springs and dampers. The differences among the models are occurred in modeling the unsprung mass as a real car tire or plate and the excitation input force. For the models with one real tire, Salah [96] modeled the QCM as a real tire connected to the moving plate, and shock absorber in between (See Figure 10 (a)). The moving plate represented the quarter of the sprung mass and the shock absorber was made of the spring and damper. The model also included four stainless steel rods to guide the movement of the plates as vertical with no torsion. Having a real car tire gave a realistic data analysis, and the model could handle a maximum weight of 300 kg and run up to 162 km/h. Figure 10 (b) shows Mitra et al. [97] model which consists of a real tire that connected to the spring and damper with the sprung plate. The cam mechanism

was utilized to convert the motor rotary motion into translation motion. Shing et al. [98] designed and modeled a QCM with real tire that was connected to the four springs and two shock absorbers. This model is presented in Figure 10 (c). The weight of 3 kg was placed at the top of the sprung plate to represent the mass of the quarter sprung mass.

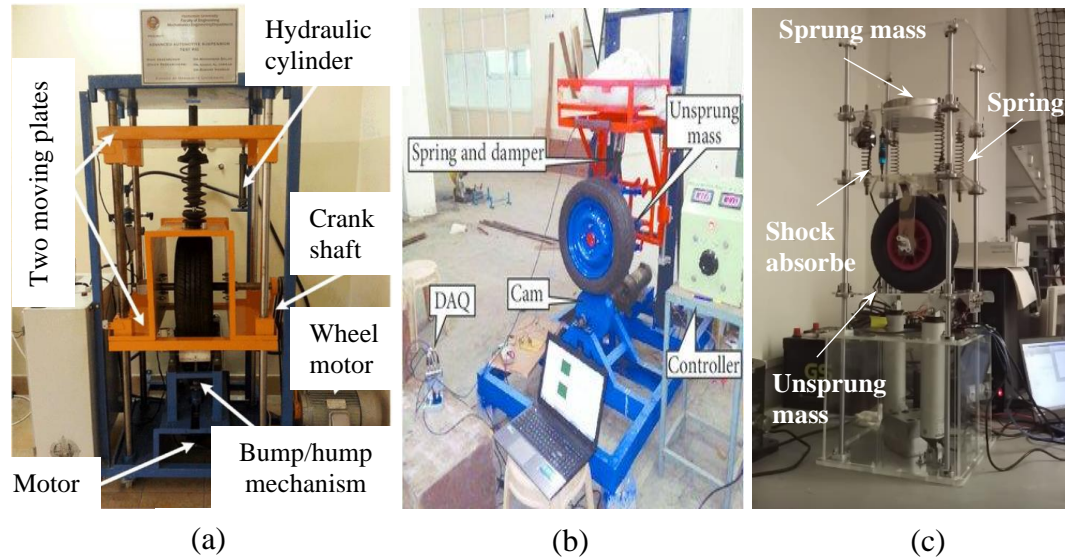


Figure 10: Different experimental setups of QCM as real tires. (a) Mohammad Salah model [96]. (b) Mitra et al. model [97]. (c) Shing et al. model [98].

On the other hand, most of the researchers modeled the unsprung mass as a moving plate. According to work done by Jugulkar et al. [99], they modeled two moving plates with four springs and adjustable damper. As shown in Figure 11 (a), the springs were connected in parallel, and each has a stiffness coefficient of 3.33 N/mm. One more spring of stiffness 32.77 N/mm was connected to the damper in series at the center of the plate. The system was guided by a central bar with roller bearings to minimize the friction. The excitation input was modeled as an electric motor with a Scotch Yoke mechanism to convert the motor rotational motion into linear motion of the system. Likewise, Patil and Joshi [100] modeled two moving plates with a suspension shock absorber and tire spring, as illustrated in Figure 11 (b). The

corresponding values of the suspension stiffness, tire stiffness, and viscous damping were 13.9 kN/m, 85 kN/m, and 518 N.s/m, respectively. The system was excited by DC motor with cam and follower mechanism to attain harmonic excitation at specific frequency and amplitude. Additionally, Quanser [101] built three moving plates as; sprung mass, unsprung mass, and the road, as shown in Figure 11 (c). Two adjustable springs of 900 N/m and dampers 7.5 N.s/m were connected between the sprung and unsprung plates. Another two springs of 2.5 kN/m and dampers of 5 N.s/m were connected between the unsprung and road plates. The system was driven by the DC motor with lead screw and cable transmission to provide the vertical motion.

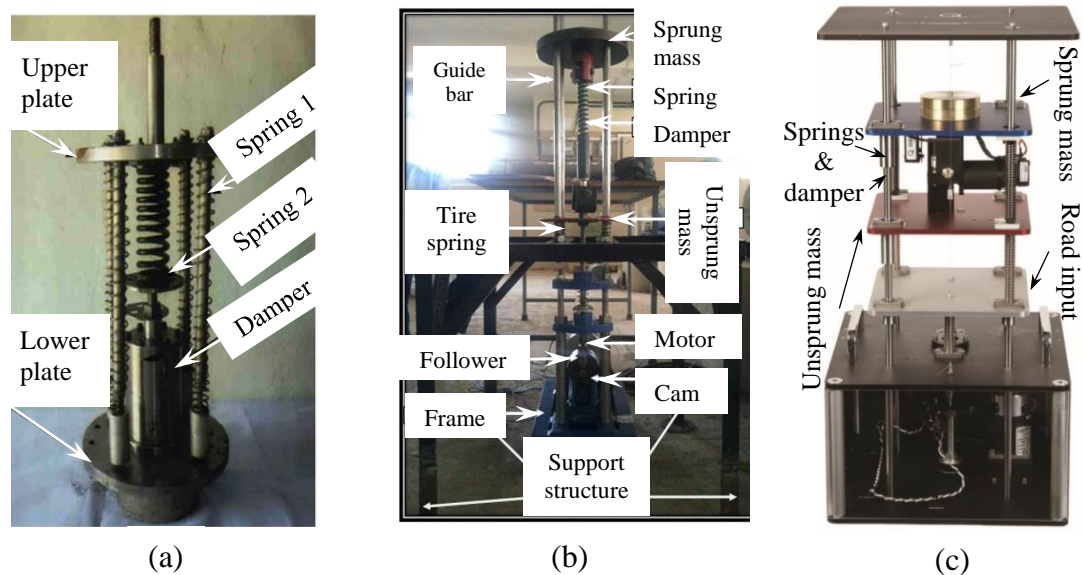


Figure 11: Different experimental setups of QCM as moving plates. (a) Jugulkar et al. model [99]. (b) Patil and Joshi model [100]. (c) Quanser model [101].

Unlike the QCM which consists of one tire, the HCM is four DOF that is made of two tires: one for the front and one for the rear axles. HCM, as presented in Figure 12 assumes the symmetry of the car about the longitudinal axis. The different characteristics of springs and dampers at the front and rear tires take into consideration which exists in the actual cars as well. Moreover, the effect of the center of gravity and

body motions was simulated using HCM. Gao et al. [102] investigated the effect of the uncertainty of random parameters of a HCM. The car suspension was subjected to a random input excitation, which is modeled employing power spectral density (PSD). It was concluded that, the uncertainty of the natural frequency of the cars is dependent on the uncertainty of the car parameters. The distance of the front and rear suspensions has a significant influence on the first two cars' frequencies. Whereas, the third and fourth cars' frequencies are affected by the front and rear tires' mass. Patel et al. [103] studied a HCM for measuring the road profile at different speeds by developing a unique algorithm using MATLAB Simulink Software. The HCM was excited by the input road profile and being compared with the measured road profile at various speeds. The simulation of the HCM showed a good agreement between the input and measured road profile in time, distance, and frequency domain.

Some researchers have been analyzed and compared both quarter and HCM in their research. Mehmood et al. [104] conducted a full dynamic analysis for a quarter and HCM using Laplace transformation and state space representation in the MATLAB program. Their analysis was focused on finding the optimum values for the damping coefficient to achieve the optimum driving comfort level. For 2 DOF, the appropriate damping range was found to be between 3000 and 4000 N.s/m. However, a range of 1500 N.s/m to 2000 N.s/m was found to be the optimum for the 4 DOF. Additionally, Faheem et al. [105] analyzed both a quarter and HCMs in displacement and frequency responses for finding the suitable damping coefficient values. The results of the two models showed that, the damping coefficient should not exceed a value of 3000 N.s/m for providing the desired performance.

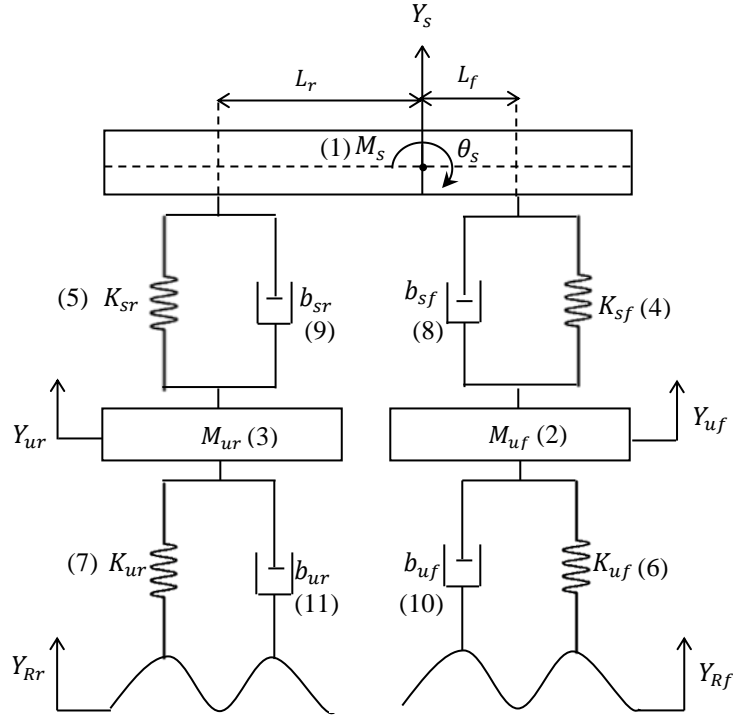


Figure 12: Four DOF model. (1) Sprung mass. (2) Front unsprung mass. (3) Rear unsprung mass. (4) Front suspension stiffness. (5) Rear suspension stiffness. (6) Front tire stiffness. (7) Rear tire stiffness. (8) Front suspension damping. (9) Rear suspension damping. (10) Front tire damping. (11) Rear tire damping.

A few investigations are available in the literature on modeling the HCM experimentally. Sapiński and Martynowicz [106] modeled a HCM as two identical suspension sets made of spring and magnetorheological shock absorbers (MRA) as shown in Figure 13 (a). The two suspensions were connected by a steel frame with a weight that representing the half-sprung mass. One of the suspension sets was excited by the shaker of type electro-hydraulic cylinder, while the other suspension was excited by the motor connected to a cam crank mechanism. An additional central roller was placed for guiding and stabilizing the system. The experimental work was focused on studying the vibration control with considering the bounce and pitch motions. Using an appropriate magnetorheological shock absorber (MRA) was able to minimize the vibrations by reducing the displacement and acceleration amplitudes. Likewise,

Chavan and Sawant [107] built two suspension systems that were connected by the beam as presented in Figure 13 (b). Each suspension was made of spring and shock absorber and excited by the eccentric cam. For different excitation frequencies, the experimental results matched the simulation results with considering the non-linearity of the suspension system.

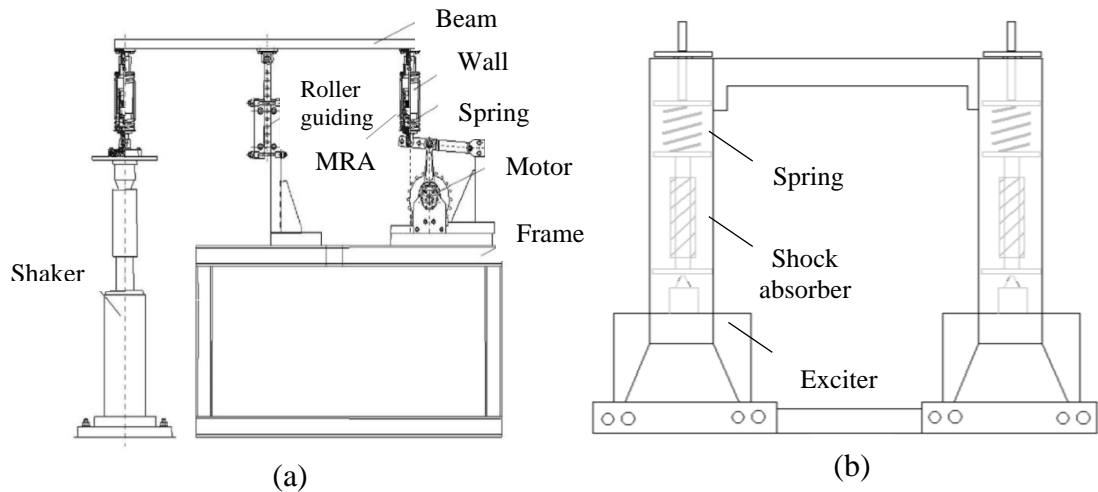


Figure 13: Different experimental setups of HCM. (a) Sapiński and Martynowicz model [106]. (b) Chavan and Sawant model [107].

The rolling motion is considered in a full car model (FCM) which will increase the number of degrees of freedom to seven. FCM shown in Figure 14 is made of the four identical QCMs that are coupled by rods. 7 DOF consisting of the bounce, pitch, and roll motions of the car body, and the other four vertical motions for each of the unsprung masses.

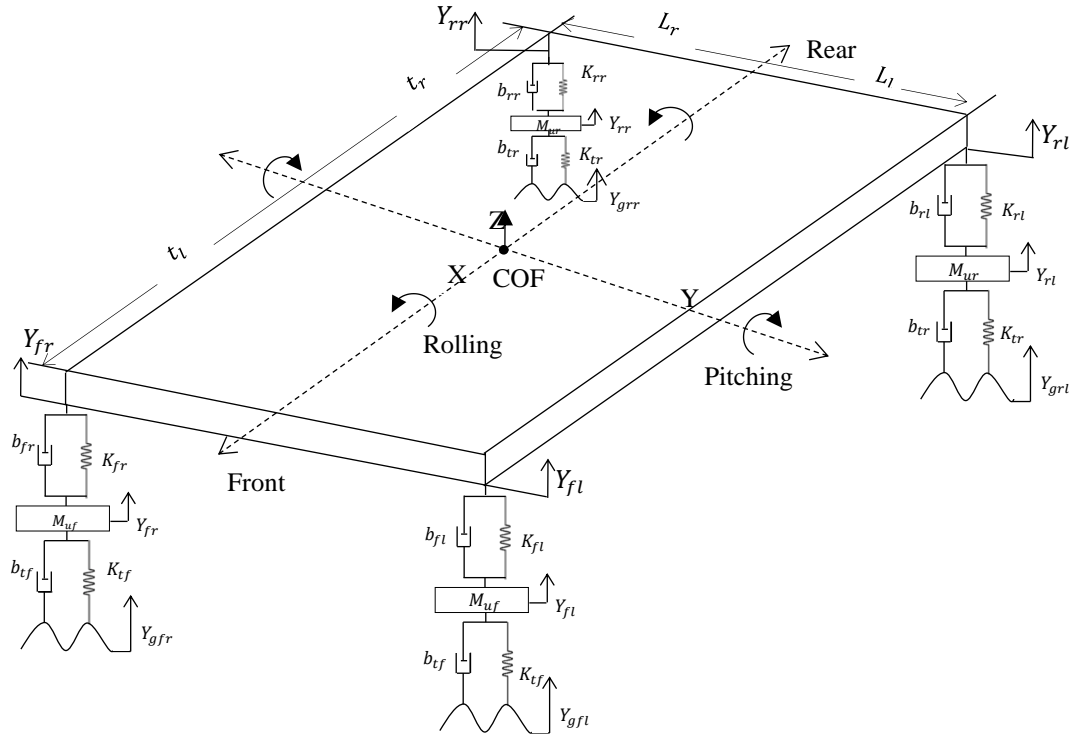


Figure 14: Four DOF model.

FCM can ultimately be used to study and analyze car performance and ride comfort. Several parameters must be taken into consideration when studying the passenger ride comfort such as RMS vertical acceleration, speed over a bump, suspension travel distance, and road handling. For the weighted RMS vertical acceleration, British standard institute listed different levels of acceptability of ride quality as presented in Table 5 [108].

Table 5: Levels of acceptability of ride quality [108].

Weighted RMS of vertical acceleration (m/s^2)	Acceptability
<0.315	Not uncomfortable
0.315-0.63	A little uncomfortable
0.5-1	Fairly uncomfortable
0.8-1.6	Uncomfortable
1.25-2.5	Very uncomfortable
>2	Extremely uncomfortable

Besides, Mitra et al [109] reported some values of different characteristics for achieving a ride comfort. The car speed must be less than 10 km/h when passing over the bump, minimum of 0.127 m of the suspension travel distance, and road handling of the relative distance between the road and the tires must be in the range of 0.0508 m. Their results of studying the FCM satisfied the ride quality characteristics. Raju and Venkatachalam [110] derived the equations of motion of the FCM and studied the suspension system when subjected to different disturbances. Pulse and impulse disturbances were given to the right front wheel. For the case of the pulse input, the maximum oscillations affected the front axle with little effect of the rear axle. However, for the impulse disturbance, the maximum oscillations undergoing the front axle were much higher than the pulse disturbance. Rajale et al. [111] evaluated the car comfort characteristics of the FCM with eight degrees of freedom, including a suspension system and car seat. Different signal inputs were studied in the displacement of the four main full car parameters, heave, pitch, roll, and seat. For step input, the displacements of the four parameters increased at the beginning and then decreased with time. For triangular signal, it was affected only the heave and pitch displacements. However, the sinusoidal input affected the whole displacements except the seat displacement at certain car speed. Iyer et al. [112] studied the FCM with independent suspension of the front tires and conventional suspension for the rear tires. The optimum values for the spring and damper of the suspension system were discussed in order to provide the maximum comfortability to the riders. The values of the stiffness and damping coefficient were found to be 8300 N/m and 700 N.s/m, respectively. Mahala et al. [113] evaluated the car responses of the quarter, half, and full car models. The study concluded that increasing the number of degrees of freedom will raise the accuracy of the analysis while it will increase the simulation time. There

is no experimental investigation of modeling and studying the FCM in the laboratories. Therefore, the work on HCM and FCM are minimal, and few studies are examined to be compared with a QCM, especially in the field of energy harvesting from a suspension system.

2.4.2 Energy harvesting from car suspension system

The dissipated energy from the suspension system can be converted to another useful form using different types of harvesters. In their work, Zuo and Zhang [114] reported that, the potential of harvestable power was in the range from 46 to 7500 W. Though, the work on implementing the piezoelectric harvester in the CSS is limited. The piezoelectric material can be added as an additional energy harvesting element to the various locations in the CSS such as springs, tires, and dampers.

Moreover, Xiao et al. [115] studied the harvested energy from the piezoelectric material theoretically and experimentally. The proposed system in Figure 15 showed a QCM (2 DOF) with piezoelectric harvester placed in parallel with the suspension springs. For the theoretical study, the QCM was excited by sinusoidal input with 1 g (9.8 m/s^2) amplitude. The peak output voltage and power from the piezoelectric element were recorded as 274.62 V and 2.84 W, respectively. The harvested voltage and power were affected by the suspension parameters like tire stiffness, suspension stiffness, and damping coefficients. The proposed theoretical analysis was validated experimentally by modeling the sprung and unsprung masses as aluminum blocks with four springs and one piezoelectric element in between. The setup was subjected to a sine wave with an amplitude of 1.5 m/s^2 . The maximum output voltage was 0.33 V at a frequency of 38.58 Hz. However, the experimental harvested power was not mentioned in the paper. Also, the characteristics of the piezoelectric material such as

its type (cantilever or stack), dimensions (area A_p and thickness h_p), piezoelectric stiffness coefficient K_p , charge constant d_{33} , dielectric permittivity ϵ_{33} , and the modulus of elasticity E_p were not clearly mentioned.

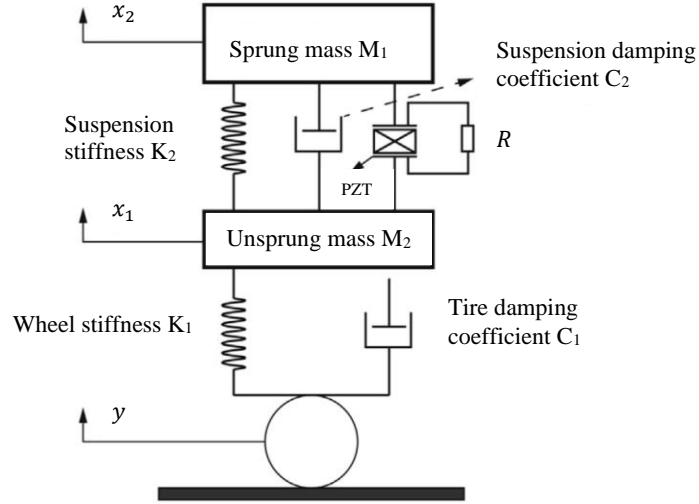


Figure 15: QCM with built in piezoelectric material in parallel connection [115].

On the other hand, Al-Yafeai et al. [116] coupled piezoelectric materials with the front and rear suspension system of the HCM shown in Figure 16. The results from the MATLAB/Simulink of the proposed model were compared with the Xiao et al. [115] model. The results illustrated that, the harvested voltage and power from the HCM were higher than that of the QCM by 77% and 57%, respectively. From both systems, the calculated voltage and power from the piezoelectric material were done without considering the stiffness of the piezoelectric material K_p .

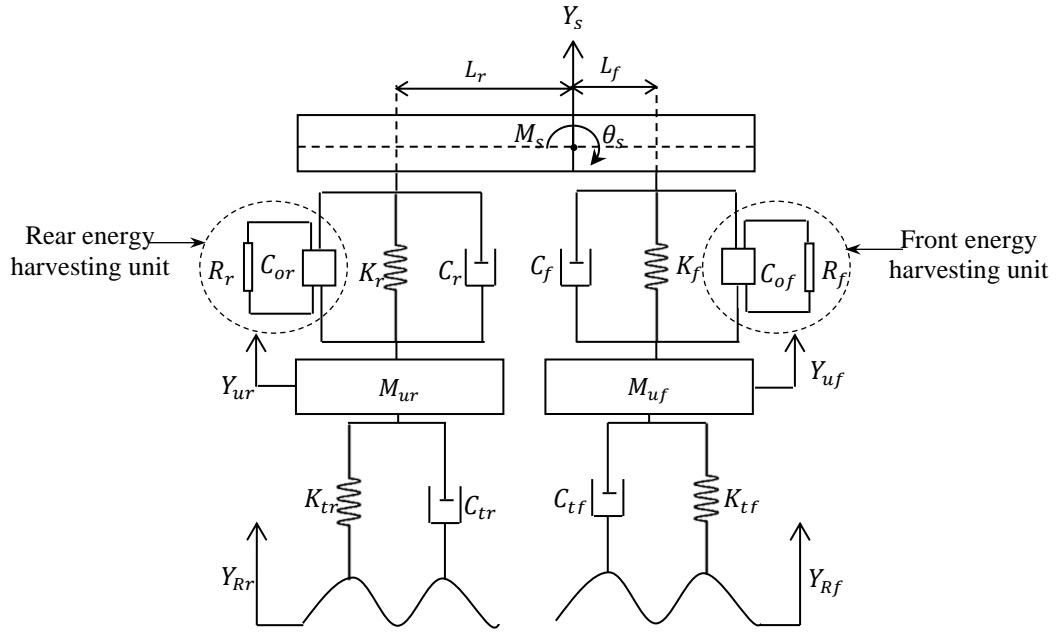


Figure 16: HCM with built in piezoelectric material in parallel connection [116].

Taking into account the piezoelectric stiffness will dramatically affect the harvested voltage and power. To validate this, a value of 6250 kN/m as an equivalent stiffness coefficient was considered when attaching the piezoelectric material in parallel with the suspension springs (as shows previously in Figure 15 and Figure 16). For the QCM, the overall stiffness coefficient of the system was calculated from the following relation

$$K_{eq} = K_s + K_p \quad (6)$$

where K_{eq} , K_s , and K_{piezo} are the stiffness coefficients of the equivalent connection, suspension, and the piezoelectric material, respectively. The relation shows that the overall stiffness coefficient increases when considering the piezoelectric material stiffness. The high value of the stiffness coefficient resulting in a huge reduction in the harvested voltage and power to be 9 V and 2.9 mW, respectively. The reason is that, the higher the system stiffness the lower its deformation and consequently the lower

its harvested voltage and power. While in a series connection (Figure 17) the harvested voltage and power remain the same as without considering the stiffness coefficient of the piezoelectric material. This is because the overall stiffness coefficient of the system is almost equal to the suspension spring coefficient as can be illustrated by the following relation:

$$K_{eq} = \frac{K_s \times K_{piezo}}{K_s + K_{piezo}} \approx K_s \quad (7)$$

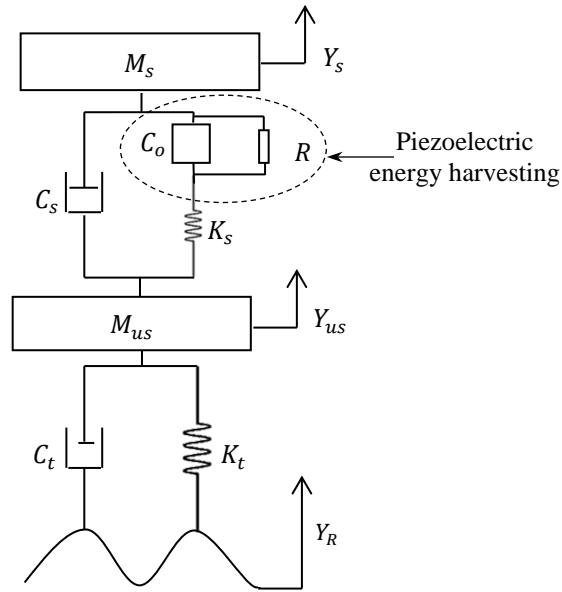


Figure 17: QCM with built in piezoelectric material in series connection.

Some studies were focused on harvesting energy from the deformation of the automobile's tires. As the tire flattened against the road surface, the piezoelectric material will be stretched and consequently generates electricity. Xie and Wang [37] proposed a dual-mass piezoelectric harvester that is connected to the QCM and presented in Figure 18. PZT4 harvester bar with dimensions of 10 cm height and 1.5 cm width was mounted on the suspension wheel. The mathematical model was subjected to the random rough road excitation with different road profiles B, C, and D. According to ISO/TC108/SC2N67; the road roughness was classified starting from

very smooth road to the very rough road. The calculations through the iteration method showed that the power of 738 W could be harvested from the road profile of type D by implementing more than four piezoelectric bars in the system. Each bar has height and width of 10 cm and 1.5 cm, respectively, with a car speed of 35 m/s. This harvested power was also affected by the suspension and piezoelectric harvester parameters. For instance, increasing the car speed and decreasing the width bar will significantly increase the electric power generated from the cars. Likewise, Zhao et al. [117] designed a piezoelectric harvester attached to the suspension system that subjected to random and pulse road excitations. From random excitation, the system was able to harvest a power of 18.83 W, while for the pulse excitation, a power of 102.24 W was harvested at car speed of 30 km/h. Their findings were also similar to the one mentioned by Xie and Wang [37] in which they stated that the harvested power is affected by different parameters like vehicle speed and the piezoelectric material cross-sectional area.

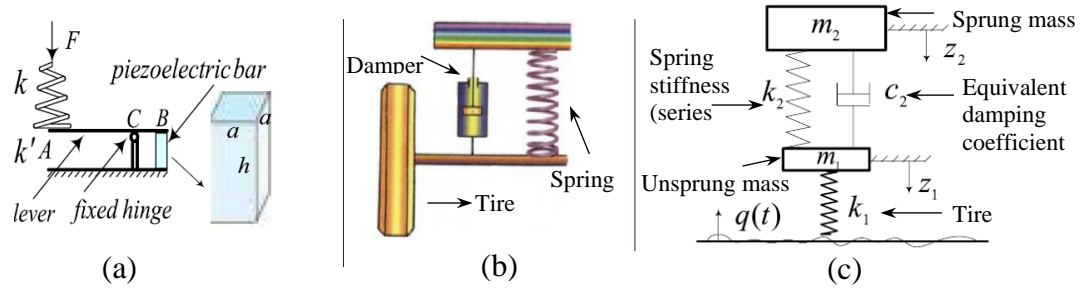


Figure 18: Dual mass piezoelectric bar harvester of QCM. (a) Piezoelectric bar harvester. (b) QCM. (c) Dual mass piezoelectric energy [37].

Likewise, Lafarge et al. [118] embedded a piezoelectric cantilever beam of type PZT 27 to the suspension wheels, as shown in Figure 19. The QCM was operated at the cantilever first natural frequency with different load resistances by the Bond Graph language. The power from two different resistors 22 k Ω and 222 k Ω was

recorded as 1 mW and 1.4 mW, respectively, where it could be powering several sensors for monitoring applications. The system was also investigated in the real case by installing the piezoelectric beam into the unsprung mass. The harvested power at a speed car of 10 km/h was varied between 0.001 mW and 0.021 mW. However, the harvested power of the range of 0.01 mW and 0.07 mW was occurred at 30 km/h. Furthermore, Behera [119] also connected three PZT5A piezoelectric materials in series along the inner tires' circumference. The three series of piezoelectric elements in the tire is illustrated in Figure 20. From his rough calculations, the model at a speed of 40 km/h was able to harvest power of approximately 14 mW.

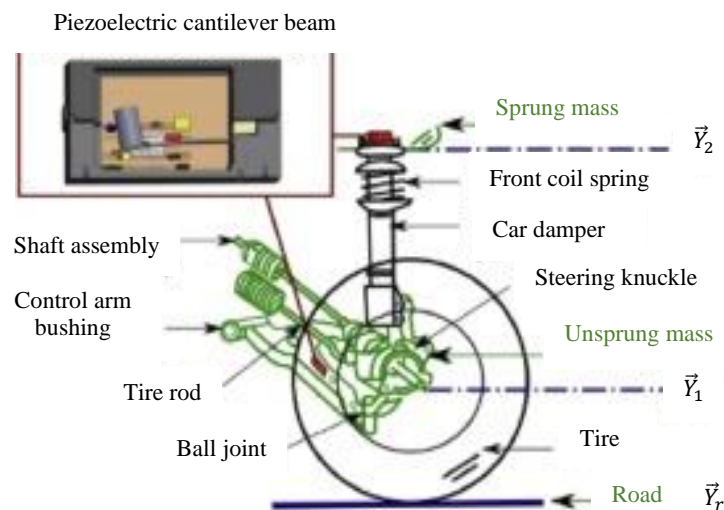


Figure 19: Car suspension with piezoelectric cantilever beam [118].

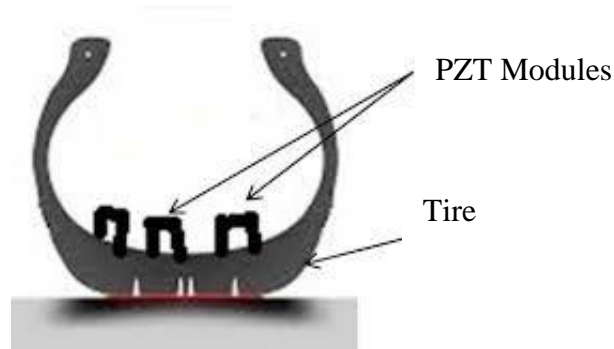


Figure 20: Three piezoelectric materials located on the tire [119].

Another utilization of the piezoelectric harvesters is to be located at the center of the tires. This provides a rotational motion of the harvester as the tires rotate. Matching the natural frequency of the piezoelectric harvester with the rotating frequency of the tires will help in maximizing the output harvested power. As stated by Gu and Livermore [120], the impact frequency of the harvester is twice the rotational frequency that depends on the centrifugal force and rotational speed. Hu et al. [121] located a nanogenerator of size $1.5 \text{ cm} \times 0.5 \text{ cm}$ in the inner surface of the car tire illustrated in Figure 21. The nanogenerator was designed to convert the mechanical energy of the tire's motion into electrical energy using piezoelectric films bender. The work was conducted experimentally by utilizing the bicycle tire instead of real tire for the sake of simplicity. As much as the nanogenerator bent due to the tire's deformation, the electric pulse was generated. The experimental results show that an output voltage of 1.5 V was generated with a travel distance of 12 mm and acceleration of 30 m/s^2 . The generated voltage could be stored in the battery or capacitor to power different electronic appliances. The study also concluded that the generated output voltage is directly proportional to the car speed, and the travel distance.



Figure 21: A nanogenerator NG in the inner surface of the tire [121].

According to Zhang et al. [122], the ceramic piezoelectric harvester was simplified as a uni-morph cantilever beam and mounted in the center of the rotating

car tire wheels as shown in Figure 22 (a). They have conducted experimental study in which a piezoelectric layer with dimensions of $7\text{ cm} \times 1.5\text{ cm} \times 1.5\text{ cm}$ was located at a shaker table with a frequency of $0 - 2000\text{ Hz}$ representing the tire rotation frequency. Figure 22 (b) represents the experimental setup that consists of energy harvester, shaker, accelerometer, and sensors. With a resistor of $252\text{ k}\Omega$, the system was able to capture a power of about 0.032 mW . In the actual test, the harvester was placed at the center of the front wheel tire of an electric car of type Coms, Toyota Auto Body. Piezoelectric harvester was connected to the wireless accelerometer and data acquisition system to measure the real output voltage per time. The test was conducted with different speeds of 10 km/h , 20 km/h , 30 km/h , and 40 km/h . The results show that, increasing the car speed resulted in increasing the collected power from the harvester until it reached approximately 0.017 mW . However, the highest average power among the four speeds occurred at a speed of 20 km/h for the case of stochastic resonance.

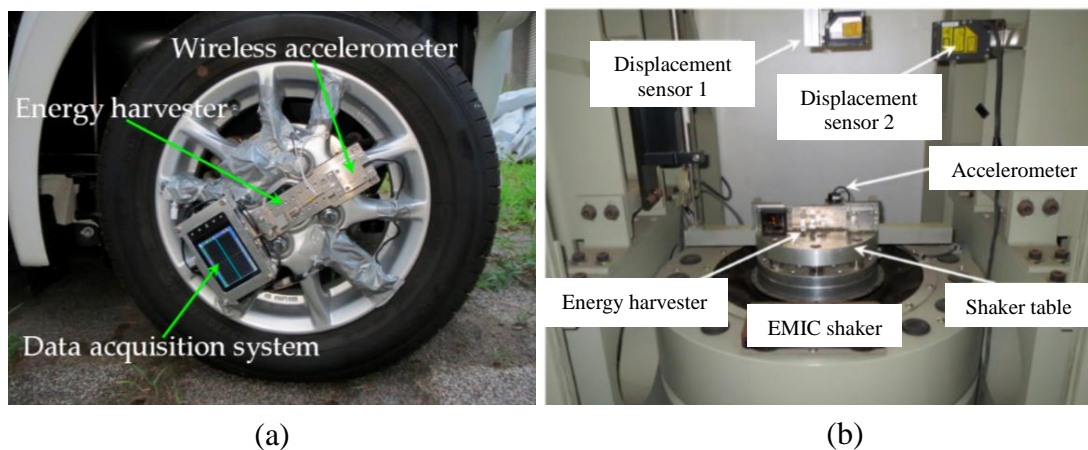


Figure 22: Energy harvester at the center of the tire. (a) The actual tire experiment. (b) The experimental setup [122].

The energy harvester proposed by Apollo project [123] was enough to generate a power of 0.9 mW by inserting a piezoelectric PVDF film inside the inner tire surface

at a speed of 80 km/h. A film of size 8 cm \times 8 cm was connected to the voltage converter circuit to convert the AC voltage to DC, as shown in Figure 23. The project concluded that the power output is linearly dependent on the piezoelectric film area, car wheel load, and its speed. Makki and Pop-Iliev [60] addressed three different piezoelectric energy harvesters illustrated in Figure 24. These are PZT unimorph bender mounted in the inner tire, PVDF thin sheet bonded to the tire, and PVDF ribbon attached to the tire bead. Among these three types, the PZT directly attached to the inner tire surface has the greatest power output of about 4.6 mW at a speed of 8 km/h. Moreover, PZT can withstand the high temperature of the tires without failure, and it is relatively cheap material (2 \$ per 25 mm diameter sheet).

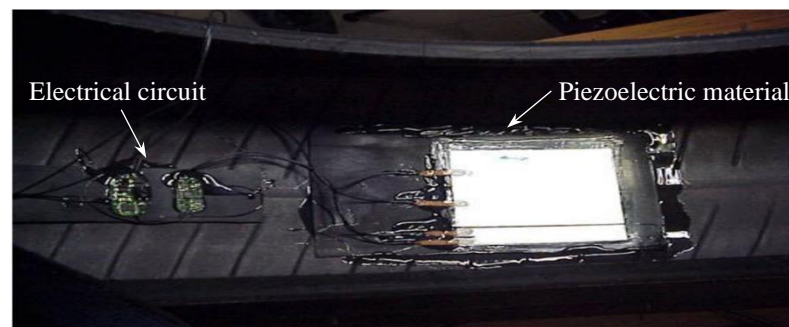


Figure 23: A piezoelectric material inside the tire surface at the right-hand side and its voltage converter circuit at the left-hand side [123].

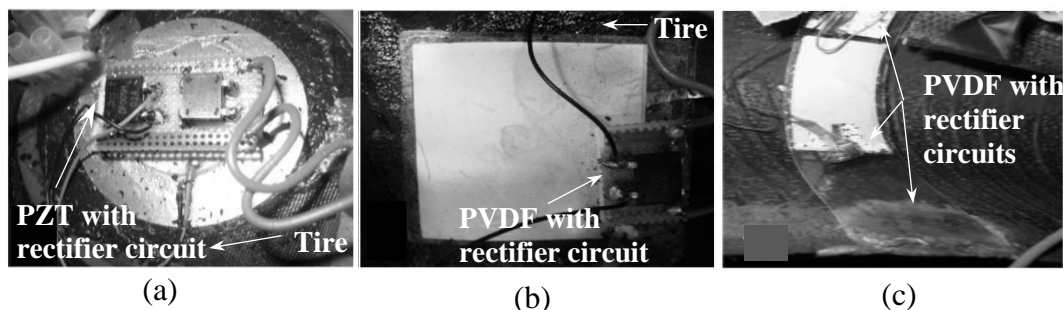


Figure 24: Three different piezoelectric energy harvesters. (a) Circular PZT bonded to the top circular tire. (b) PVDF element with rectifier circuit bonded to the tire. (c) Plastic ribbon with three PVDF bonded to the tire [60].

The piezoelectric material can be modeled as a new regenerative shock absorber in the CSS. Installing a piezoelectric material with the shock absorber helps in generating electricity as the piston compresses the damping fluid inside the shock absorber and creates a pressure that deforms the piezoelectric material. Several proposed designs apply the same concept. For instance, Lee et al. [124] modeled a regenerative shock absorber called PESHHA that is made of two piezoelectric layers stacked in the shock absorber. The system was able to produce an electric charge when exposed to vibrations that effect in changing in the fluid pressure induced by the piston displacement. Whereas, Lafarge et al. [125] focused on studying the effectiveness of the location of the piezoelectric material mounted on the shock absorber. The two proposed different locations are shown in

Figure 25. They found that locating PZT-5H between the two surfaces in the absorber (d_{33}) harvest more energy than locating it on the damper's surface (d_{31}).

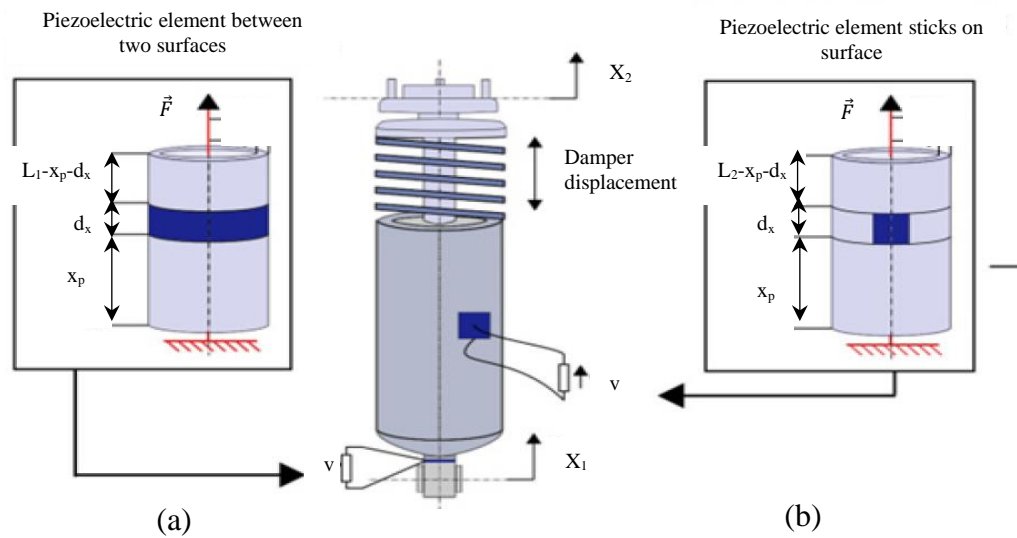


Figure 25: Piezoelectric material on the shock absorber. (a) Piezoelectric material between two surfaces. (b) Piezoelectric material on the damper surface [125].

Furthermore, Ali and Adhhikari [126] modeled a piezoelectric shock absorber as a single degree of freedom that is coupled to the electric circuit made of electrical

capacitance and resistance. The proposed system was excited by sinusoidal wave input with constant frequency, while, Madhav and Ali [127] subjected their model to the random input excitation. The aim of the two models (presented in Figure 26) were to find the optimal mechanical and electrical parameters in order to get the maximum power output and minimum system's vibrations.

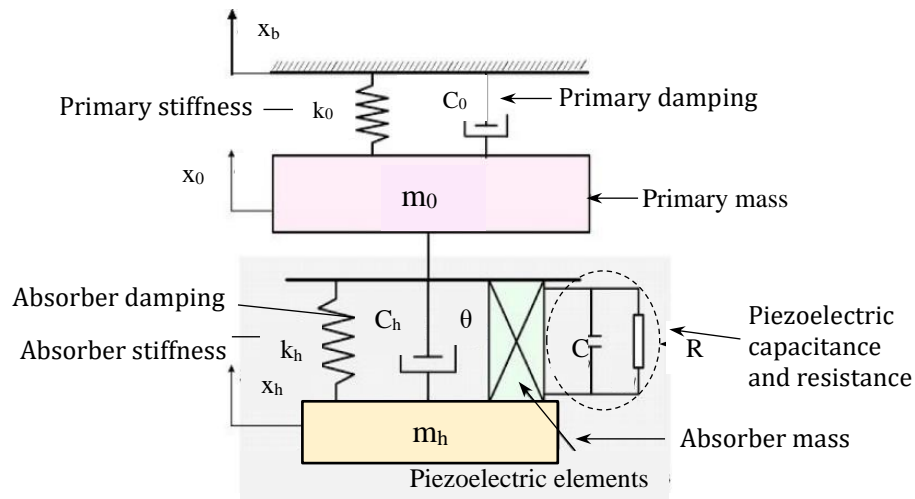


Figure 26: Energy harvesting system of piezoelectric vibration absorber [126], [127].

Some investigators used a multilayer piezoelectric stack as an alternative approach to increase the harvested energy. Arizti [128] modified the suspension shock absorber tube by installing the piezoelectric stack in the top of the piston as clearly shown in Figure 27. As the car passed over the bump, the energy from the piezoelectric stack of type PSt 1000/25/40 can be produced from the movement of the piston. The harvested voltage from one bump in the road was recorded as 17.69 mV. However, the harvested power from the proposed system was not calculated in this study. The study was also proposing the factors that were affecting the effectiveness of the piezoelectric stack as for examples, increasing the number of layers and/or the layer's thickness.

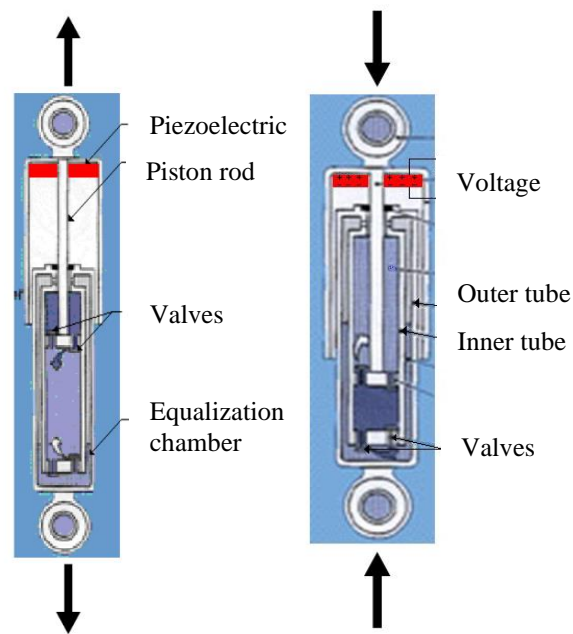


Figure 27: Piezoelectric stack inside the shock absorber tube [128].

Moreover, Hendrowati et al. [129] impeded a multilayer piezoelectric stack with the suspension system. A piezoelectric stack made of 15 layers was connected in series with the suspension spring in the QCM. Multilayer piezoelectric vibration energy harvesting (ML PZT VEH) used was based on transferring the vertical displacement of the suspension system into horizontal displacement to magnify the spring force applied on the piezoelectric stack. The proposed ML PZT VEH principle which is presented in Figure 28 helped increase the harvested power by a value of 7.17 times higher than the direct installing to the suspension system. Unlike Xiao et al. [115] and Al-Yafeai et al. [116] models, Hendrowati et al. [129] considered the stiffness coefficient of the piezoelectric stack in the calculations. However, the values of the stiffness coefficient, the piezoelectric dielectric permittivity ϵ_{33} , and the resistance R were not clearly specified.

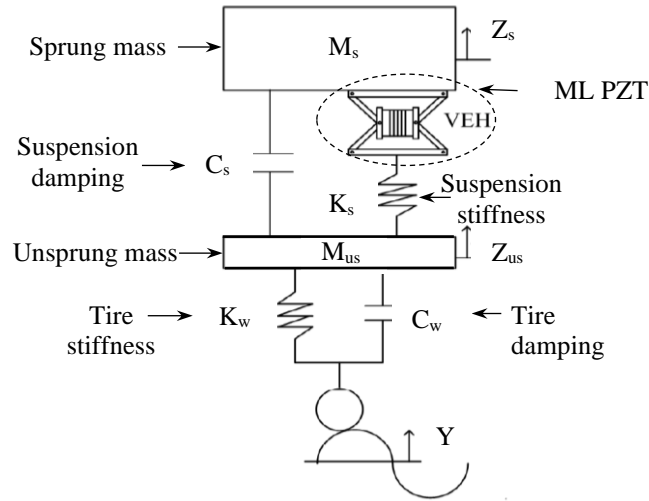


Figure 28: QCM with ML PZT VEH mechanism [129].

It is of importance to compare the different piezo element-based harvesters available in the literature up to date regardless of the specification of them. Table 6 summarizes the harvested energy obtained from the different CSS considered in the literature. The harvested systems are different in the configurations (cantilever and stack), locations of the piezoelectric element in the suspension system (springs, shock absorbers, and wheels), the suspension system models (quarter or half), and the road input excitation (harmonic or random). It can be noticed that the harvested power ranges from 0.001 mW to 3.9 W which is limited when compared with the available/dissipated energy. The main focus of some researchers was only on the evaluation of the dissipated energy from CSS not on the harvested energy [130]. Further, some researchers have evaluated the harvested energy using other techniques rather than piezoelectric-based techniques [130].

Table 6: Different energy harvesting of CSS with their specifications and important outcomes.

References	Type of Piezo	Location of Piezo	Car Model	Road Input	Excitation Speed/Acceleration /Frequency	Harvested Voltage	Harvested Power /Power Density	Dissipated Power
Xiao et al. [115] (2015)	PZT	Parallel with the suspension springs	QCM (2 DOF)	Harmonic	1.45 Hz	274.62 V	2.48 W	NA
Al-Yafeai et al. [116] (2019)	PZT	Parallel with the suspension springs	HCM (4 DOF)	Harmonic	1.45 Hz	486 V	3.9 W	NA
Xie and Wang [37] (2015)	PZT 4 bar	On suspension wheels	QCM (2 DOF)	Random rough road classes of B, C, & D	35 km/h	NA	NA	<u>Class B:</u> 40 W <u>Class C:</u> 162 W <u>Class D:</u> 652 W
Zhao et al. [117] (2019)	PZT 4	On suspension wheels	QCM (2 DOF)	Random road of class B	30 km/h	NA	NA	18.83 W
Lafarge et al. [118] (2018)	Cantilever beam made of two PZT 27 layers	Embedded to the wheels	QCM (2 DOF)	Random rough road	<u>Experimental test:</u> 91 Hz <u>Simulation:</u> 30 km/h <u>Real test:</u> 10 km/h & 30 km/h	<u>Experiment:</u> 13 V <u>Simulation:</u> 2 V <u>Real test:</u> @ 10 km/h: 1-2 V @ 30 km/h: 2-3 V	<u>Experiment:</u> 1.4 mW <u>Simulation:</u> 0.02 W <u>Real test:</u> @ 10 km/h: 0.001-0.021 mW @ 30 km/h: 0.01-0.07 mW	NA

Table 6: Different energy harvesting of CSS with their specifications and important outcomes (cont'd).

References	Type of Piezo	Location of Piezo	Car Model	Road Input	Excitation Speed/Acceleration /Frequency	Harvested Voltage	Harvested Power /Power Density	Dissipated Power
Behera [119] (2015)	32 PZT-5A arranged in three strips	Inner tires' circumference	NA	NA	40 km/h	NA	14 mW	NA
Hu et al. [121] (2011)	piezoelectric films bender	Inner surface of the tire	NA	NA	30 m/s ²	1.5 V	70 μ W/cm ²	NA
Zhang et al. [122] (2016)	Cantilever of ultrathin unimorph ceramic piezoelectric	Center of the tire	NA	Random on road noise	<u>Experimental test:</u> 6 Hz <u>Real test:</u> 20 km/h	NA	<u>Experimental lab. test:</u> 0.032 mW <u>Real car test:</u> 0.017 mW	NA
Apollo project [123] (2003)	PVDF	Inner tire surface	NA	NA	80 km/h	NA	0.9 mW	NA
Makki and Pop-Iliev [60] (2011)	<ul style="list-style-type: none"> • PZT unimorph bender • PVDF thin sheet • PVDF ribbon 	Inner tire	NA	NA	9 km/h	<ul style="list-style-type: none"> • 45.5 V • 62.3 V • 18.7 V 	<ul style="list-style-type: none"> • 4.6 mW • 0.85 mW • 0.23 mW 	NA
Lee et al. [124] (2013)	Two parallel plated of PZT 4	Shock absorber	1 DOF	NA	10 Hz	20 V	1.2 mW	NA

Table 6: Different energy harvesting of CSS with their specifications and important outcomes (cont'd).

References	Type of Piezo	Location of Piezo	Car Model	Road Input	Excitation Speed/Acceleration /Frequency	Harvested Voltage	Harvested Power /Power Density	Dissipated Power
Lafarge et al. [125] (2015)	PZT 5H	Shock absorber: • Stacked on the damper's surface d_{31} • Placed between two surfaces d_{33}	QCM (2 DOF)	NA	30 km/h	NA	<u>Mode d_{33}:</u> 6 mW <u>Mode d_{31}:</u> 3 mW	NA
Ali and Adhhikari [126] (2013)	Piezoelectric stack	Shock absorber	2 DOF	Sinusoidal excitation	NA	NA	6.5 (normalized power)	NA
Madhav and Ali [127] (2016)	Piezoelectric stack	Shock absorber	2 DOF	Random excitation	NA	NA	2.4 (normalized power)	NA
Arizti [128] (2010)	PZT stack	Shock absorber	NA	NA	NA	17.69 mV	NA	NA
Hendrowati et al. [129] (2012)	PZT stack	Series with the suspension's spring	QCM (2 DOF)	Harmonic excitation	43.2 km/h	6.23 V	1.6 mW	NA

2.5 Electronic circuit of piezoelectric harvesting system

The harvested energy from the piezoelectric material must be accumulated and stored. Without this stage, the resultant harvested power will be dissipated with no utilization. Having a piezoelectric energy harvester requires a rectifier circuit in order to convert the AC wave from the harvester to the DC voltage which is suitable for energy storage. The most simple and common rectifier circuit used in the literature was the full-wave rectifier with diode bridge [131]–[134]. The output voltage from the piezoelectric element will be first rectified and then accumulated through the large smoothing capacitor. The smoothing capacitor is placed in parallel with the battery to be charged. The schematic diagram of the piezoelectric harvesting circuit is shown in Figure 29.

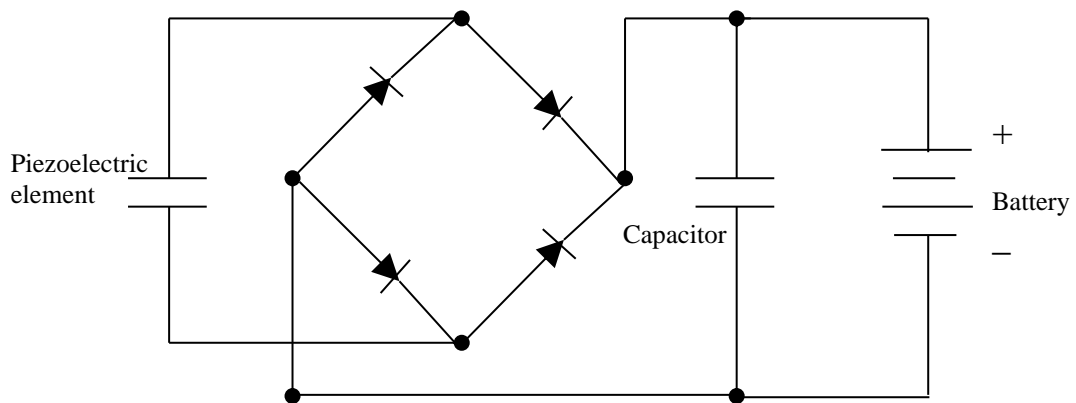


Figure 29: Schematic of battery charging circuit.

After rectification, some researchers were focused on developing the harvesting energy circuits to feed the batteries or the external electronic load by having voltage regulators. The voltage regulators could be a step-up or step-down converter. For instance, Ottman et al. [135] developed a harvesting circuit made from the ac-dc rectifier, capacitor, and electrochemical battery. An additional switch mode dc-dc step-down converter was added to the circuit to control the energy flow to the battery. The

control technique of the converter helps in varying the switching frequency to increase the current flow to the battery and adjusted the duty cycle. The corresponding harvesting circuit was implemented in bimorph piezoelectric bender and showed that the power was increased by 400% when compared to the circuit with no dc-dc step-down converter. Yet, the corresponding control circuit required more power than the power generated by the piezoelectric element. Consequently, Hofmann et al. [136] used the same circuit of Ottman et al. [135] but with a fixed duty cycle to maximize the harvested power. The tested optimal duty cycle experimentally agreed with the analytical value of 2.81%. The results also showed that, the harvested power from the proposed circuit was increased up to 30.66 mW which is over three times the direct charging of the battery.

The harvested energy from the piezoelectric material is not sufficient to directly power the electronic appliances. It needs a mode of storing device before utilizing it. This could be done by having a capacitor or a rechargeable battery. Having capacitors as an energy storage device was studied by many researchers [137]–[140]. Due to their high-power density, they charged and discharged very rapidly, making them more applicable for only rapid energy transfer systems. However, most of the literature work concluded that, using capacitors as a storage device was not an efficient method when compared to the rechargeable batteries. This was also confirmed by Sodano and his team [141] who tested the piezoelectric plates with two different storage devices; capacitor and battery. It was found that using a rechargeable battery resulted in better power efficiency and storage. Using a battery as a storage source will allow a large variety of electronic devices to be powered when compared to the capacitor due to its quick discharge rate. However, the batteries have a limited number of charging cycles. Chen et al. [142] mentioned the following batteries with their

lifetime cycles, Lead Acid (500 – 1000 cycles), Nickel Cadmium (2000 – 2500 cycles), Sodium Sulphur (2500 cycles), Lithium-Ion (up to 10,000 cycles). After the corresponding life cycles, the battery's capacity significantly falls under 80% of its original capacity.

Another new approach for a storage medium rather than the conventional capacitor or battery is using supercapacitors [143]–[145]. Supercapacitors, also called ultracapacitor, have a capacitance and stored energy much higher than the conventional one. Also, their cycle life compared to the electrochemical batteries could reach up to 10^6 cycles [146]. Guan and Liao [147] conducted a comparison study of supercapacitors with the rechargeable batteries. The experimental setup with different storage devices is shown in Figure 30. They reported that, the charge/discharge efficiencies of the supercapacitors compared to the Lithium-Ion and Nickel Metal batteries were 95%, 92%, and 65%, respectively. However, the self-discharge rate of the ultracapacitors was high compared to the electrochemical batteries that were resulting in losing most of their stored energy within few days [108], [114], [115]. One of the solutions proposed by Tolentino and Talampas [150] was to combine the rechargeable battery with the supercapacitor as an energy storage unit. They used the Lithium-Ion battery as a primary storage unit while the supercapacitor as a secondary unit for achieving a higher power output than having only one of them.

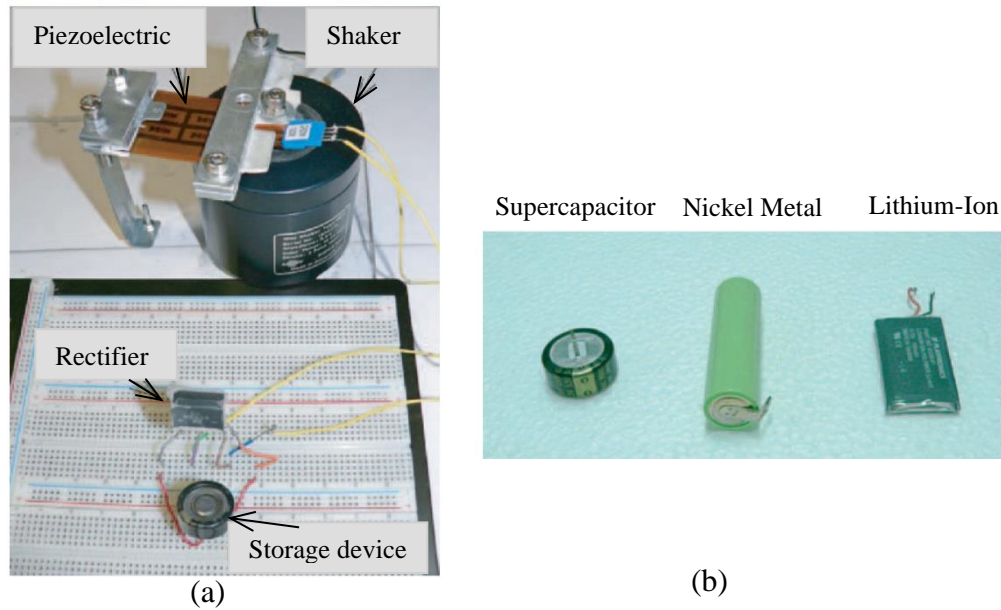


Figure 30: Piezoelectric energy harvesting system. (a) Experimental set up. (b) Different storage devices [147].

2.6 Utilization of the harvested energy

Nowadays, micro-electro-mechanical systems (MEMS) and wireless technology have been identified as one of the most promising technologies for the 21st century. Different types of wireless sensors could be placed everywhere. Thus, it is necessary to have their own power supply rather than the traditional electrochemical batteries. Powering remote sensors through piezoelectric material providing endless energy for the sensor's lifespan. Various sensors could be utilized in different applications, such as industrial, medical, and commercial applications. For instance, using wireless remote sensors to provide a smart lighting system, monitor sleep and heart beating, and monitor public infrastructures like roads and bridges. Some of the worldwide countries such as USA (California), and Italy have proposed the piezoelectric energy-generating roads by placing the piezoelectric materials underneath the roads in order to utilize the harvested electrical energy in powering the

road signs and lights [151], [152]. Also, Japan has been established the idea of harvesting energy via piezoelectric material. In Japan station, the piezoelectric materials were placed under the ticket gates. The harvested energy from passengers walk was utilized in order to run the automatic ticket gates and electronic displays [77].

Furthermore, the vibrations generated from the car's travel can be converted into electricity to be either utilized or stored in a battery. The utilization of the harvested energy is considered in powering various appliances like car sensors, smartphones, smartwatches, etc. Besides, the battery that stored the harvested energy could act temporarily in emergency cases. For example, in case of shutting off the car's, the spare battery will help to jump-start the car. Many other applications may also be found in the new car generations.

Chapter 3: Mathematical Models

3.1 Mathematical models without piezoelectric stack

The mathematical model for the pure mechanical system will be conducted for both quarter and HCM. The procedures of modeling the mechanical systems theoretically and experimentally will be discussed in the following sections.

3.1.1 Quarter car model (QCM)

The simplest representation of the real car is modeling it as a QCM. It examines only the vertical vibrations of the car body (bouncing) which can be useful for preliminary design. The two degrees of freedom system in a QCM (shown in Figure 31) represents the one-fourth of the car, and it consists of two solid masses known as sprung and unsprung masses. The sprung mass M_s represents a quarter of the car body, and the unsprung mass M_{us} represents one car tire assembly. The primary suspension which is made of the spring K_s and linear viscous damper b_s is supporting the sprung mass. Whereas, the unsprung mass is in direct contact with the road surface through spring and damper that represent the tire stiffness K_{us} and tire absorptivity b_{us} respectively. The car is excited by the road excitation Y_R which will cause the vertical displacement of the car body Y_s as well as the tire Y_{us} . The QCM can be easily modeled applying Newton's 2nd law. The two equations of motion of two DOF are illustrated as follows (note that the system is in stable equilibrium),

The equation of the vertical motion of the unsprung mass

$$M_{us}\ddot{Y}_{us} = K_s(Y_s - Y_{us}) + b_s(\dot{Y}_s - \dot{Y}_{us}) - K_{us}(Y_{us} - Y_R) - b_{us}(\dot{Y}_{us} - \dot{Y}_R) \quad (8)$$

The equation of the vertical motion of the sprung mass

$$M_s \ddot{Y}_s = -K_s(Y_s - Y_{us}) - b_s(\dot{Y}_s - \dot{Y}_{us}) \quad (9)$$

where:

\dot{Y}_s , \dot{Y}_{us} , and \dot{Y}_R are the velocity of the sprung, unsprung, and road, respectively.

\ddot{Y}_s , \ddot{Y}_{us} , and \ddot{Y}_R are the acceleration of the sprung, unsprung, and road, respectively.

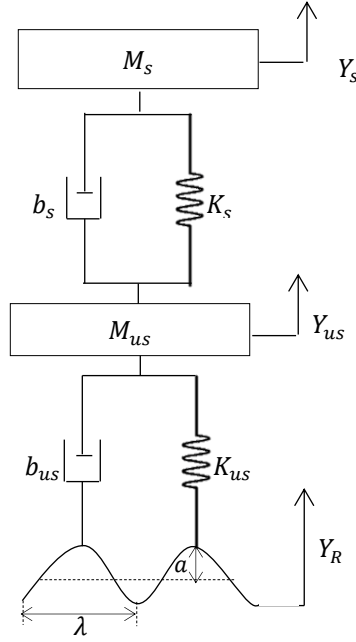


Figure 31: Quarter car model (QCM).

3.1.2 Half car model (HCM)

HCM is represented as four DOF that consists of the bounce Y_s and pitch motion θ_s of the car body and the vertical translations of the front Y_{uf} and rear axles Y_{ur} . Half car body is connected to the front and rear tires and that is represented in Figure 32. The sprung mass M_s is free to bounce and pitch. While, the front M_{uf} and rear M_{ur} unsprung masses are free to bounce vertically with respect to the half car body. The front and rear suspension systems between the sprung mass and unsprung masses are modeled as front and rear linear viscous dampers (b_{sf} and b_{sr}) and springs

(K_{sf} and K_{sr}), whereas, the both tires are modelled as linear springs (K_{uf} and K_{ur}) and dampers (b_{uf} and b_{ur}). The four equations of motion are derived as follows

The equation of the vertical motion of the front unsprung mass

$$\begin{aligned} M_{uf}\ddot{Y}_{uf} = & -K_{uf}(Y_{uf} - Y_{Rf}) - b_{uf}(\dot{Y}_{uf} - \dot{Y}_{Rf}) + K_{sf}(Y_s - L_f\theta_s - Y_{uf}) \\ & + b_{sf}(\dot{Y}_s - L_f\dot{\theta}_s - \dot{Y}_{uf}) \end{aligned} \quad (10)$$

The equation of the vertical motion of the rear unsprung mass

$$\begin{aligned} M_{ur}\ddot{Y}_{ur} = & -K_{ur}(Y_{ur} - Y_{Rr}) - b_{ur}(\dot{Y}_{ur} - \dot{Y}_{Rr}) + K_{sr}(Y_s + L_r\theta_s - Y_{ur}) \\ & + b_{sr}(\dot{Y}_s + L_r\dot{\theta}_s - \dot{Y}_{ur}) \end{aligned} \quad (11)$$

The equation of the vertical motion of the sprung mass

$$\begin{aligned} M_s\ddot{Y}_s = & -K_{sf}(Y_s - L_f\theta_s - Y_{uf}) - b_{sf}(\dot{Y}_s - L_f\dot{\theta}_s - \dot{Y}_{uf}) \\ & - K_{sr}(Y_s + L_r\theta_s - Y_{ur}) - b_{sr}(\dot{Y}_s + L_r\dot{\theta}_s - \dot{Y}_{ur}) \end{aligned} \quad (12)$$

The equation of the angular motion of the sprung mass

$$\begin{aligned} I_s\ddot{\theta}_s = & L_f[K_{sf}(Y_s - L_f\theta_s - Y_{uf}) + b_{sf}(\dot{Y}_s - L_f\dot{\theta}_s - \dot{Y}_{uf})] \\ & - L_r[K_{sr}(Y_s + L_r\theta_s - Y_{ur}) + b_{sr}(\dot{Y}_s + L_r\dot{\theta}_s - \dot{Y}_{ur})] \end{aligned} \quad (13)$$

All symbols used in the equations are presented in the nomenclature.

The road profile is approximated by harmonic acceleration excitation that excites the car front tire $\ddot{Y}_{Rf}(t)$ and the rear tire with the following delayed function

$\ddot{Y}_{Rr}(t)$:

$$\ddot{Y}_{Rr}(t) = \ddot{Y}_{Rf}(t - \tau) \text{ where } \ddot{Y}_{Rf}(t) = a \sin(\omega t) \quad (14)$$

In the above equation, a is the acceleration amplitude of the sine wave, ω is the angular frequency, and τ is the time delay $\tau = \frac{L}{u}$ as given by, where L and u are the car wheelbase and velocity, respectively.

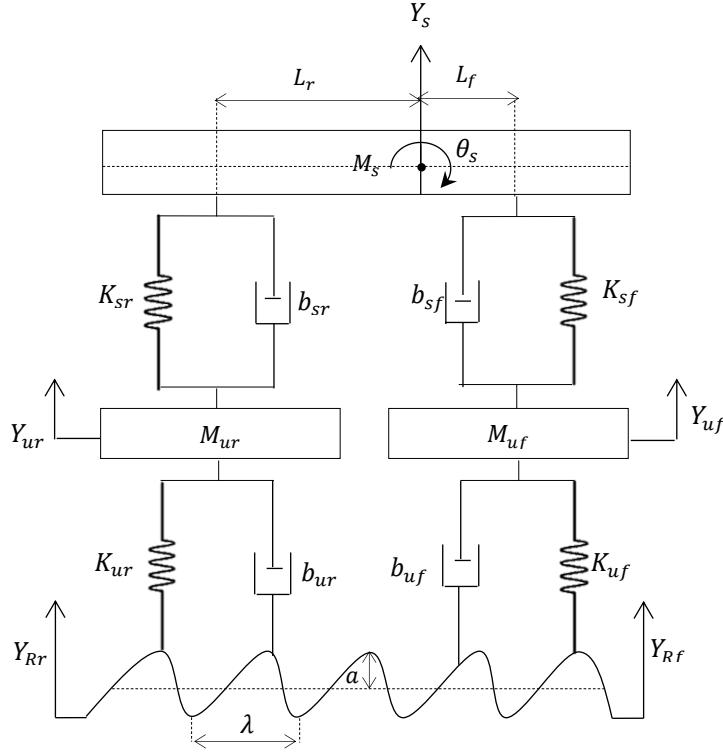


Figure 32: Half car model (HCM).

3.2 Mathematical models with piezoelectric stack

The governing equations of the electromechanical model having piezoelectric harvester stacks mounted in series with suspension spring are derived. The derived governing equations for both quarter and half car models are presented in Laplace transformation and illustrated in the following sections.

3.2.1 Piezoelectric stack model

As discussed previously in the chapter 2, the location of the piezoelectric stack will significantly affect the harvested power. In this study, the piezoelectric stack

element will be connected in series with the sprung stiffness in order to not affecting the mechanical performance of the suspension system. Whereas having a piezoelectric stack in parallel connection with the suspension spring increases the equivalent suspension system stiffness and consequently affects the ride quality and comfortability. Figure 33 shows the equivalent stiffness in both cases. The equivalent stiffness in the series connection will be approximately equal to the stiffness of the sprung mass as if there is no piezoelectric stack.

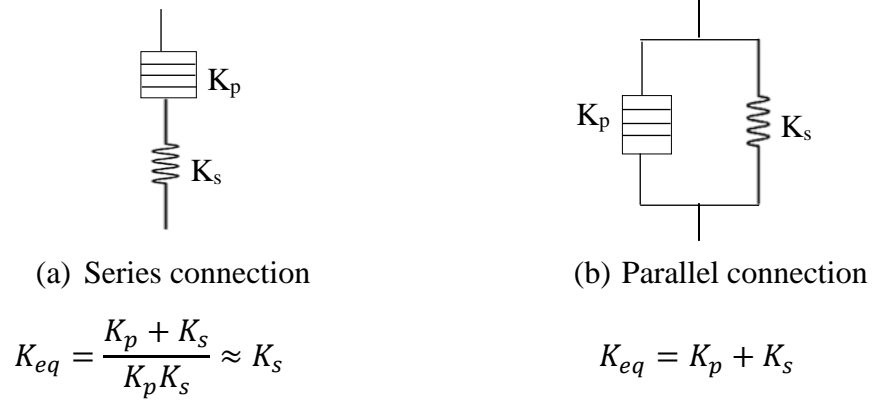


Figure 33: Equivalent stiffness in different connections. (a) Series. (b) Parallel connections.

The mathematical representation of the piezoelectric element is mainly expressed as the resorting force in the piezoelectric stack element and the output current from the piezoelectric material i_p . The restoring force in equation (20) consists of the mechanical and electrical forces with neglecting the effect of piezoelectric damping. The electric circuit is included in order to collect and store the energy converted from the vibration energy. The integrated circuit shown in Figure 34 composed of the piezoelectric material that is modelled as a piezoelectric capacitance C_p and resistance R_p with the output AC voltage V_p connected to the external circuit. The external rectified circuit consists of the bridge rectifier made of four ideal silicon diodes to obtain the output DC voltage V connected to the smoothing capacitor C_p and

external load R_e . The smoothing capacitor is utilized to reduce the ripple of the output AC-DC signal.

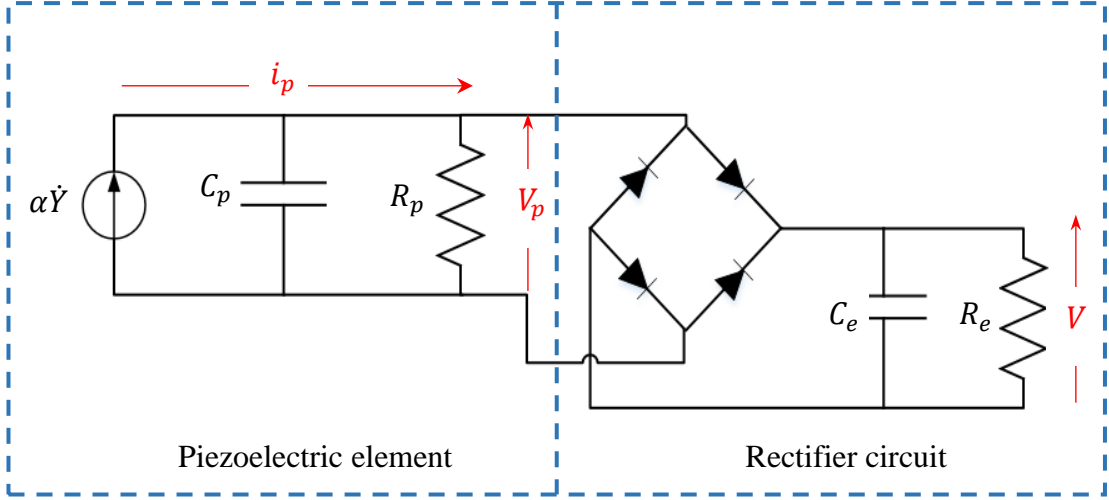


Figure 34: Piezoelectric energy harvesting circuit.

For the piezoelectric element, the relationship between the electrical and mechanical variables can be derived as follows [153]:

$$F_p = K_p Y_p(t) + \alpha V_p(t) \quad (15)$$

$$i_p = \alpha \dot{Y}_p - C_p \dot{V}_p \quad (16)$$

where the featuring quantities are the short circuit stiffness of piezoelectric stack material K_p , the relative displacement between the sprung and unsprung masses Y_p , and the force factor α . The mathematical expression of these quantities are illustrated in equations (17) - (19) which are defined as a function of the piezoelectric parameters presented in Table 7.

$$K_p = \frac{E_p A_p}{l_p} \quad (17)$$

$$\alpha = d_{33} E_p \frac{A_p}{h_p} \quad (18)$$

$$C_p = N \frac{\epsilon_{33} A_p}{h_p} \quad (19)$$

where A_p and h_p are the surface area and thickness of one layer of the piezoelectric stack and the total length of the stack is defined by the following equation.

$$l_p = N h_p \quad (20)$$

Table 7: Piezoelectric parameters [154].

Parameter	Value	Unit
E_{33}	53	GPa
d_{33}	600	pm/V
ϵ_{33}	39.975	nF/m

When a piezoelectric voltage is equal to the output rectified voltage, the diodes conduct, and the current i_p flows from the piezo stack into the external rectifier circuit that can be identified as

$$i_p = \begin{cases} C_e \dot{V} + \frac{V}{R_e} & \text{if } V_p = V \\ -C_e \dot{V} - \frac{V}{R_e} & \text{if } V_p = -V \\ 0 & \text{if } |V_p| < V \end{cases} \quad (21)$$

From piezoelectric harvesting circuit shown in Figure 34, the resistors and capacitors are connected in parallel. As the piezoelectric resistance is much higher than the external load resistance, the equivalent resistance R is equal to the external resistance $R \approx R_e$. It is also assumed that the smoothing capacitor C_e is enormous compared to the piezoelectric capacitance C_p ; thus the DC rectified voltage is approximated as a constant over a cycle [155], [156]. The equivalent capacitance equals to the piezoelectric capacitance $C \approx C_p$. The external load is modelled as a constant current source, and the four diodes are assumed to exhibit the ideal behaviour

which means the diode drop is negligible [157]. As a result, the piezoelectric harvesting circuit can be simplified as the equivalent electric circuit as shown in Figure 35 and equation (22).

$$\frac{V}{R} = \alpha \dot{Y}(t) - C \dot{V}(t) \quad (22)$$

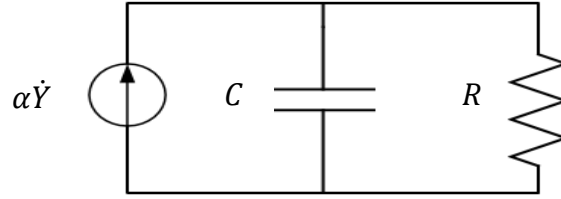


Figure 35: Equivalent electric circuit.

3.2.2 Quarter car model (QCM) with PZT stack

The quarter car model with piezoelectric stack connected in series with the suspension springs is shown in Figure 36. The equations of motion in Laplace transformation are illustrated as the following:

The equation of vertical motion of the unsprung mass:

$$\begin{aligned} M_{us} \ddot{Y}_{us} = & -K_{us}(Y_{us} - Y_R) - b_{us}(\dot{Y}_{us} - \dot{Y}_R) + K_s(Y_p - Y_{us}) \\ & + b_s(\dot{Y}_s - \dot{Y}_{us}) \end{aligned} \quad (23)$$

Applying Laplace transformation:

$$\begin{aligned} [M_{us}s^2 + (b_{us} + b_s)s + (K_{us} + K_s)]Y_{us} \\ = (b_{us}s + K_{us})Y_R + (b_s s)Y_s + (K_s)Y_p \end{aligned} \quad (24)$$

The vertical displacement of the unsprung mass can be written as:

$$Y_{us} = A_1 Y_R + A_2 Y_s + A_3 Y_p \quad (25)$$

where

$$A_1 = \left[\frac{b_{us}s + K_{us}}{M_{us}s^2 + (b_{us} + b_s)s + (K_{us} + K_s)} \right]$$

$$A_2 = \left[\frac{b_s s}{M_{us}s^2 + (b_{us} + b_s)s + (K_{us} + K_s)} \right]$$

$$A_3 = \left[\frac{K_s}{M_{us}s^2 + (b_{us} + b_s)s + (K_{us} + K_s)} \right]$$

The equation of vertical motion of the quarter sprung mass:

$$M_s \ddot{Y}_s = -b_s(\dot{Y}_s - \dot{Y}_{us}) - K_p(Y_s - Y_p) - \alpha V_p \quad (26)$$

Applying Laplace transformation:

$$[M_s s^2 + b_s s + K_p] Y_s = (b_s s) Y_{us} + (K_p) Y_p - (\alpha) V_p \quad (27)$$

The vertical displacement of the unsprung mass can be written as:

$$Y_s = A_4 Y_{us} + A_5 Y_p - A_6 V_p \quad (28)$$

where

$$A_4 = \left[\frac{b_s s}{M_s s^2 + b_s s + K_p} \right]$$

$$A_5 = \left[\frac{K_p}{M_s s^2 + b_s s + K_p} \right]$$

$$A_6 = \left[\frac{\alpha}{M_s s^2 + b_s s + K_p} \right]$$

The equation of the piezoelectric element:

$$M_p \ddot{Y}_p = -K_s(Y_p - Y_{us}) + K_p(Y_s - Y_p) + \alpha V_p \quad (29)$$

Applying Laplace transformation:

$$[M_p s^2 + (K_s + K_p)]Y_p = (K_s)Y_{us} + (K_p)Y_s + (\alpha)V_p \quad (30)$$

The vertical displacement of the sprung mass can be written as:

$$Y_p = A_7 Y_{us} + A_8 Y_s + A_9 V_p \quad (31)$$

where

$$A_7 = \left[\frac{K_s}{M_p s^2 + (K_s + K_p)} \right]$$

$$A_8 = \left[\frac{K_p}{M_p s^2 + (K_s + K_p)} \right]$$

$$A_9 = \left[\frac{\alpha}{M_p s^2 + (K_s + K_p)} \right]$$

The governing equations for the equivalent electrical system as derived in equation (22) can be modified and written separately in Laplace transformation as:

$$V = \alpha R(\dot{Y}_s - \dot{Y}_p) - CR\dot{V} \quad (32)$$

Applying Laplace transformation:

$$(CRs + 1)V = (\alpha Rs)Y_s - (\alpha Rs)Y_p \quad (33)$$

The harvested voltage and power are

$$V = A_{10}Y_s - A_{10}Y_p \quad (34)$$

$$P = \frac{V^2}{R} \quad (35)$$

where

$$A_{10} = \left[\frac{\alpha R s}{C R s + 1} \right]$$

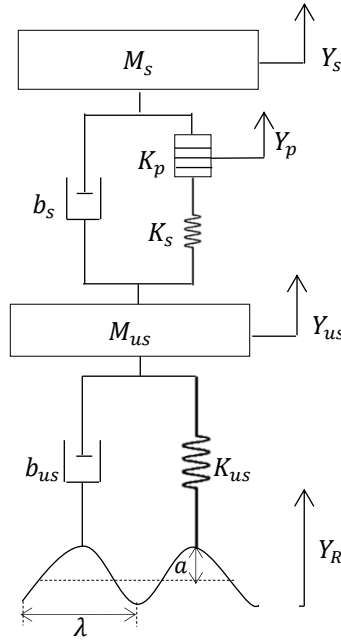


Figure 36: QCM with PZT stack.

3.2.3 Half car model (HCM) with PZT stack

The half car model with piezoelectric stack connected in series with the front and rear suspension springs is shown in Figure 37. The equations of motion in Laplace transformation are illustrated as the following:

The equation of vertical motion of the front unsprung mass:

$$\begin{aligned} M_{uf} \ddot{Y}_{uf} = & -b_{uf}(\dot{Y}_{uf} - \dot{Y}_{Rf}) - K_{uf}(Y_{uf} - Y_{Rf}) + b_{sf}(\dot{Y}_s - L_f \dot{\theta}_s - \dot{Y}_{uf}) \\ & + K_{sf}(Y_{pf} - Y_{uf}) \end{aligned} \quad (36)$$

Applying Laplace transformation:

$$\begin{aligned} [M_{uf}s^2 + (b_{sf} + b_{tf})s + (K_{sf} + K_{tf})]Y_{uf} \\ = (b_{uf}s + K_{uf})Y_{Rf} + (b_{sf}s)Y_s - (b_{sf}L_f s)\theta_s + (K_{sf})Y_{pf} \end{aligned} \quad (37)$$

The vertical displacement of the front unsprung mass can be written as:

$$Y_{uf} = A_{11}Y_{Rf} + A_{12}Y_s - A_{13}\theta_s + A_{14}Y_{pf} \quad (38)$$

where

$$A_{11} = \left[\frac{b_{uf}s + K_{uf}}{M_{uf}s^2 + (b_{sf} + b_{tf})s + (K_{sf} + K_{tf})} \right]$$

$$A_{12} = \left[\frac{b_{sf}s}{M_{uf}s^2 + (b_{sf} + b_{tf})s + (K_{sf} + K_{tf})} \right]$$

$$A_{13} = \left[\frac{b_{sf}L_f s}{M_{uf}s^2 + (b_{sf} + b_{tf})s + (K_{sf} + K_{tf})} \right]$$

$$A_{14} = \left[\frac{K_{sf}}{M_{uf}s^2 + (b_{sf} + b_{tf})s + (K_{sf} + K_{tf})} \right]$$

The equation of vertical motion of the rear unsprung mass:

$$\begin{aligned} M_{ur}\ddot{Y}_{ur} = -b_{ur}(\dot{Y}_{ur} - \dot{Y}_{Rr}) - K_{ur}(Y_{ur} - Y_{Rr}) + b_{sr}(\dot{Y}_s + L_r\dot{\theta}_s - \dot{Y}_{ur}) \\ + K_{sr}(Y_{pr} - Y_{ur}) \end{aligned} \quad (39)$$

Applying Laplace transformation:

$$\begin{aligned} (M_{ur}s^2 + (b_{sr} + b_{ur})s + (K_{sr} + K_{ur}))Y_{ur} \\ = (b_{ur}s + K_{ur})Y_{Rr} + (b_{sr}L_r s)\theta_s + (K_{sr})Y_{pr} + (b_{sr}s)Y_s \end{aligned} \quad (40)$$

The vertical displacement of the rear unsprung mass can be written as:

$$Y_{ur} = A_{15}Y_{Rr} + A_{16}\theta_s + A_{17}Y_{pr} + A_{18}Y_s \quad (41)$$

where

$$A_{15} = \left[\frac{b_{ur}s + K_{ur}}{M_{ur}s^2 + (b_{sr} + b_{ur})s + (K_{sr} + K_{ur})} \right]$$

$$A_{16} = \left[\frac{b_{sr}L_r s}{M_{ur}s^2 + (b_{sr} + b_{ur})s + (K_{sr} + K_{ur})} \right]$$

$$A_{17} = \left[\frac{K_{sr}}{M_{ur}s^2 + (b_{sr} + b_{ur})s + (K_{sr} + K_{ur})} \right]$$

$$A_{18} = \left[\frac{b_{sr}s}{M_{uf}s^2 + (b_{sf} + b_{tf})s + (K_{sf} + K_{tf})} \right]$$

The equation of vertical motion of the half-sprung mass:

$$\begin{aligned} M_s \ddot{Y}_s = & -b_{sf}(\dot{Y}_s - L_f \dot{\theta}_s - \dot{Y}_{uf}) - b_{sr}(\dot{Y}_s + L_r \dot{\theta}_s - \dot{Y}_{ur}) \\ & - K_{pf}(Y_s - L_f \theta_s - Y_{pf}) - K_{pr}(Y_s + L_r \theta_s - Y_{pr}) \\ & - (\alpha)V_{pf} - (\alpha)V_{pr} \end{aligned} \quad (42)$$

Applying Laplace transformation:

$$\begin{aligned} & (M_s s^2 + (b_{sf} + b_{sr})s + (K_{pf} + K_{pr}))Y_s \\ & = ((b_{sf}L_f - b_{sr}L_r)s + (K_{pf}L_f - K_{pr}L_r))\theta_s + (b_{sf}s)Y_{uf} \\ & + (b_{sr}s)Y_{ur} + (K_{pf})Y_{pf} + (K_{pr})Y_{pr} - (\alpha)V_{pf} - (\alpha)V_{pr} \end{aligned} \quad (43)$$

The vertical displacement of the sprung mass can be written as:

$$Y_s = A_{19}\theta_s + A_{20}Y_{uf} + A_{21}Y_{ur} + A_{22}Y_{pf} + A_{23}Y_{pr} - A_{24}V_{pf} - A_{24}V_{pr} \quad (44)$$

where

$$A_{19} = \left[\frac{(b_{sf}L_f - b_{sr}L_r)s + (K_{pf}L_f - K_{pr}L_r)}{M_s s^2 + (b_{sf} + b_{sr})s + (K_{pf} + K_{pr})} \right]$$

$$A_{20} = \left[\frac{b_{sf}s}{M_s s^2 + (b_{sf} + b_{sr})s + (K_{pf} + K_{pr})} \right]$$

$$A_{21} = \left[\frac{b_{sr}s}{M_s s^2 + (b_{sf} + b_{sr})s + (K_{pf} + K_{pr})} \right]$$

$$A_{22} = \left[\frac{K_{pf}}{M_s s^2 + (b_{sf} + b_{sr})s + (K_{pf} + K_{pr})} \right]$$

$$A_{23} = \left[\frac{K_{pr}}{M_s s^2 + (b_{sf} + b_{sr})s + (K_{pf} + K_{pr})} \right]$$

$$A_{24} = \left[\frac{\alpha}{M_s s^2 + (b_{sf} + b_{sr})s + (K_{pf} + K_{pr})} \right]$$

The equation of angular motion of the half-sprung mass:

$$\begin{aligned} I_s \ddot{\theta}_s = & L_f (b_{sf}(\dot{Y}_s - L_f \dot{\theta}_s - \dot{Y}_{uf}) + K_{pf}(Y_s - L_f \theta_s - Y_{pf}) + \alpha V_{pf}) \\ & - L_r (b_{sr}(\dot{Y}_s + L_r \dot{\theta}_s - \dot{Y}_{ur}) + K_{pr}(Y_s + L_r \theta_s - Y_{pr}) \\ & + \alpha V_{pr}) \end{aligned} \quad (45)$$

Applying Laplace transformation:

$$\begin{aligned}
& \left(I_s s^2 + (b_{sf} L_f^2 + b_{sr} L_r^2) s + (K_{pf} L_f^2 + K_{pr} L_r^2) \right) \theta_s \\
&= \left((b_{sf} L_f - b_{sr} L_r) s + (K_{pf} L_f - K_{pr} L_r) \right) Y_s \\
&\quad - (b_{sf} L_f s) Y_{uf} + (b_{sr} L_r s) Y_{ur} - (K_{pf} L_f) Y_{pf} \\
&\quad + (K_{pr} L_r) Y_{pr} + (\alpha L_f) V_{pf} - (\alpha L_r) V_{pr}
\end{aligned} \tag{46}$$

The angular displacement of the sprung mass can be written as:

$$\theta_s = A_{25} Y_s - A_{26} Y_{uf} + A_{27} Y_{ur} - A_{28} Y_{pf} + A_{29} Y_{pr} + A_{30} V_{pf} - A_{31} V_{pr} \tag{47}$$

where

$$A_{25} = \left[\frac{(b_{sf} L_f - b_{sr} L_r) s + (K_{pf} L_f - K_{pr} L_r)}{I_s s^2 + (b_{sf} L_f^2 + b_{sr} L_r^2) s + (K_{pf} L_f^2 + K_{pr} L_r^2)} \right]$$

$$A_{26} = \left[\frac{b_{sf} L_f s}{I_s s^2 + (b_{sf} L_f^2 + b_{sr} L_r^2) s + (K_{pf} L_f^2 + K_{pr} L_r^2)} \right]$$

$$A_{27} = \left[\frac{b_{sr} L_r s}{I_s s^2 + (b_{sf} L_f^2 + b_{sr} L_r^2) s + (K_{pf} L_f^2 + K_{pr} L_r^2)} \right]$$

$$A_{28} = \left[\frac{K_{pf} L_f}{I_s s^2 + (b_{sf} L_f^2 + b_{sr} L_r^2) s + (K_{pf} L_f^2 + K_{pr} L_r^2)} \right]$$

$$A_{29} = \left[\frac{K_{pr} L_r}{I_s s^2 + (b_{sf} L_f^2 + b_{sr} L_r^2) s + (K_{pf} L_f^2 + K_{pr} L_r^2)} \right]$$

$$A_{30} = \left[\frac{\alpha L_f}{I_s s^2 + (b_{sf} L_f^2 + b_{sr} L_r^2) s + (K_{pf} L_f^2 + K_{pr} L_r^2)} \right]$$

$$A_{31} = \left[\frac{\alpha L_r}{I_s s^2 + (b_{sf} L_f^2 + b_{sr} L_r^2) s + (K_{pf} L_f^2 + K_{pr} L_r^2)} \right]$$

The equation of the front and rear piezoelectric elements:

Front piezoelectric stack:

$$M_{pf}\ddot{Y}_{pf} = -K_{sf}(Y_{pf} - Y_{uf}) + K_{pf}(Y_s - L_f\theta_s - Y_{pf}) + (\alpha)V_{pf} \quad (48)$$

Applying Laplace transformation:

$$\begin{aligned} (M_{pf}s^2 + (K_{sf} + K_{pf}))Y_{pf} \\ = (K_{sf})Y_{uf} + (K_{pf})Y_s - (K_{pf}L_f)\theta_s + (\alpha)V_{pf} \end{aligned} \quad (49)$$

The vertical displacement of the front piezoelectric stack can be written as

$$Y_{pf} = A_{32}Y_{uf} + A_{33}Y_s - A_{34}\theta_s + A_{35}V_{pf} \quad (50)$$

where

$$A_{32} = \left[\frac{K_{sf}}{M_{pf}s^2 + (K_{sf} + K_{pf})} \right]$$

$$A_{33} = \left[\frac{K_{pf}}{M_{pf}s^2 + (K_{sf} + K_{pf})} \right]$$

$$A_{34} = \left[\frac{K_{pf}L_f}{M_{pf}s^2 + (K_{sf} + K_{pf})} \right]$$

$$A_{35} = \left[\frac{\alpha}{M_{pf}s^2 + (K_{sf} + K_{pf})} \right]$$

Rear piezoelectric stack:

$$M_{pr}\ddot{Y}_{pr} = -K_{sr}(Y_{pr} - Y_{ur}) + K_{pr}(Y_s + L_r\theta_s - Y_{pr}) + (\alpha)V_{pr} \quad (51)$$

Applying Laplace transformation:

$$\begin{aligned} & \left(M_{pr}s^2 + (K_{sr} + K_{pr}) \right) Y_{pr} \\ & = (K_{sr})Y_{ur} + (K_{pr})Y_s + (K_{pr}L_r)\theta_s + (\alpha)V_{pr} \end{aligned} \quad (52)$$

The vertical displacement of the rear piezoelectric stack can be written as

$$Y_{pr} = A_{36}Y_{ur} + A_{37}Y_s + A_{38}\theta_s + A_{39}V_{pr} \quad (53)$$

where

$$A_{36} = \left[\frac{K_{sr}}{M_{pr}s^2 + (K_{sr} + K_{pr})} \right]$$

$$A_{37} = \left[\frac{K_{pr}}{M_{pr}s^2 + (K_{sr} + K_{pr})} \right]$$

$$A_{38} = \left[\frac{K_{pr}L_r}{M_{pr}s^2 + (K_{sr} + K_{pr})} \right]$$

$$A_{39} = \left[\frac{\alpha}{M_{pf}s^2 + (K_{sf} + K_{pf})} \right]$$

The governing equations for the equivalent electrical system as derived in equation (22) can be modified and written separately in Laplace transformation as:

The front harvested voltage and power:

$$V_f = \alpha R(\dot{Y}_s - L_f \dot{\theta}_s - \dot{Y}_{pf}) - CR \dot{V}_f \quad (54)$$

Applying Laplace transformation:

$$V_f = A_{40}Y_s - A_{41}\theta_s - A_{40}Y_{pf} \quad (55)$$

Chapter 4: Experimental Setup

Figure 38 demonstrates the experimental setup used in this work. The system represents the QCM with a piezoelectric stack attached to the shaker for testing. The other subsystems used in the experiment are the shaker input with signal waveform generator and amplifier, data acquisition system, and electrical circuit.

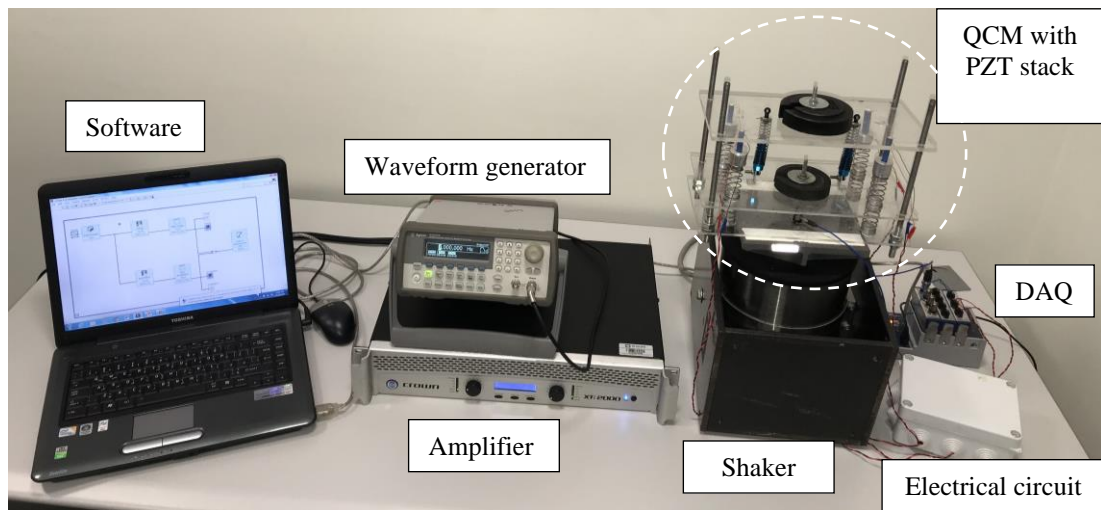


Figure 38: Experimental setup of QCM with piezoelectric stack.

4.1 Quarter car model with piezoelectric stack

QCM shown in Figure 39 consists of three masses, (or three plates) that are made of Poly(methyl methacrylate) (PMMA). The plates from the bottom represent the road input, unsprung mass, and sprung mass with dimensions of 30 cm \times 15 cm. The thickness of the sprung plate is 6 mm, while for the road and unsprung plates it is 4 mm. There are four recesses at the bottom of the sprung plate to set in the piezoelectric stacks. Four bottom springs (e.g., the spring store PC1880) installed between the bottom and middle plates represent the tire stiffness, each with a free length of 41.402 mm, outer diameter of 22.225 mm, and stiffness coefficient of 1550 N/m. However, the four springs (e.g., the spring store PC1575) installed between the

sprung and unsprung masses represent to the suspension springs with a free length of 57.15 mm, outer diameter of 22.6 mm, and stiffness coefficient of 700 N/m. There are two shock absorbers (e.g., Amazon Rc Car 1/10 Shock Absorber Damper pair) that represent the suspension dampers each with a viscous damping coefficient of 25 Ns/m. Tipped masses of 1 kg and 0.6 kg are located at the center of the upper and middle plates that correspond to the sprung and unsprung masses, respectively. Four piezoelectric stacks are installed in series with the suspension springs through aluminum cylinders. The physical, electrical, and electromechanical properties of the piezoelectric stacks are presented in Table 8.

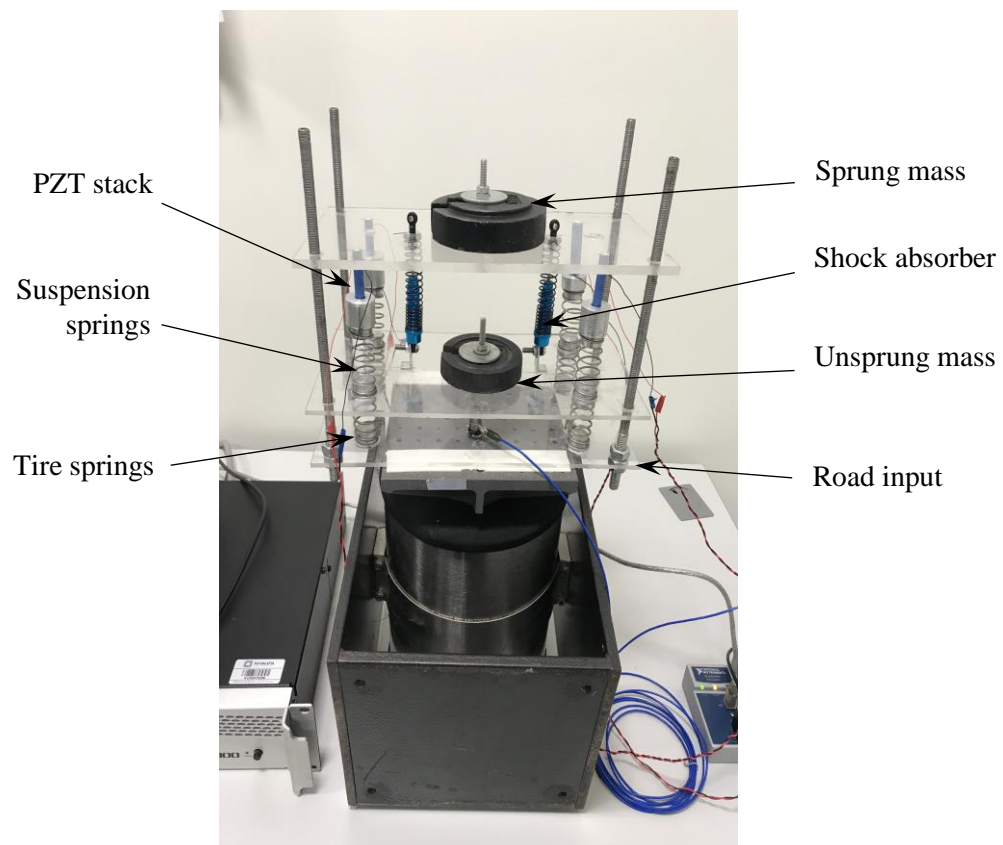


Figure 39: QCM attached to the shaker.

Table 8: Piezoelectric stack material properties.

Property	Symbol	Value	Unit
Length	L	40	mm
Area	A	49	mm ²
Mass	M	15	g
Density	ρ	7.8	g/cm ³
Stiffness	K	51	MN/s
Capacitance	C	4.5	μ F
Piezoelectric constant	d_{33}	600	pm/V
Elastic constant	E_{33}	53	GPa
Dielectric constant	ϵ_{33}	30.975	nF/m
Electromechanical coupling coefficient	k	0.65	NA

4.2 Vibration source input

The quarter car system is driven by a single vibrator system of type VTS 100. The shaker is connected to the power amplifier from Crown XTi2000 and arbitrary waveform generator from Agilent 33220A. The setup shown in Figure 40 is used as a vibration source for the experiment to simulate the harmonic excitation of the road.



Figure 40: Vibration source input.

4.3 Data acquisition system

The road input acceleration is measured using the accelerometer (e.g., PCB Piezotronics 352C33) that is mounted on the road input plate. The accelerometer is then connected to the National Instruments (NI) Data Acquisition system (DAQ) of type NI 9234. Also, the piezoelectric stacks and electrical circuits are connected to the DAQ device of type NI 9225. The acceleration and voltage signals are acquired by utilizing the DAQ assistant installed in LABVIEW software that helps in reading the voltage and acceleration signals from different sensors in both time and frequency domains. The screenshot of the program used in the experiment is shown in Figure 41.

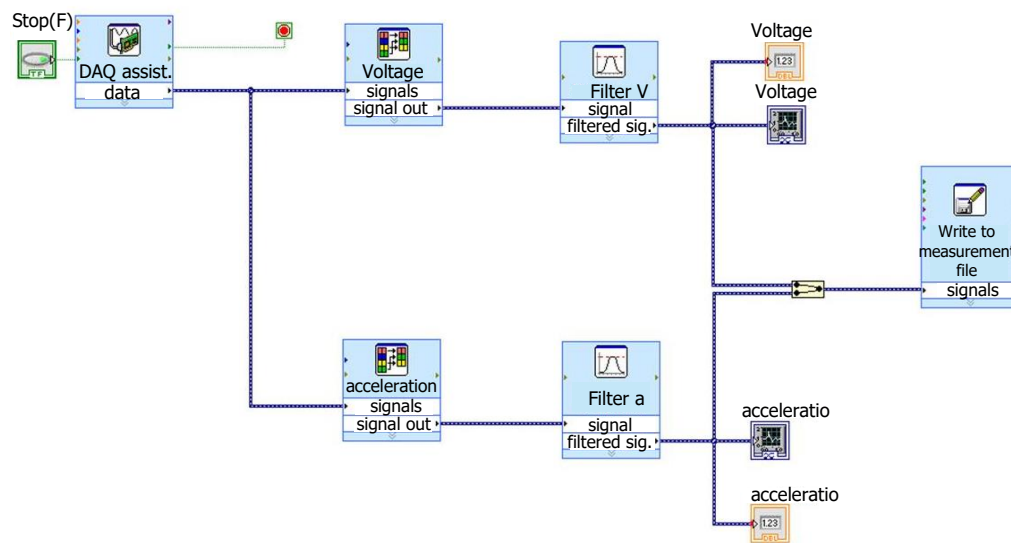


Figure 41: LABVIEW program used in the experiment.

4.4 Electrical circuit

In this experiment, the piezoelectric stack is connected to an amplified circuit PDu100B to amplify the voltage output. This type of circuits allows for different configurations and voltage gain. The connection used in this experiment is a unipolar

input with bipolar output type that will amplify the output voltage up to 55 times. The electrical circuit used is illustrated in Figure 42.

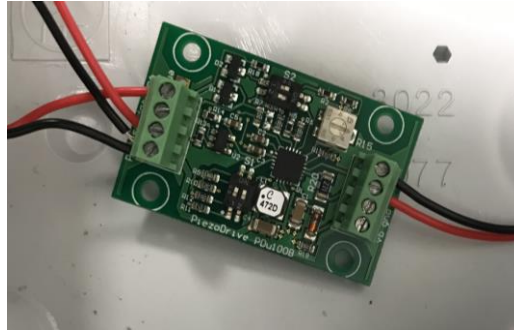


Figure 42: Electrical circuit connection.

Chapter 5: Results and Discussions

5.1 Analytical results

The analytical results from both quarter and half car models were obtained using MATLAB/Simulink under harmonic and random excitations in order to evaluate the harvested voltage and power from piezoelectric stack elements installed in series with the suspension springs. Different CSS as well as the piezoelectric parameters were examined for the HCM.

5.1.1 Quarter vs. half car models

5.1.1.1 Harmonic excitation

To investigate the performance of the QCM and HCM with built in piezoelectric stack, MATLAB/Simulink model shown in Figure 43 was built to carry out the time and frequency domains simulation. The CSS parameters used in both mathematical models are listed in Table 9 [115], [158].

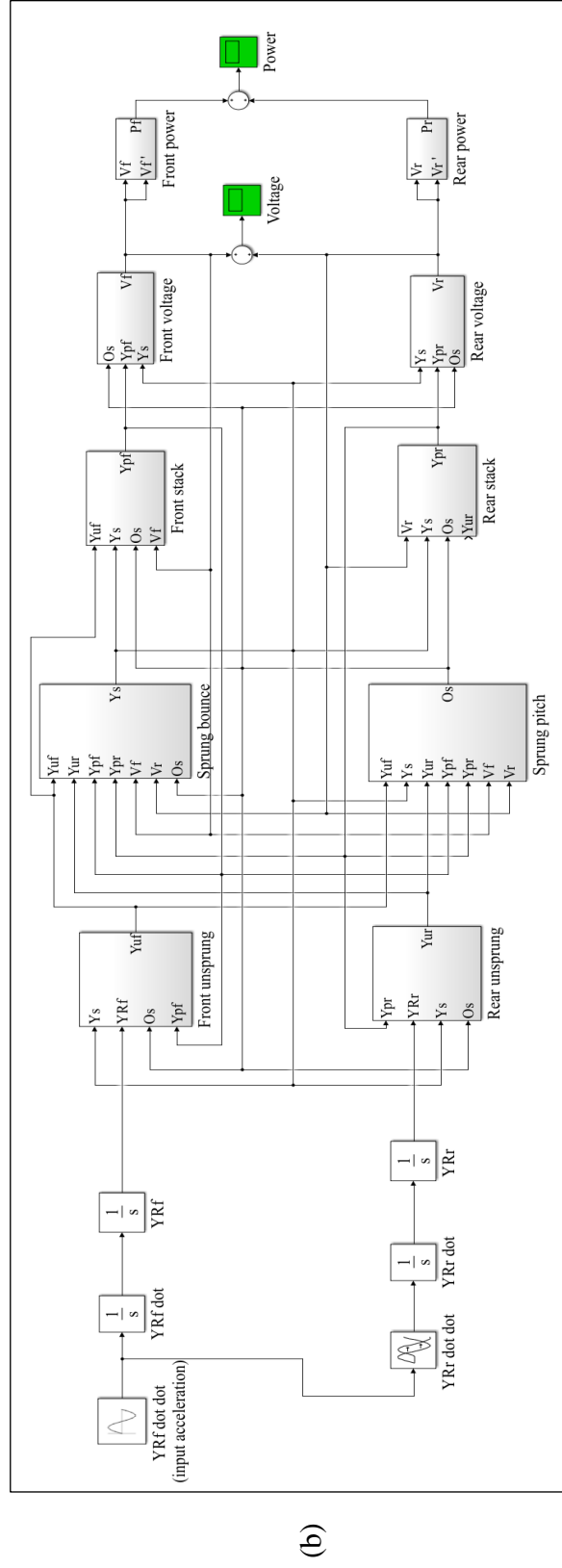
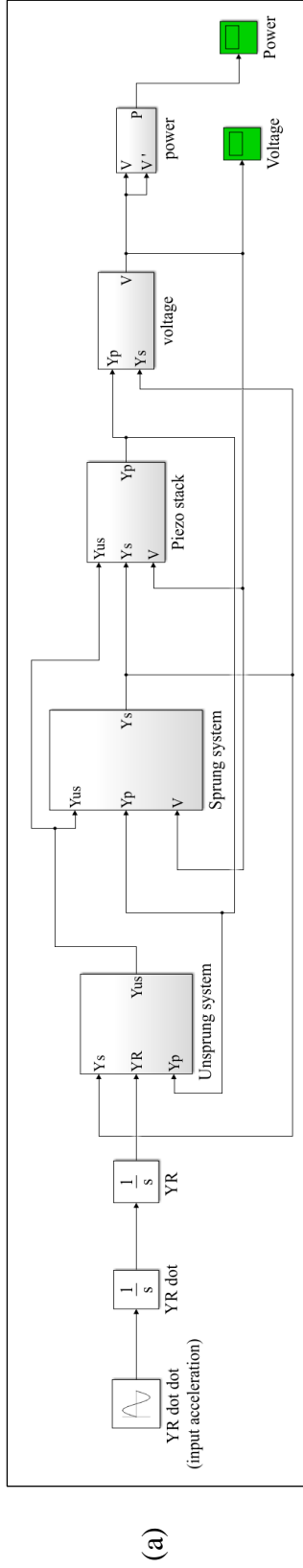


Figure 43: Simulation scheme for the energy harvesting models. (a) QCM. (b) HCM.

Table 9: Parameters used in the mathematical model of the quarter and half car suspension systems [115], [158].

Model	Property	Symbol	Value	Unit
QCM	Sprung mass	M_s	260	kg
	Unsprung mass	M_{us}	40	kg
	Suspension spring stiffness	K_s	26,000	N/m
	Tire stiffness	K_{us}	130,000	N/m
	Suspension damping coefficient	b_s	520	N.s/m
	Tire damping coefficient	b_{us}	265.73	N.s/m
HCM	Sprung mass	M_s	520	kg
	Moment of inertia	I_s	2,000	kg.m ²
	Front/rear unsprung masses	M_{uf}, M_{ur}	40	kg
	Front/rear suspension stiffness	K_{sf}, K_{sr}	26,000	N/m
	Front/rear tire stiffness	K_{uf}, K_{ur}	130,000	N/m
	Front/rear suspension damping	b_{sf}, b_{sr}	520	N.s/m
	Front/rear tire damping	b_{uf}, b_{ur}	265.73	N.s/m
	Distance from C.G. to the front axle	L_f	1.23	m
	Distance from C.G. to the rear axle	L_r	1.65	m

For harmonic excitation of any dynamic model, it is essential to calculate the natural frequencies of the system to determine the locations of the resonance. Studying the relation between the displacement amplitude of each system with the input road displacement amplitude in frequency domain helps in finding the resonant frequencies of the system. Since the QCM is two degrees of freedom (2 DOF), this means that it has two resonant frequencies (1.46 Hz and 9.68 Hz) that can be found from the peak values shown in Figure 44. However, four resonant frequencies for HCM are illustrated in Figure 45. The four peaks correspond to the pitch (1.06 Hz) and bounce motions (1.46 Hz) of the sprung mass and the other bounce motion of the front and rear unsprung masses (9.68 Hz).

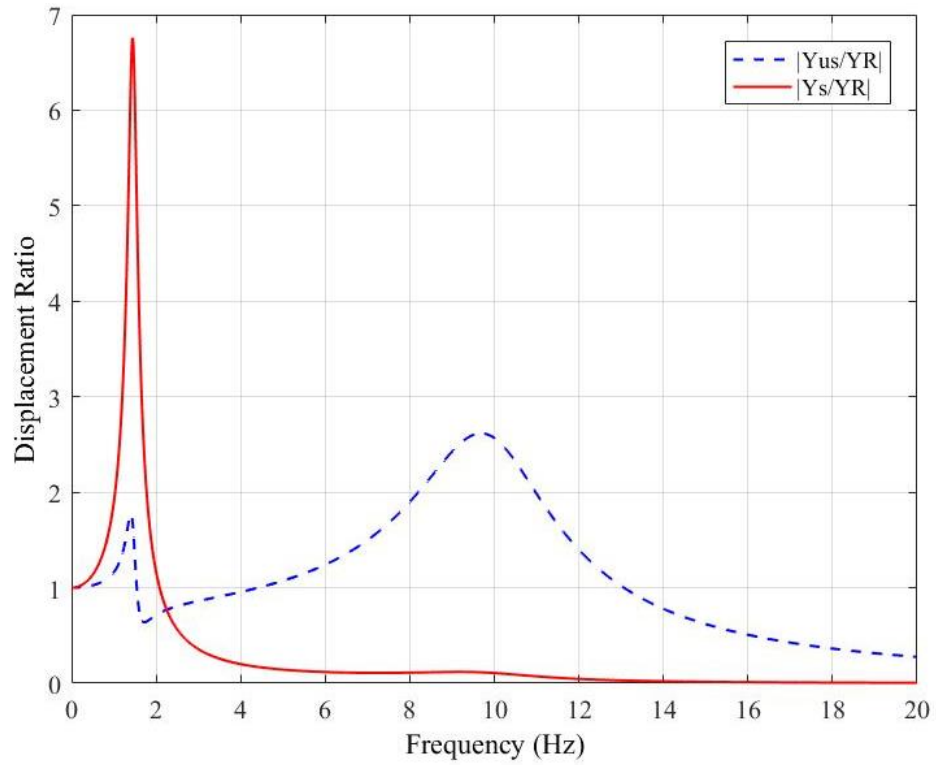


Figure 44: Displacement ratio of sprung and unsprung masses with respect to the input displacement in frequency domain for QCM.

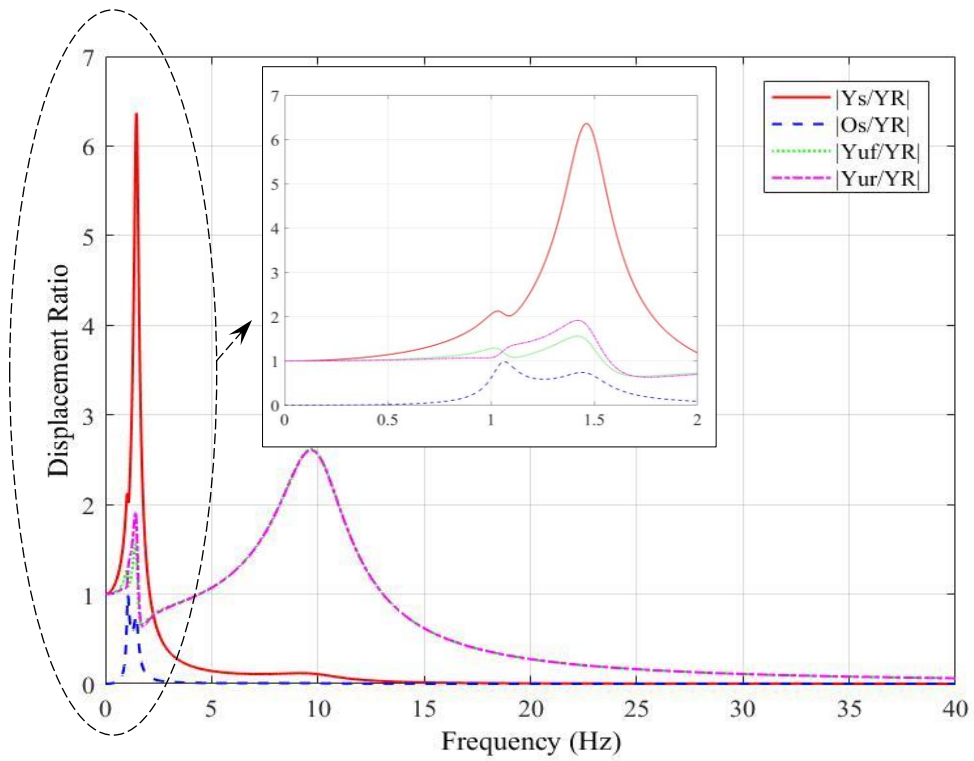


Figure 45: Displacement ratio of sprung and unsprung masses with respect to the input displacement in frequency domain for HCM.

In this work, the piezoelectric stack of type PZT-5H was used since it is the best choice for energy harvesting applications due to the high value of piezoelectric constant d_{33} , availability, and low cost [159]. The piezoelectric stacks were mounted in series with the suspension's springs in QCM and HCM. Their mounting in this way will not affect the dynamic performance/response of the suspension system. The recommended natural frequency of the sprung mass is below 1.5 Hz [160]. A value of more than 1.5 Hz is not expected since it increases the acceleration of the car body and causes discomfort to the passengers. Also, the natural frequency of the pitch mode should be close to the bounce mode of the sprung mass and should not be affected during the pitch motion. Moreover, the unsprung masses natural frequencies should not be less than 8 Hz since the human body is more sensitive to the vertical vibration motion in the frequency range of 4 - 8 Hz [160]. The natural frequencies of the both energy harvesting systems presented in Table 10 matched the ranges that were recommended by Hossain and Chowdhury [160].

Table 10: Natural frequencies of QCM and HCM.

	Natural frequency (f)	Value	Unit
QCM	Sprung bounce motion	1.46	Hz
	Unsprung bounce motion	9.68	Hz
HCM	Sprung pitch motion	1.06	Hz
	Sprung bounce motion	1.46	Hz
	Front unsprung bounce motion	9.68	Hz
	Rear unsprung bounce motion	9.68	Hz

For harmonic input excitation, the power that is available for harvesting is the amount of the power dissipated by the suspension dampers. Thus, the average potential power that can be harvested from the suspension dampers in one oscillation is the

product of the damping force and its relative velocity that can be calculated for QCM and HCM as [161]:

$$P_{avg_{quarter}} = \frac{b_s \omega^2 (Y_s - Y_{us})^2}{2} \quad (60)$$

$$P_{avg_{half}} = \frac{b_{sf} \omega^2 (Y_s - L_f \theta - Y_{uf})^2}{2} + \frac{b_{sr} \omega^2 (Y_s + L_r \theta - Y_{ur})^2}{2} \quad (61)$$

where $(Y_s - Y_{us})$, $(Y_s - L_f \theta - Y_{uf})$, and $(Y_s + L_r \theta - Y_{ur})$ are the amplitude of the relative displacements of the suspension. The average power dissipated by the suspension damper for QCM is depicted in Figure 46. The peak values of power dissipated from the suspension damper were occurred (as expected) at the resonant frequencies of the system. At the sprung resonant frequency (1.46 Hz), the dissipated power from the suspension damper was 1424 W, while it is remarkably increased to 15.54 kW at the unsprung resonant frequency (9.68 Hz).

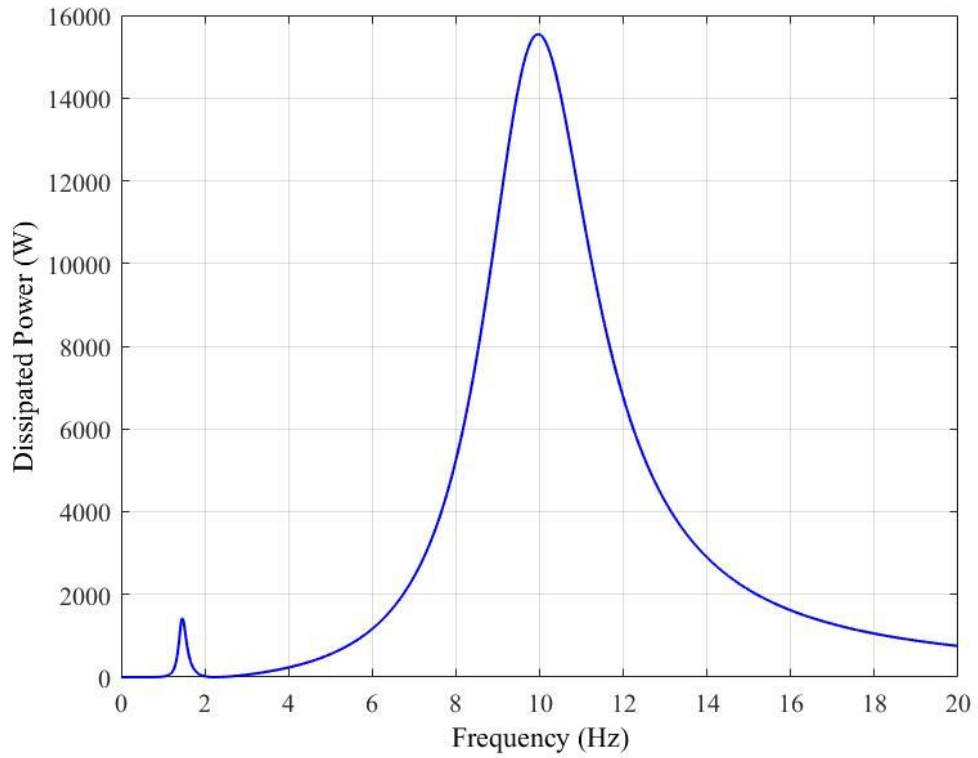


Figure 46: The variation of the average dissipated power by the suspension damper for QCM in the frequency domain.

For HCM, the average peak values of the dissipated power are recorded four times as presented in Figure 47. The lowest peak corresponded to the sprung pitch mode with a value of 187 W. At the sprung bounce mode, the average dissipated power increased to 2990 W. Whereas, at the unsprung bounce mode for the front and rear masses, the dampers dissipated the highest amount of power (31.131 kW).

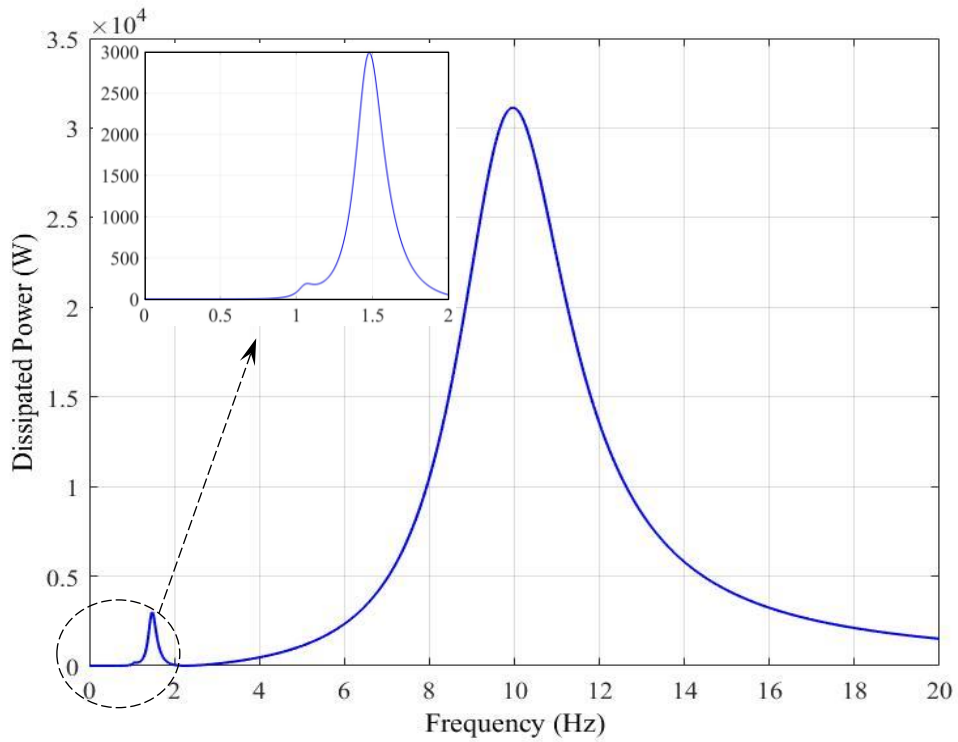


Figure 47: The variation of the average dissipated power by the suspension damper for HCM in the frequency domain.

According to the ISO 13473-1 [162], the road texture was divided into four main categories depending on the value of the texture wavelength λ , i- microtexture: $\lambda < 0.5$ mm, ii- macrotexture: $0.5 \text{ mm} < \lambda < 50 \text{ mm}$, iii- megatexture: $50 \text{ mm} < \lambda < 0.5$ m and iv- unevenness: $0.5 \text{ m} < \lambda < 50 \text{ m}$. The common unevenness texture wavelength used in the literature was 5 m [163]. The car traveling velocity u over a road is affected by the excitation frequency f and the road wavelength λ as shown in the following equation:

$$u = \lambda f \quad (62)$$

Since most of the cars' rigid body excitation frequency within the range [0.5 - 15 Hz], so that the corresponding car velocity is varied between 9 km/h and 270 km/h [164]. The results from Figure 48 and Figure 49 show the average dissipated power for QCM and HCM at different velocity ranges. For the QCM, the two highest dissipated power were occurred at the velocities of 26.28 km/h and 174.24 km/h. On the other hand, the first dissipated power for the HCM was recorded when the car was traveled at a velocity of 19 km/h. The second corresponding peak that revealed to the sprung bouncing mode had a power dissipation of 2990 W. However, the average power increased significantly to 31 kW at the front and rear unsprung resonant frequency of 9.68 Hz with a velocity of 174.24 km/h.

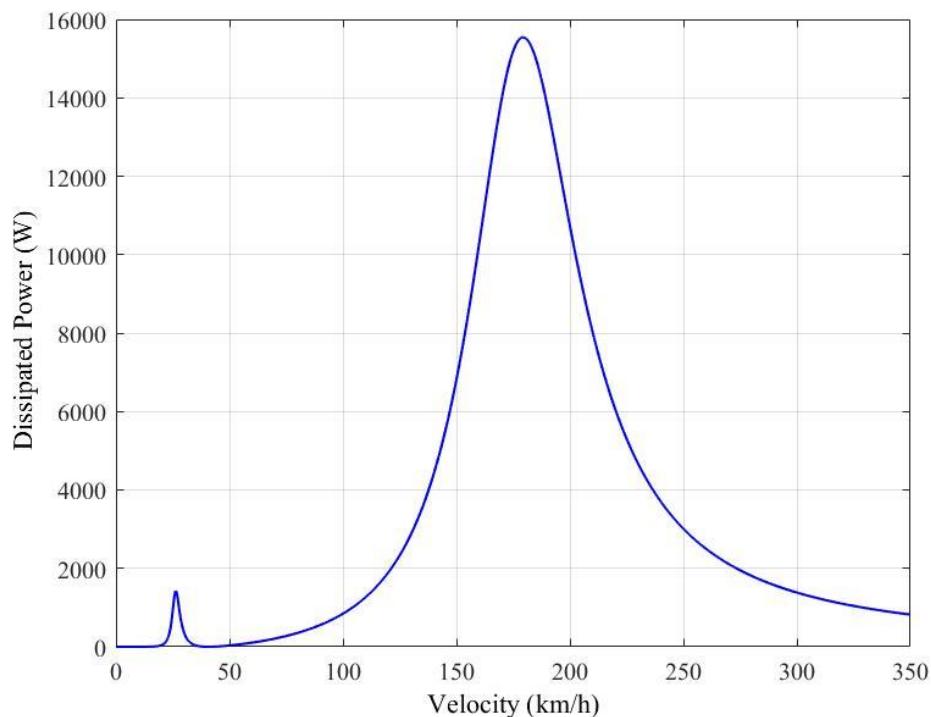


Figure 48: The variation of the average dissipated power by the suspension damper for QCM in different car velocities.

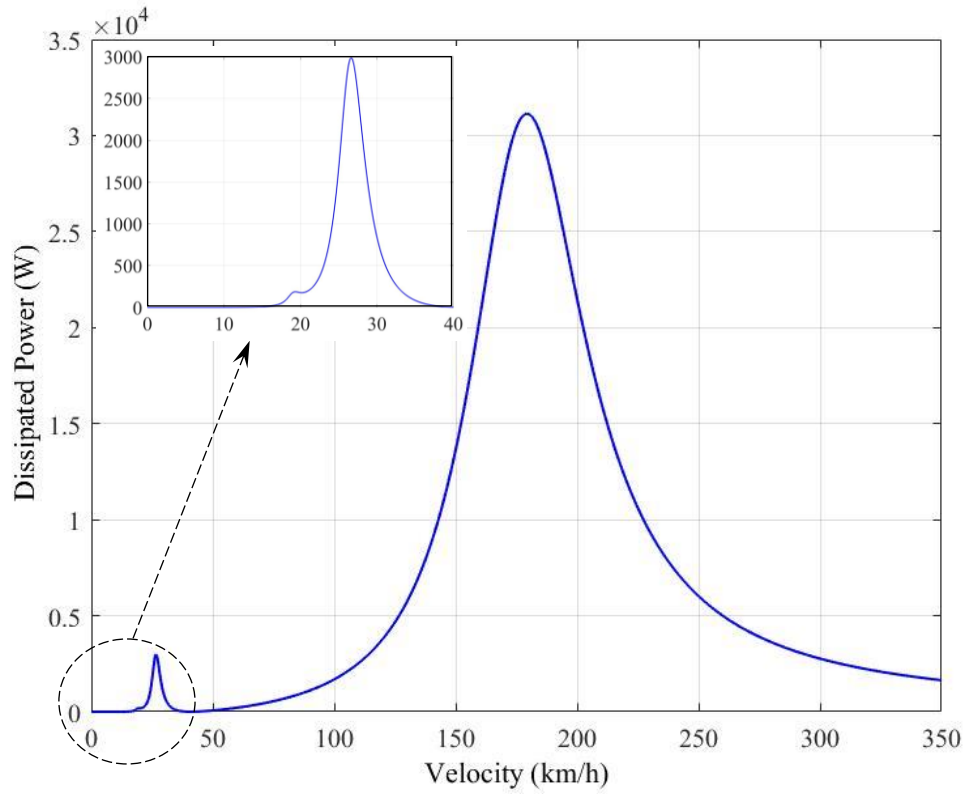


Figure 49: The variation of the average dissipated power by the suspension damper for HCM in different car velocities.

Inserting the piezoelectric stack that was made of 40 layers and with a surface area and length of 49 mm^2 and 40 mm , respectively, was utilized in harvesting the dissipated power from the suspension systems. The steady-state responses for evaluating the harvested voltage and power were simulated by exciting the car using sinusoidal acceleration excitation input with an amplitude of 0.5 g ($4.9 \text{ m/s}^2 \sim$ amplitude displacement of 0.05 m [129], [165]) and velocity of 9.17 rad/s . It can be observed from both QCM and HCM shown in Figure 50 and Figure 51 that, at the beginning time of simulation, there are a transient response to the excitation acceleration. The transient phase ends within very short period (\sim milliseconds) and after this stage the maximum output voltage and power can be measured. At the steady state phase, the maximum generated voltage and power for the QCM were found to be

around 19.11 V and 36.74 mW, respectively. The root mean square (RMS) was then calculated for the harmonic acceleration excitation through dividing the peak values by the square root of 2. Consequently, the RMS voltage and power values were found to be 13.51 V and 18.26 mW, respectively.

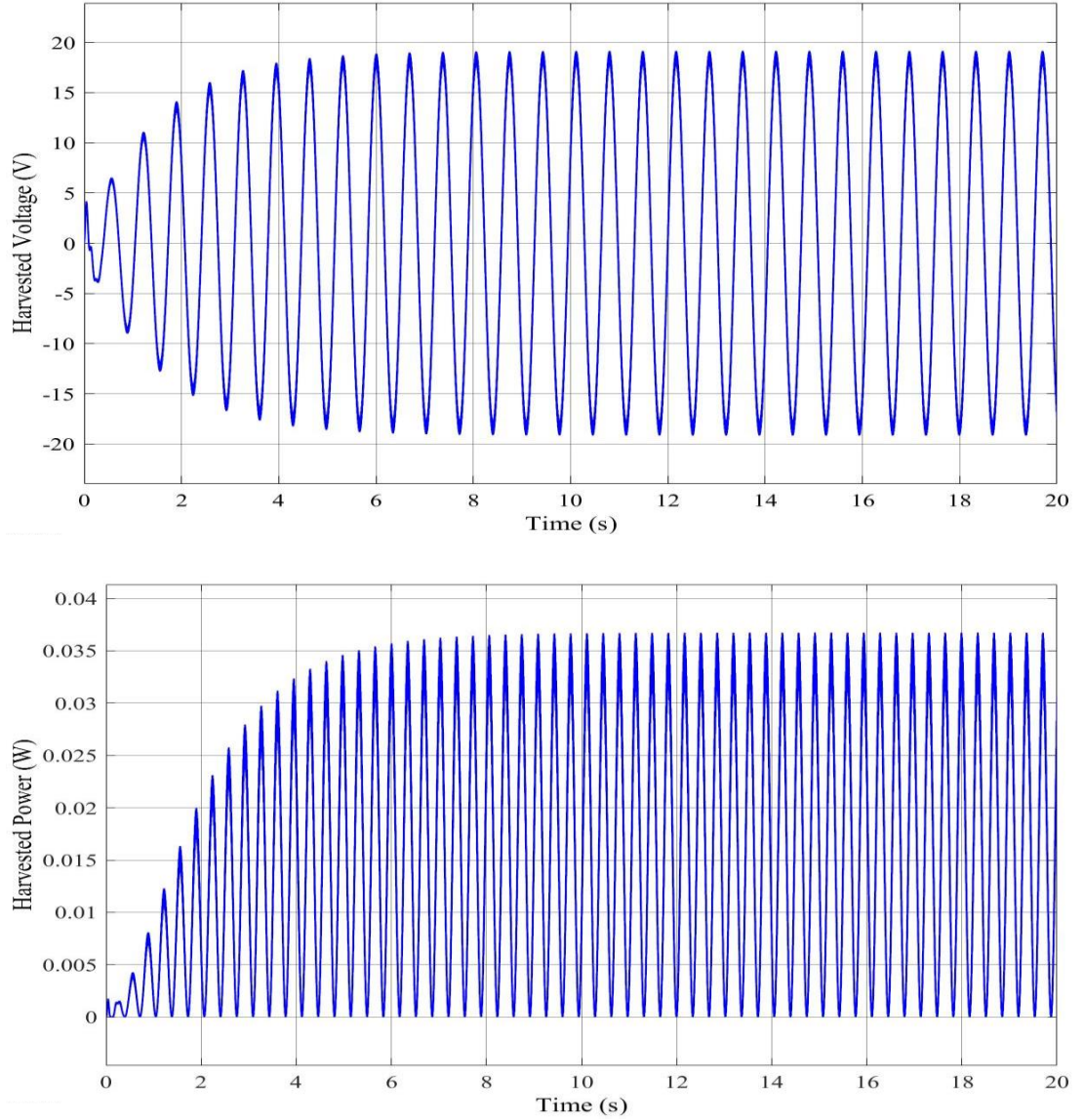


Figure 50: Harvested voltage and power in the time domain for QCM.

Two piezoelectric stacks were installed in series with the front and rear suspension springs in HCM. At the steady state phase (see Figure 51), the maximum harvested voltage and power were 33.56 V and 56.35 mW, respectively. The

corresponding RMS values were calculated and found to be 23.73 V and 28.13 mW for the harvested voltage and power, respectively. By comparing the generated outcomes from 4 DOF and 2 DOF models, the results clearly showed that the output voltage and power of HCM are increased by 75.6% and 53.38%, respectively.

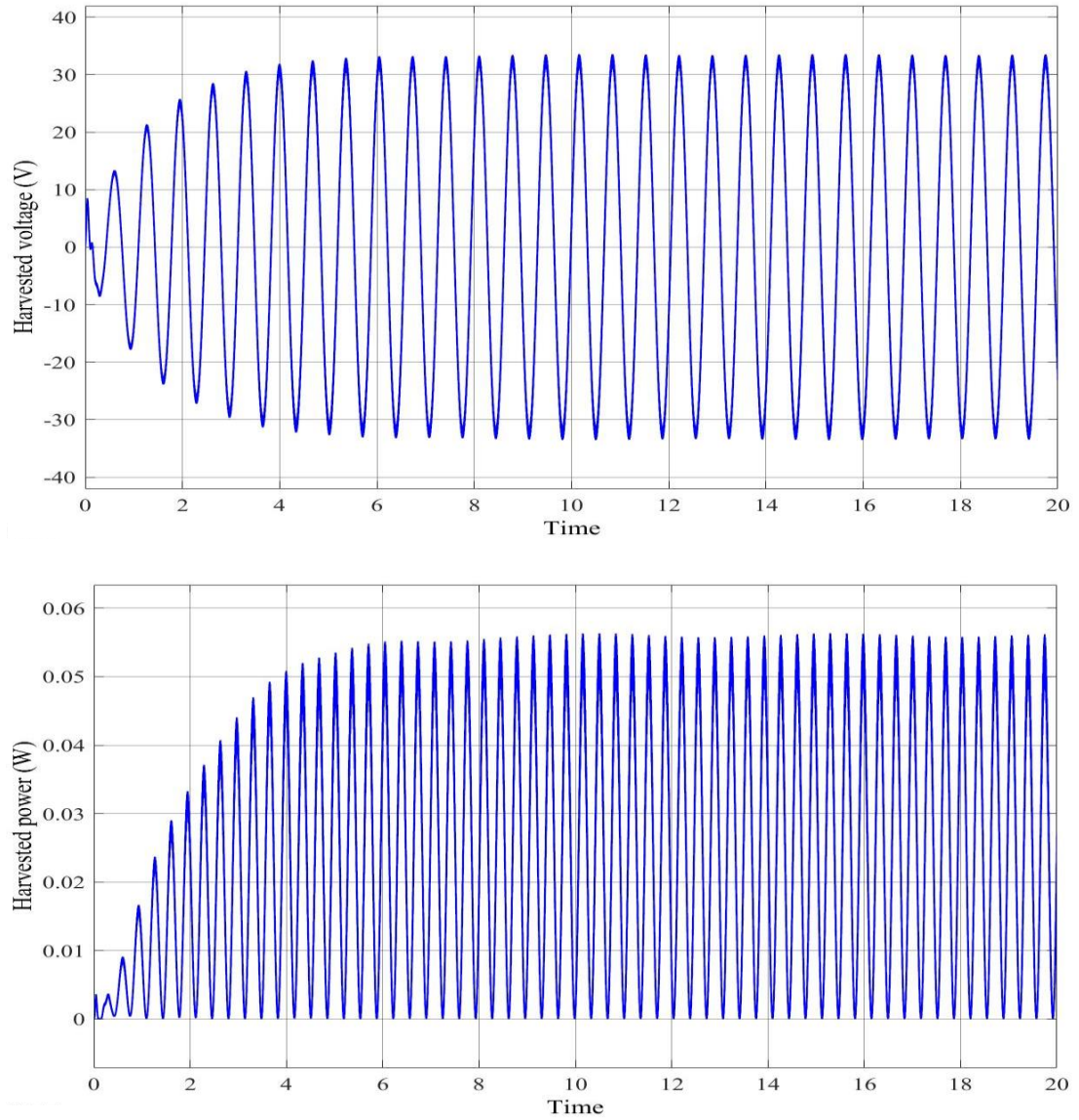


Figure 51: Harvested voltage and power in the time domain for HCM.

The output harvested voltage and power were also studied in the frequency domain for QCM and HCM and the results are presented in Figure 52 and Figure 53. The input excitation frequency was varied from 0 to 20 Hz, and the other car's

parameters (e.g. mass, stiffness coefficient, and damping coefficient) were kept fixed. The plots were conducted for each excitation frequency by taking the peak values of the harvested voltage and power at the steady state phase. The results showed that the highest value of the harvested voltage and power for both cases were occurred at 1.46 Hz which matched with the sprung bouncing mode. However, for the HCM, the second peak was recorded at the sprung pitch mode of 1.06 Hz with the output voltage and power of 17.82 V and 31.74 mW, respectively. For the QCM and HCM, the lowest peak values were found at the bouncing mode of the unsprung masses ($f = 9.68$ Hz). For the QCM, the harvested voltage and power were 1.427 V and 0.204 mW, respectively, in the other side, for the half car, the peaks were 2.815 V and 0.396 mW. Thus, it can be concluded, as expected, that the resonant frequencies, generate more harvested energy if compared with that of the non-resonant frequencies.

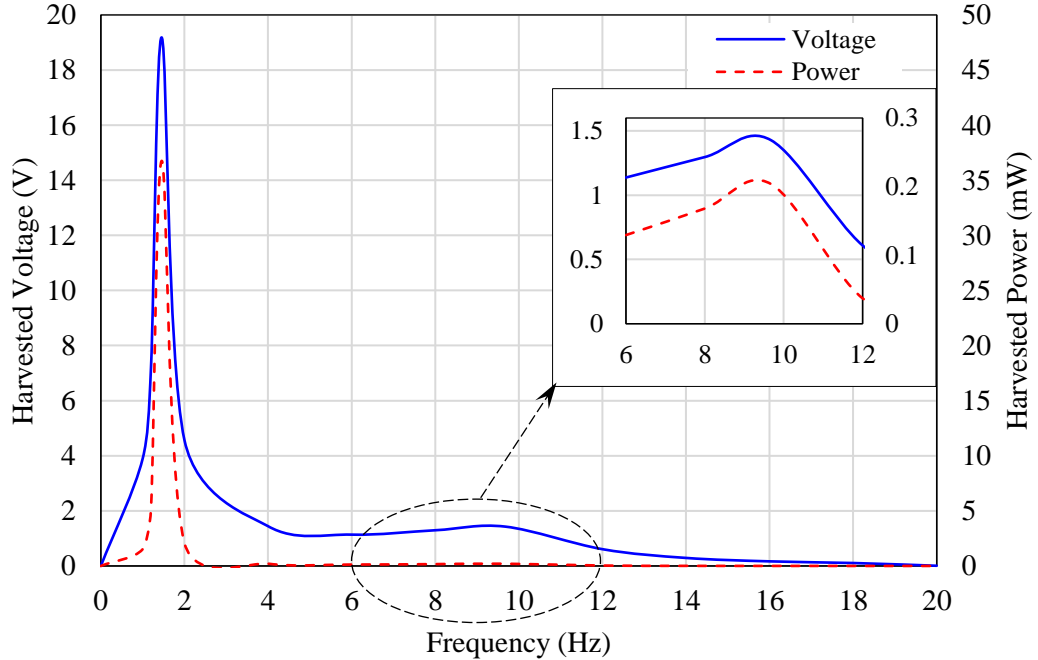


Figure 52: Harvested voltage and power in the frequency domain for QCM.

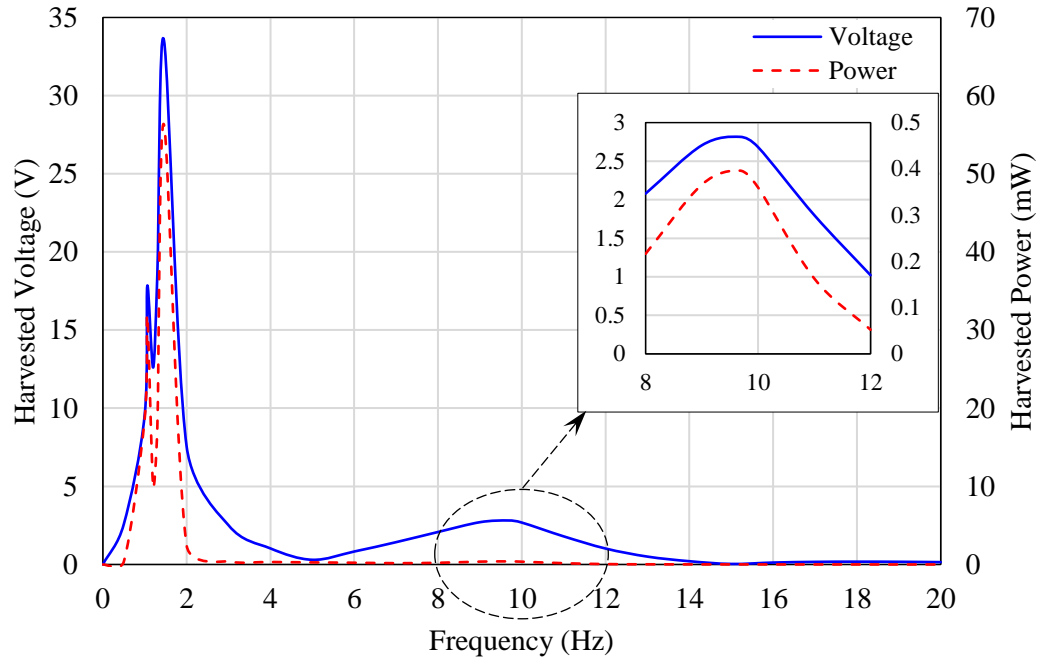


Figure 53: Harvested voltage and power in the frequency domain for HCM.

The harvested voltage and power at different car velocities are also demonstrated in Figure 54 for QCM and Figure 55 for HCM. It can be pointed out that, the trend of variation of the harvested voltage and power vs. frequency (Figure 52 and Figure 53) is similar to that of the harvested voltage and power vs. car velocity (Figure 54 and Figure 55). The reason behind this similarity is that, the frequency and velocity are directly proportional to each other. This correlation is illustrated in equation (62) at a road wavelength λ of 5 m. The maximum values take place at the velocities corresponding to the resonant frequencies. Accordingly, the most significant output voltage and power occur at velocity of 26.28 km/h that corresponded to the sprung bounce resonant frequency of 1.46 Hz. While for the half model at the sprung pitch resonant frequency of 1.06 Hz, the corresponding car velocity was found to be 19.1 km/h that could provide harvested voltage and power of 17.82 V and 31.74 mW, respectively. The lowest peaks of the harvested voltage and power for both models were related to the unsprung resonant frequency at car velocity of 174.24 km/h.

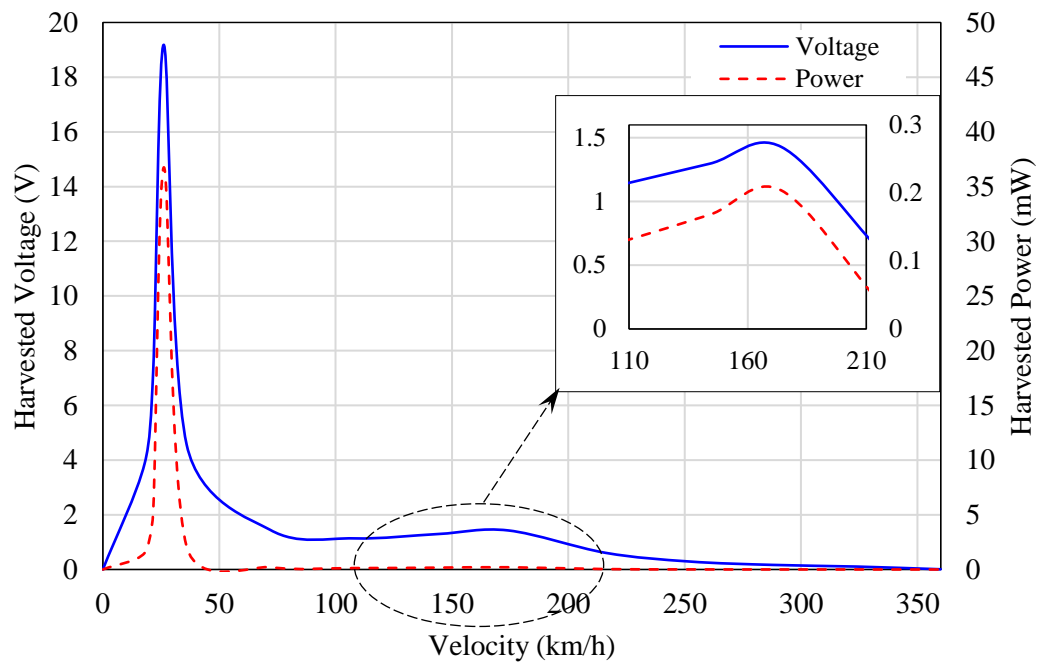


Figure 54: Harvested voltage and power at different car velocities for QCM.

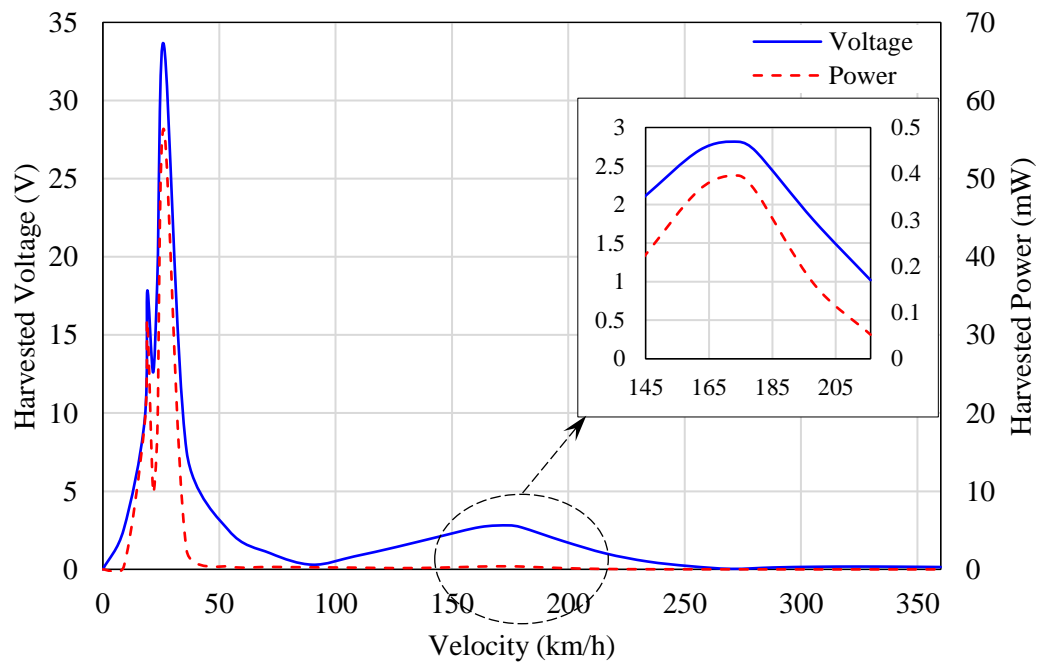


Figure 55: Harvested voltage and power at different car velocities for HCM.

Taking the most common velocity ranges where the cars usually run [40 – 100 km/h], the harvested voltage and power was calculated for both models as presented in Figure 56 and Figure 57. This velocity range corresponds to the non-resonance

frequencies. It can be noticed that, the harvested voltage and power decrease with velocity. For QCM, the reduction in the harvested voltage and power were from 3.5 V to 1.16 V and 1.2 mW to 0.13 mW, respectively. However, for the HCM, the harvested voltage was decreased from 5.5 V to 0.5 V and the harvested power was decreased from 1.5 mW to 0.24 mW. Also, the harvested voltage and power at 40 km/h were more than the power harvested at the unsprung bounce resonant frequency (174.24 km/h). This illustrates that yet the system can harvest power out of the resonant frequencies and within the most suitable velocity range at which the cars move.

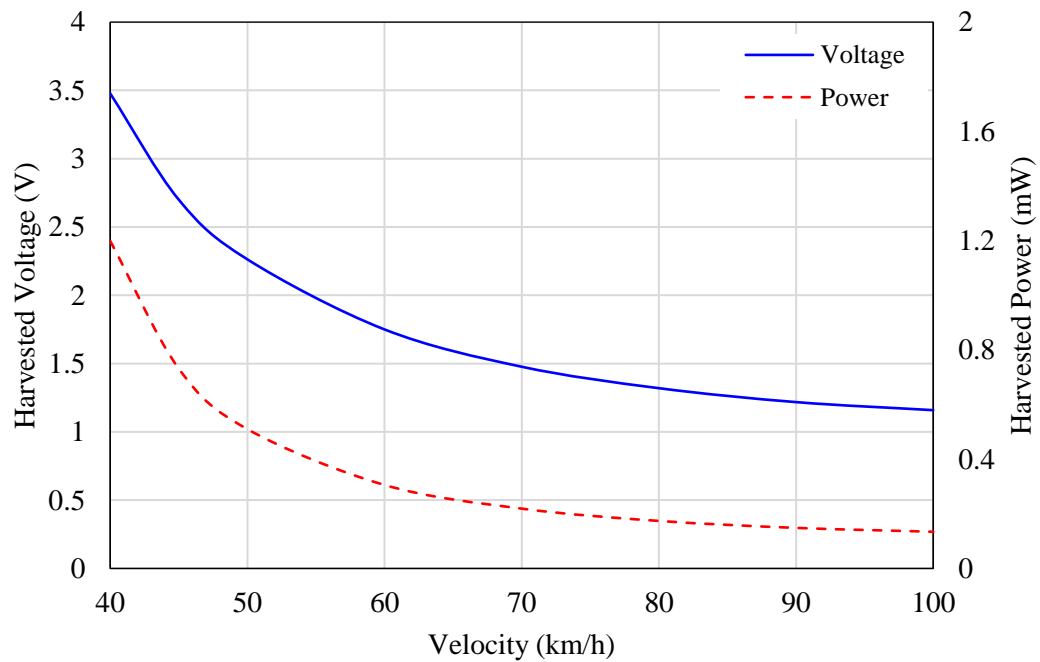


Figure 56: Harvested voltage and power in different car velocities at the non-resonance frequency for QCM.

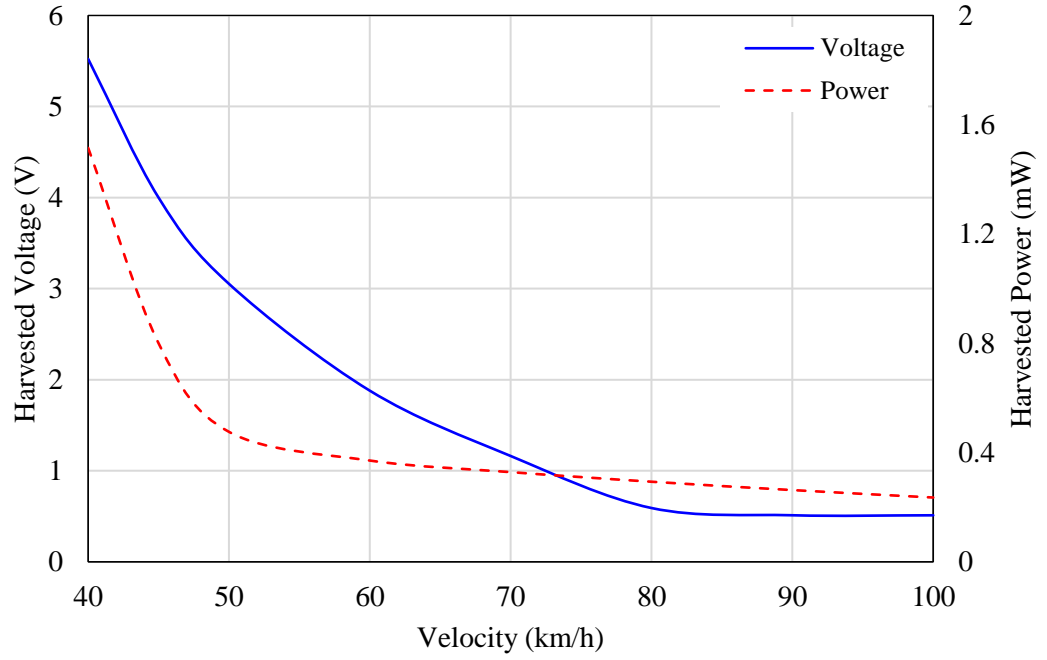


Figure 57: Harvested voltage and power in different car velocities at the non-resonance frequency for HCM.

5.1.1.2 Random excitation

When a car moves at a constant speed, the road roughness is considered as a stationary random process that is subjected to Gauss distribution. Random road profile can be expressed in the space domain in terms of power spectral density PSD using the equation [166]:

$$G_q(n) = G_q(n_o) \left(\frac{n}{n_o} \right)^{-W} \quad (63)$$

where n is spatial frequency and n_o is spatial reference frequency ($n_o=0.1 \text{ m}^{-1}$), $G_q(n_o)$ denotes road roughness coefficient (m^2/m^{-1}), and W is called the waviness that represents the road wavelength to be either long or short. Usually, the waviness was taken to be $W = 2$, which is within the range of $1.75 \leq W \leq 2.25$ [167].

The spatial frequency $G_q(n)$ is transferred to the time frequency $G_q(f)$ from the relation of the time frequency f (s^{-1}), spatial frequency n (m^{-1}), and car speed u (m/s) as presented by equations (64) through (66):

$$f = u \times n \quad (64)$$

The mathematical relation of $G_q(n)$ and $G_q(f)$ can be presented as:

$$G_q(f) = \frac{1}{u} G_q(n) \quad (65)$$

When $W = 2$, equation (65) can be rewritten as:

$$G_q(f) = \frac{1}{u} G_q(n_o) \left(\frac{n}{n_o} \right)^{-2} = G_q(n_o) n_o^2 \frac{u}{f^2} \quad (66)$$

By deriving equation (66), the car vertical speed PSD can be expressed as:

$$G_{\dot{q}}(f) = (2\pi f)^2 G_q(f) = 4\pi^2 G_q(n_o) n_o^2 u \quad (67)$$

For a stationary random process, the road roughness in the time domain is represented by filtering white noise generation method. Random road input of the front tire is expressed as following [117]:

$$\dot{Y}_{Rf}(t) = 2\pi n_o w(t) \cdot \sqrt{G_q(n_o) u(t)} - 2\pi f_o Y_{Rf}(t) \quad (68)$$

where $w(t)$ is Gaussian white noise with mean zero and f_o represents the cut-off frequency. Assuming the delay effect at the rear tire, the random road input can be expressed as $\dot{Y}_{Rr}(t) = \dot{Y}_{Rf}(t - \tau)$. Consequently, the random road input of the rear tire is derived as [168]:

$$\dot{Y}_{Rr}(t) = -\dot{Y}_{Rf} + \frac{2uY_{Rf}(t)}{L} - \frac{2uY_{Rr}(t)}{L} \quad (69)$$

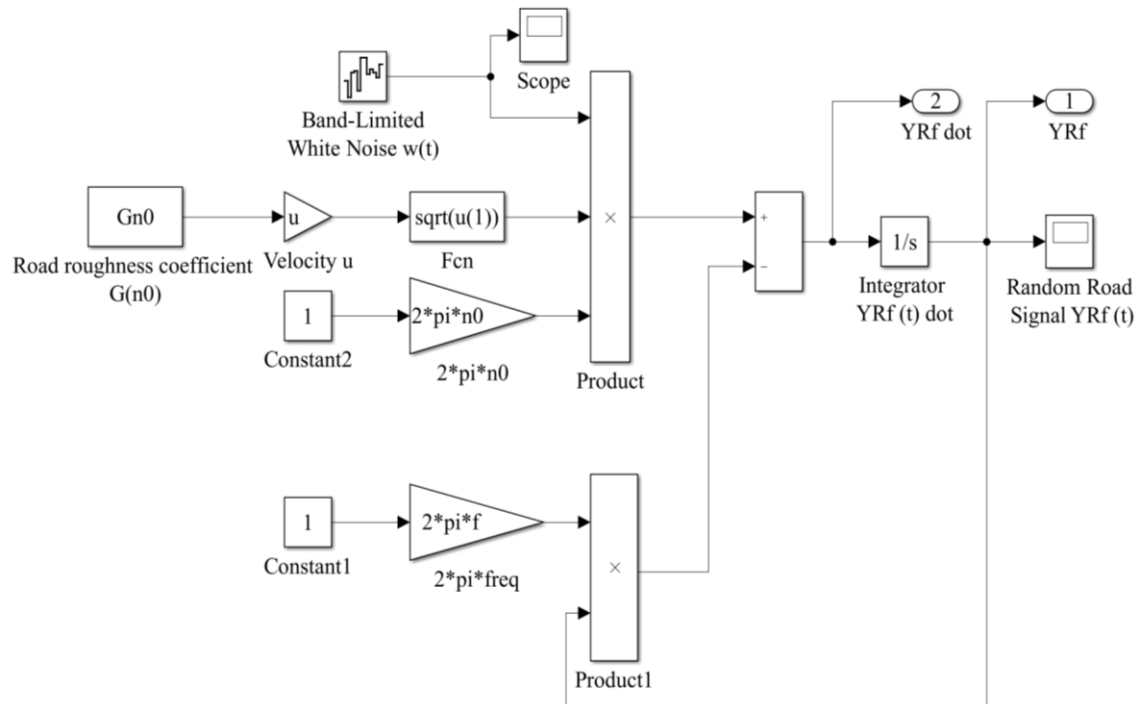
The car excitation input was tested by different road roughness profiles that were classified by ISO 8608 international standard [166] and illustrated in Table 11. The road roughness has several grades of road profile, starting from the very smooth road that is presented as class A to the very rough road of class H (see Table 11).

Table 11: Road roughness level according to ISO 8608 [166].

Road Profile Grade	$G_q(n_o)(\times 10^{-6}m^3)$ $n_o = 0.1 m^{-1}$ Geometric Mean
Class A	16
Class B	64
Class C	256
Class D	1024
Class E	4096
Class F	16384
Class G	65536
Class H	262144

Setting $f_o = 0$ and assuming the car was traveled at a constant speed of 80 km/h, the harvested power from the QCM and HCM subjected to the different grade roughness of road profile was investigated at three main classes: A, C, and H. The simulation scheme for front and rear road roughness inputs with their signals for the three classes are demonstrated in Figure 58 and Figure 59.

(a)



(b)

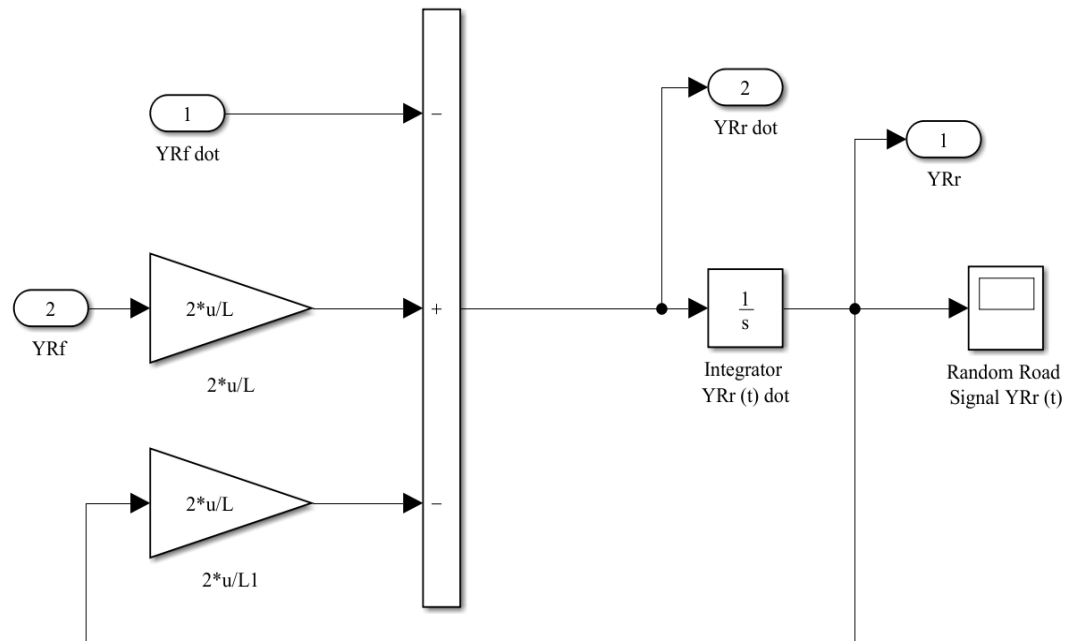


Figure 58: Simulation scheme for road roughness input. (a) Front tire. (b) Rear tire.

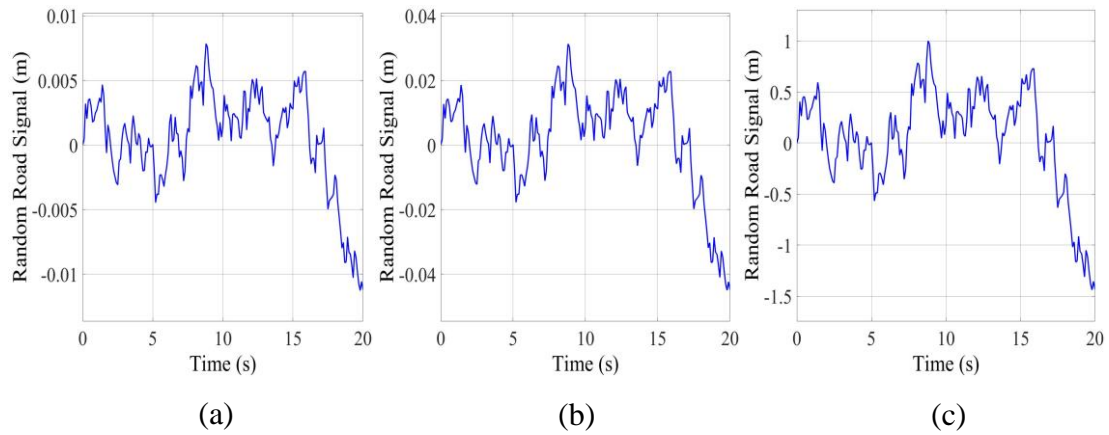
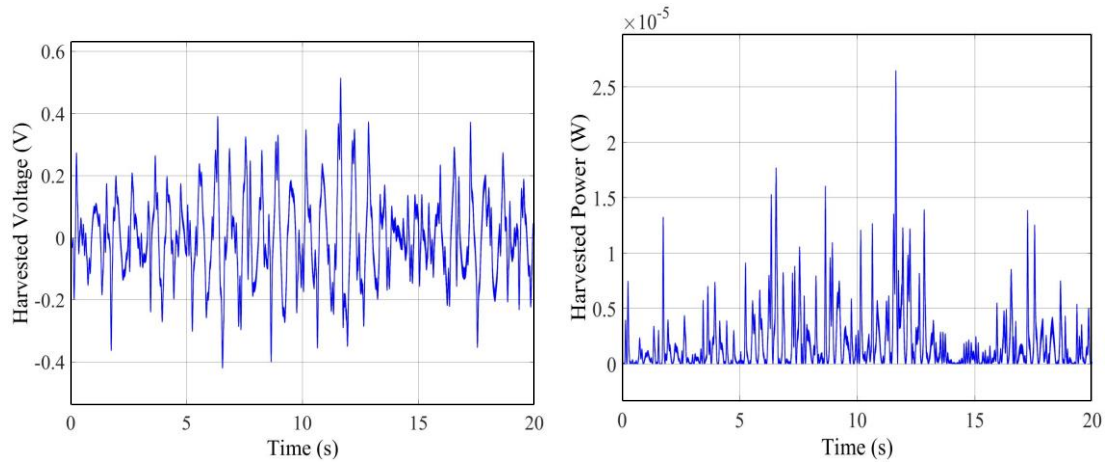


Figure 59: Road roughness signals. (a) Class A. (b) Class C. (c) Class H.

The results for different road classes revealed that, the best road quality were presented by class A as shown in Figure 59 (a) and **Error! Reference source not found.** which means it has a minor degree of roughness. As a result, the power that can be harvested from the QCM and HCM was minimal due to the less vibrations occurred to the suspension system. For QCM, the peak value was recorded as 0.0265 mW with RMS value of 0.00318 mW, while for HCM the peak value was 0.0328 mW with RMS value of 0.00489 mW. For class C, which is considered as an average road quality, the results were increased when compared to class A. As shown in **Error! Reference source not found.**, for QCM, the maximum harvested voltage and power were 2.06 V and 0.4242 mW, respectively. The output voltage and power were increased approximately by 60% when calculated for a HCM. On the other hand, the most significant voltage and power harvested from the road roughness were captured from class H as illustrated in **Error! Reference source not found.** which has the highest degree of roughness. The harvesting power from the very rough road was 434.3 mW with RMS value of 52.1 mW for QCM and it was 537.5 mW with RMS value of 80.1 mW for HCM.

Quarter car model (QCM):



Half car model (HCM):

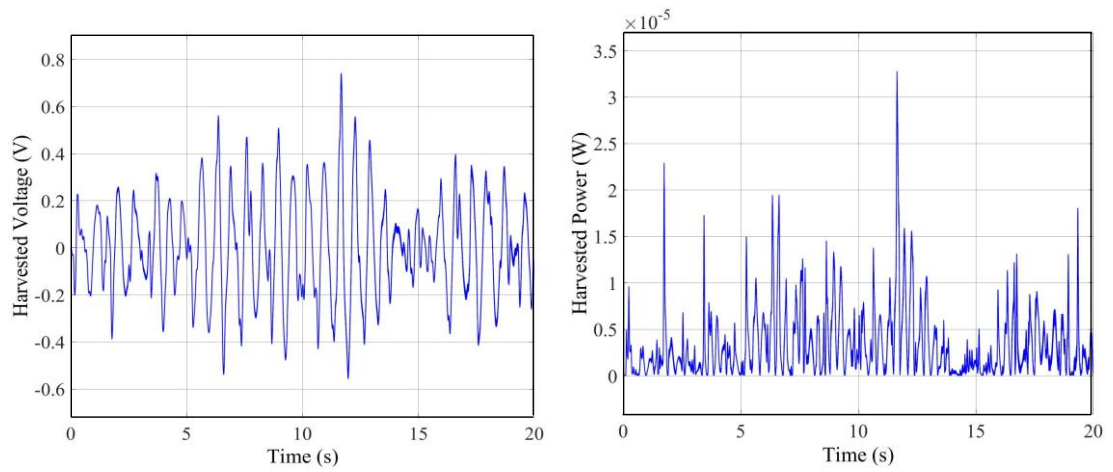
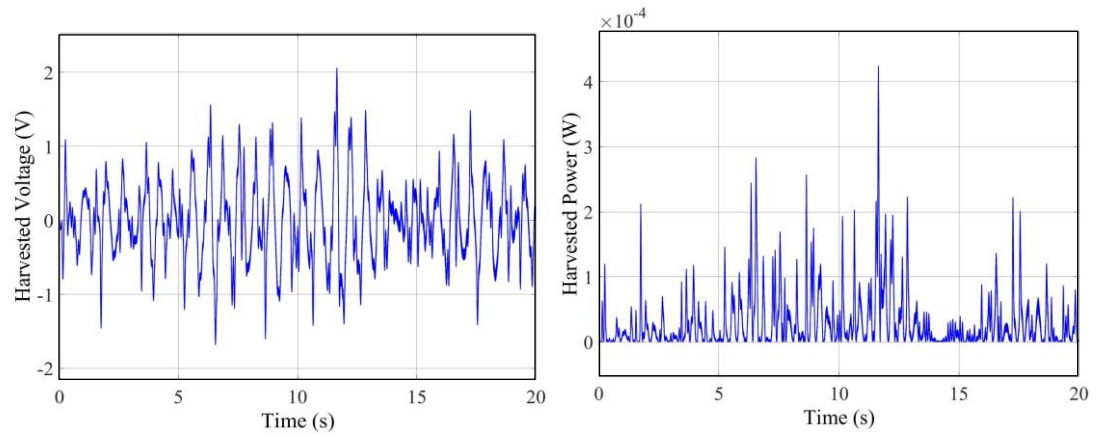


Figure 60: Harvested voltage and power on a road of class A for both QCM and HCM.

Quarter car model (QCM):



Half car model (HCM):

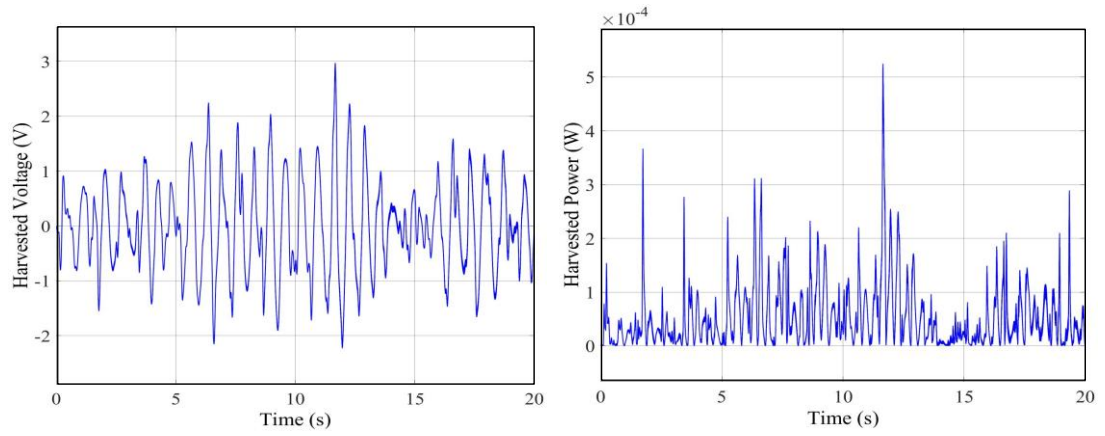
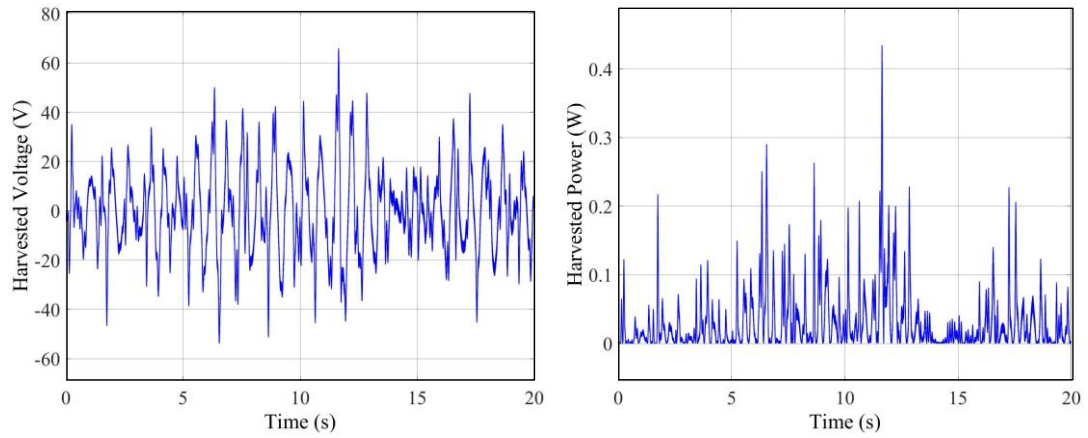


Figure 61: Harvested voltage and power on a road of class C for both QCM and HCM.

Quarter car model (QCM):



Half car model (HCM):

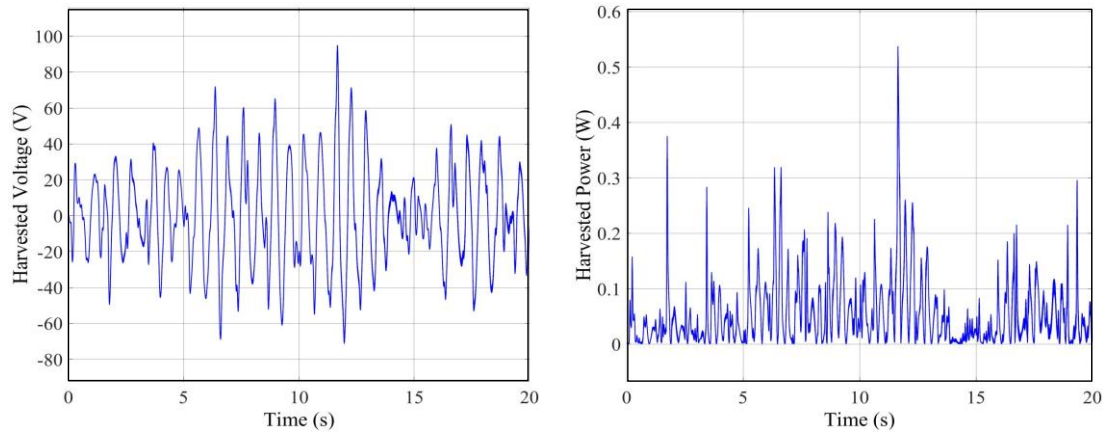


Figure 62: Harvested voltage and power on a road of class H for both QCM and HCMs.

The maximum harvested voltage and power were also studied at the most common car velocities [40 – 100 km/h] of a road surface of class C (since it considered as an average road profile). The results revealed that the harvested voltage and power from both QCM and HCM were linearly increased with the car velocity. This observation is supported by equation (68) where the velocity of the road surface is proportional to the square root of the car's velocity. It was found that the harvested

voltage and power of QCM was increased from 1.46 V to 2.3 V and 0.21 mW to 0.53 mW, when the velocity changed from 40 km/h to 100 km/h, as demonstrated in Figure 63. Likewise, the harvested voltage and power of HCM (see Figure 64) were increased approximately by 2 V and 0.45 mW at the same velocity range. This observation illustrated that, a slight increase in car velocity leads to a remarkable rise in the harvested energy.

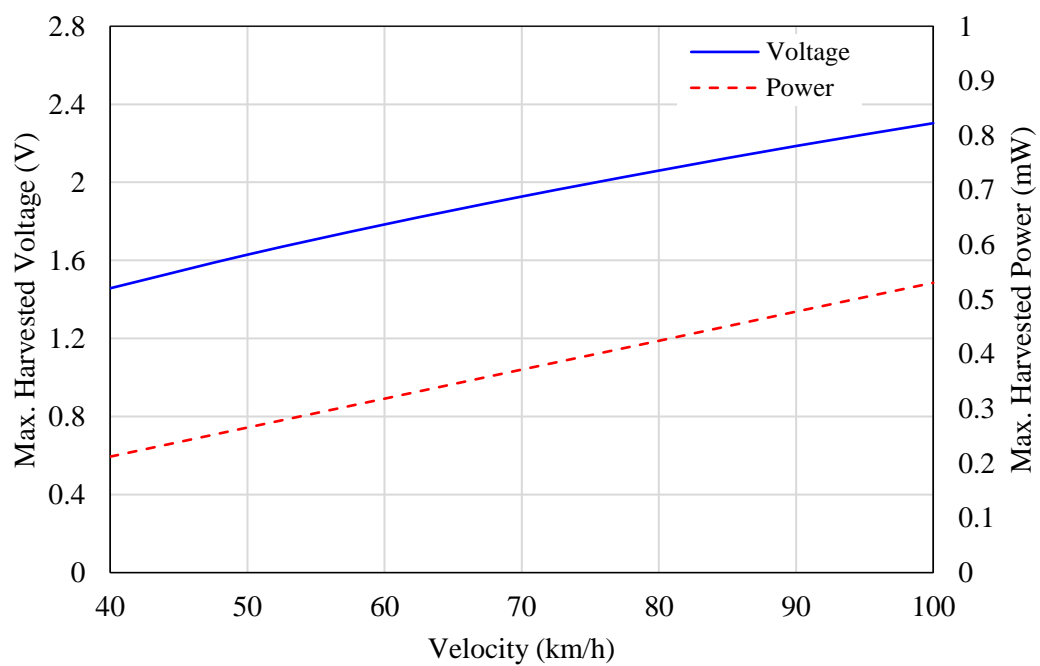


Figure 63: Harvested voltage and power on a road of class C for QCM with different car velocities.

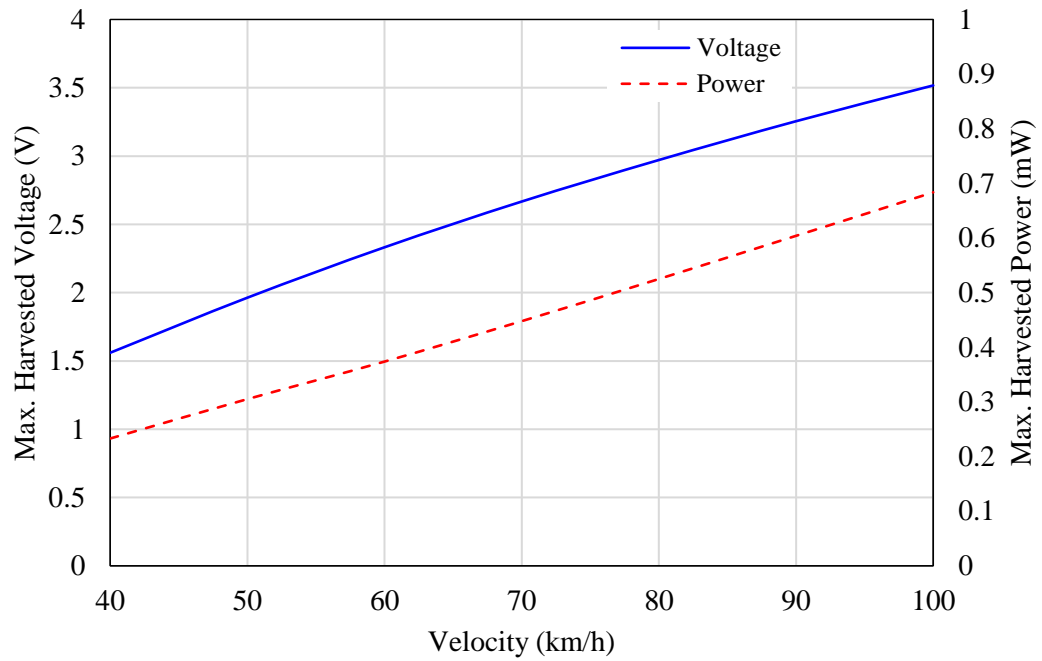


Figure 64: Harvested voltage and power on a road of class C for HCM with different car velocities.

From the results presented previously in section 5.1.1 and summarized in Table 12, it is worth noting here that, the harvested power from the quarter and half car system with a piezoelectric stack cannot be compared with different systems found in the literature. The harvested systems in the literature were different in the configuration (cantilever [118], [124], [125] and stack [126]–[129]), location of the piezoelectric element in the suspension system (springs [116], [129], [169], [170], shock absorbers [118], [125]–[128], and wheels [37], [118], [119]), the suspension system model (QCM [37], [118], [125], [129], [170] or HCM [116]), and the road input excitation (harmonic [116], [126], [129], [170] or random [37], [118], [125], [127]). The harvested voltage and power were approximately in range of [17.69 mV – 486 V] and [0.001 mW – 3.9 W], respectively, and the results for both QCM (19.11 V and 36.74 mW) and HCM (33.56 V and 56.35 mW) are within these ranges.

Table 12: Summarized results for quarter and half car models.

Input	Parameters	Quarter car model			Half car model		
Harmonic excitation	Resonant frequencies (Hz)	1.46	9.68		1.06	1.46	9.68
	Velocity (km/h) (resonant frequency)	26.28	174.24		19	26.28	174.2
	Dissipated power (kW)	1.424	15.54		0.18	2.99	31.13
	Harvested voltage (V)	19.11	1.427		17.82	33.6	2.815
	Harvested power (mW)	36.74	0.204		31.74	56.4	0.396
Random excitation	Road profile grade	A	C	H	A	C	H
	Harvested voltage (V)	0.51	2.06	65.9	0.74	2.97	95.06
	Harvested power (mW)	0.02	0.42	434.3	0.03	0.52	537.5

5.1.2 Effect of different parameters on the HCM

The harvested voltage and power from the piezoelectric stacks attached in series with the suspension springs were investigated according to road input excitation, piezoelectric parameters, and car suspension parameters.

The effect of sine wave acceleration amplitude on the harvested voltage and power at the excitation frequency of 1.46 Hz are depicted in Figure 65. The output voltage from the piezoelectric stack raised linearly from 6.7 V to 67.03 V when road acceleration amplitude increased from 0 g to 1 g. While, the output power increased in a quadratic relationship (as the power is a square of the voltage over the resistance) with minimum and maximum harvested power of 2.25 mW and 225 mW, respectively. It can be noticed that, the harvested voltage and power increased with the amplitude road unevenness. This is due to the change of the linear momentum of the car, which

means an increase of the car velocity and consequently increases the harvested voltage and power with respect to the unevenness amplitude.

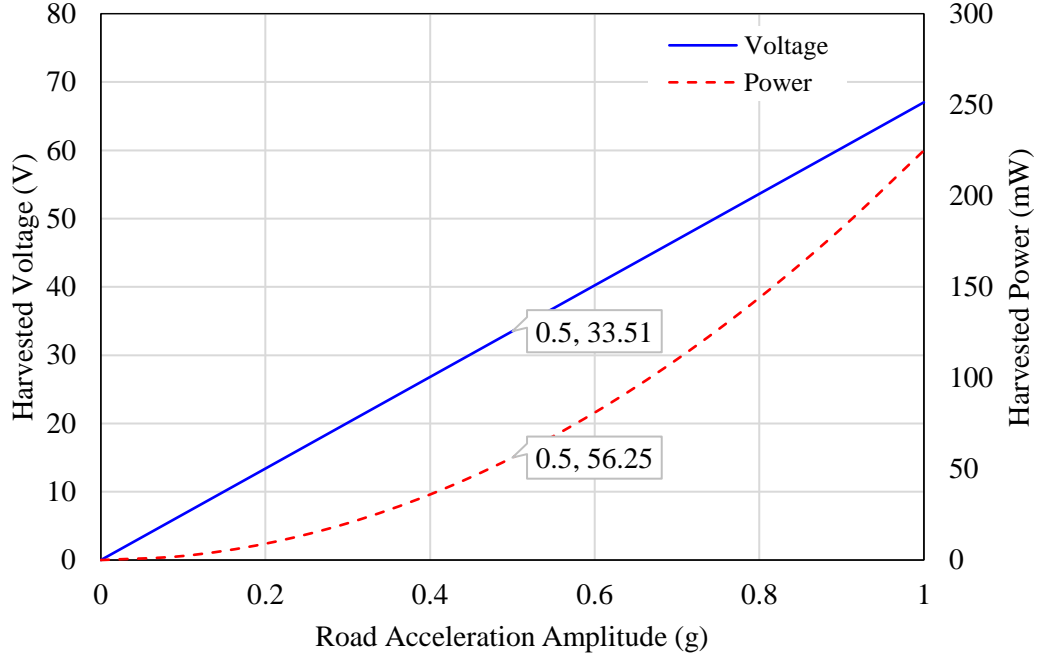


Figure 65: Harvested voltage and power vs. different amplitudes of road unevenness at excitation frequency of 1.46 Hz.

The effect of the piezoelectric stack parameters on the performance of the energy harvesting model was also investigated. The analysis was done for multiple numbers of layers up to 100 layers. The results demonstrated in Figure 66 show that, increasing the number of layers increases linearly the harvested voltage and exponentially the harvested power. Since the stack layers were connected electrically in parallel, the total displacement of the piezoelectric stack was expressed in reference [27] as

$$Y_{stack} = NY_p = \frac{1}{K_p} F_p + Nd_{33}V \quad (70)$$

This means that, the overall displacement of the stack increases with the number of layers which will consequently decrease the stiffness of the piezoelectric stack.

Besides, the total charge in the piezoelectric stack is the summation of the output charge of all layer. This observation is supported by equation (71). As a result, the output voltage and power from the proposed piezoelectric stack with 40 up to 100 layers increased by 54 V and 0.3 W.

$$Q_{stack} = NQ_p = nd_{33}f + C_pV \quad (71)$$

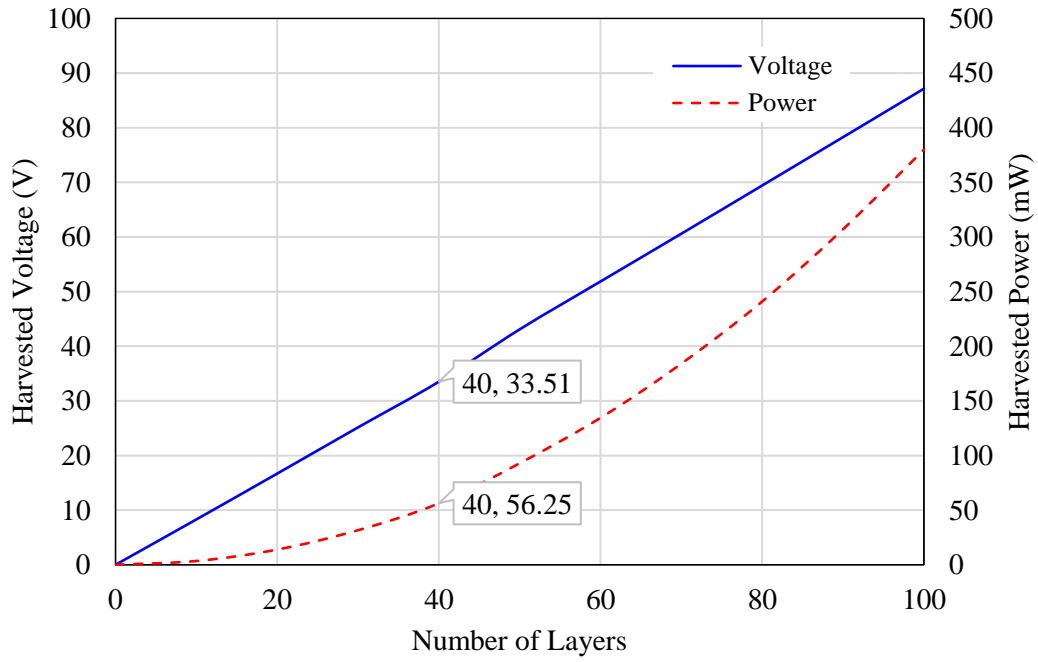


Figure 66: The effect of the number of layers of the piezoelectric stack on the harvested power.

The effect of another parameter of the piezoelectric stack that can be studied was the area to thickness ratio. This parameter will affect different parameters such as the force factor, stiffness, and capacitance of the piezoelectric material. The ratio was examined within a range from 1 mm to 1000 mm. As shown in Figure 67, increasing the area/thickness ratio will significantly increase the harvested power by 0.3 W due to the increase of the electric generating capacity of the piezoelectric stack.

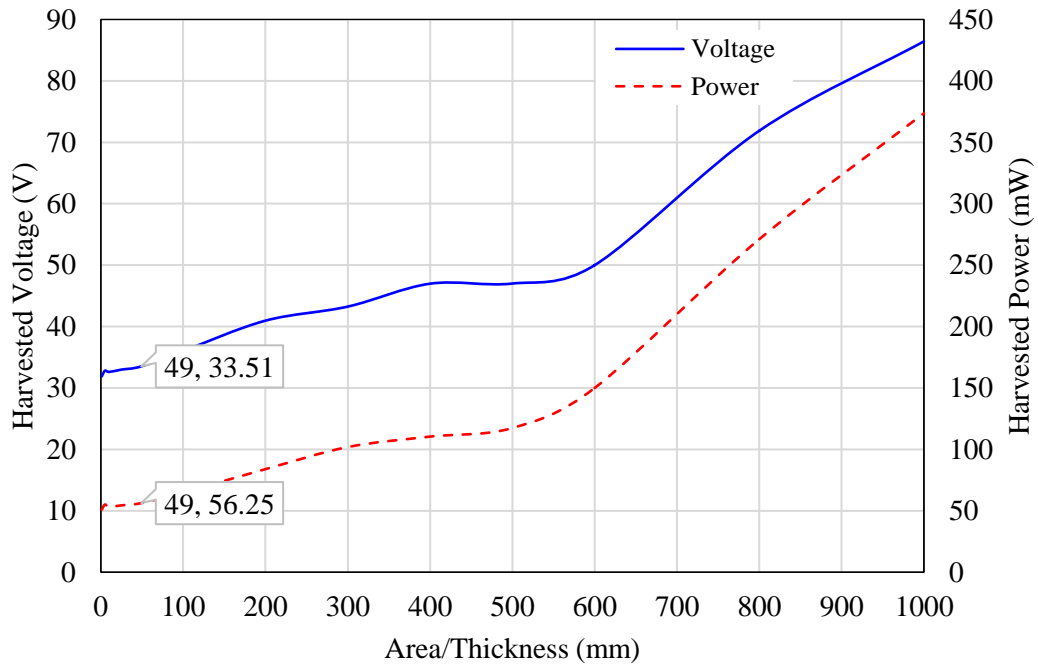


Figure 67: The effect of area/thickness ratio of the piezoelectric stack on the harvested power.

The effect of the car selected parameters on the performance of the half car piezoelectric energy harvesting model was examined as well. This was done by varying the values of the selected parameter and keeping the other car parameters in Table 9 constant. The influence of the sprung and unsprung stiffness coefficients is demonstrated in Figure 68 through Figure 70. The results showed that both the sprung and unsprung resonant frequencies increase with increasing the stiffness coefficient. This result is validated by the relationship between the natural frequencies of the system and the stiffness coefficient constant (i.e., $\omega = \sqrt{\frac{K}{M}}$). Also, increasing the suspension stiffness will increase the relative displacement between the sprung and unsprung masses. Accordingly, this will rise the harvested power from the piezoelectric stack as shown in Figure 68. In contrast, increasing the tire stiffness will decrease the resonance power (see Figure 69). This means that stiffer tires result in a harder ride and less suspension movement.

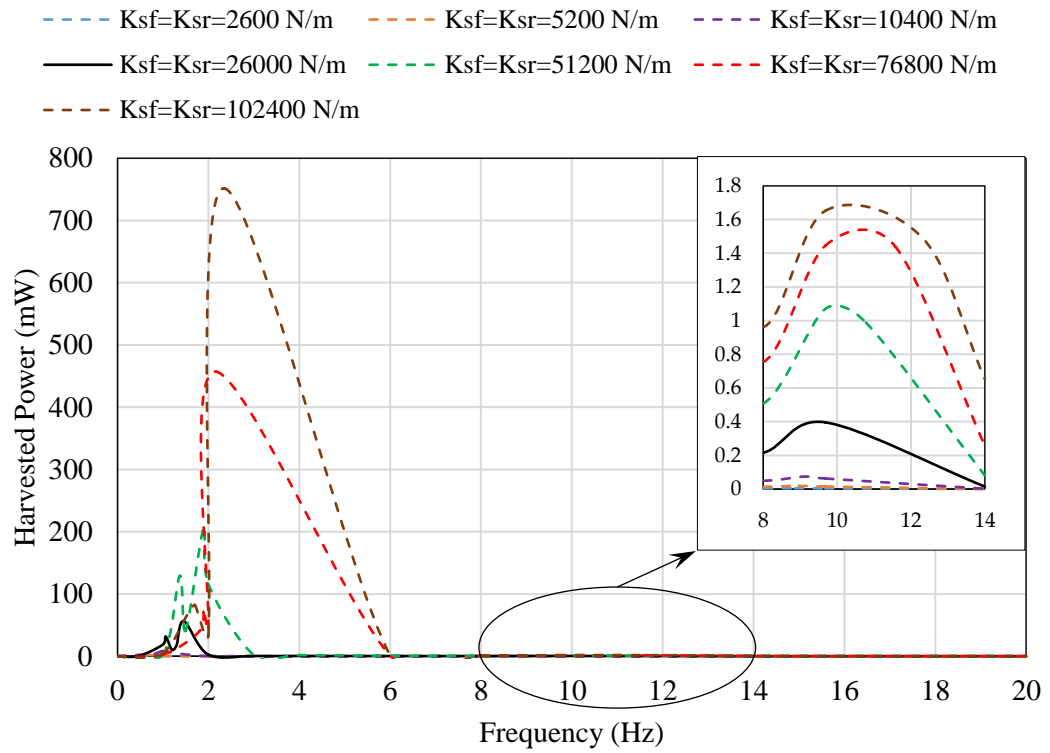


Figure 68: Effect of the sprung stiffness coefficient on the harvested power.

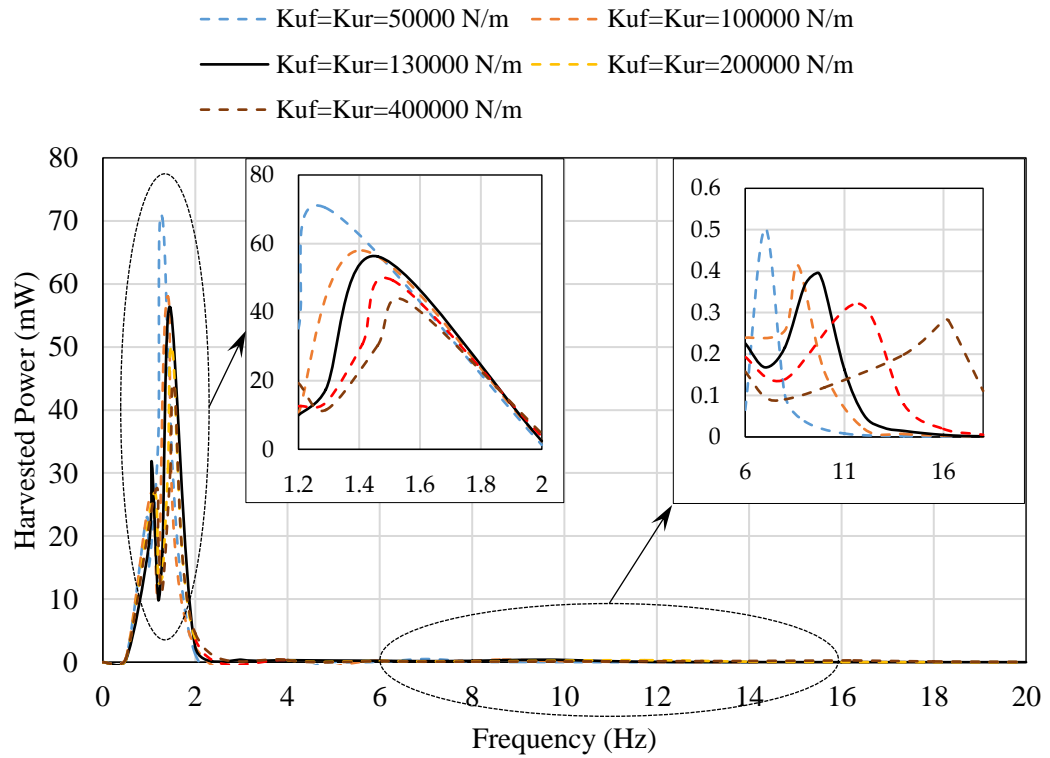


Figure 69: Effect of the unsprung stiffness coefficient on the harvested power.

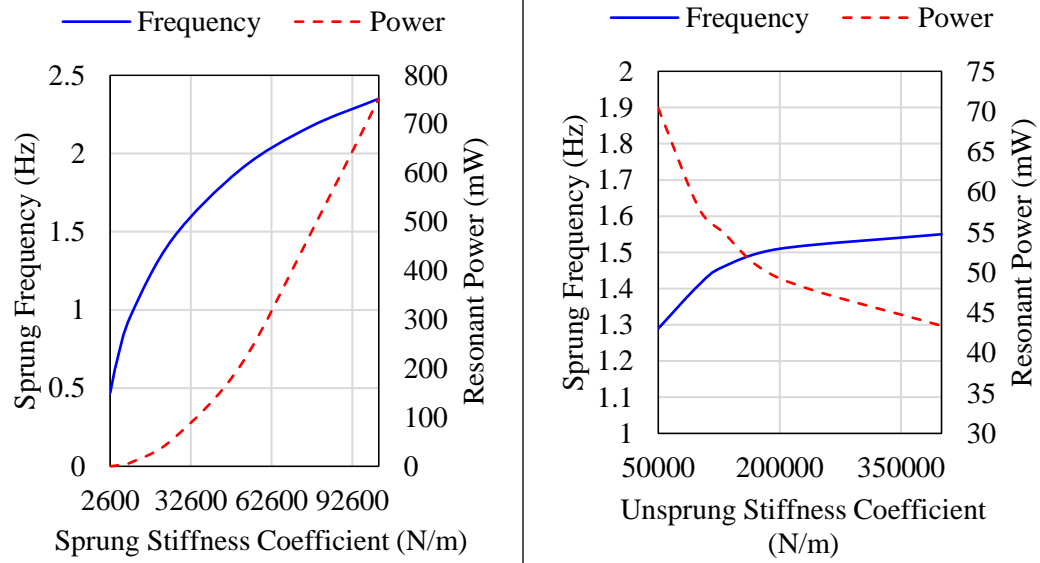


Figure 70: Effect of the sprung and unsprung stiffness coefficient on the output sprung resonant frequency and power.

Figure 71 through Figure 73 demonstrate the influence of the sprung and unsprung damping coefficient. The results showed that, the damping coefficient will not affect the sprung and unsprung resonant frequencies since there is no direct relationship between the damping coefficient and the frequency of the system. However, increasing the damping coefficient for both masses will significantly reduce the output resonance power. However, this will It was noticed that less suspension damping will provide higher harvested power by allowing more stress to be applied to the piezoelectric material. Conversely, having lightly damped or soft suspension will reduce car handling performance and stability [160], [163].

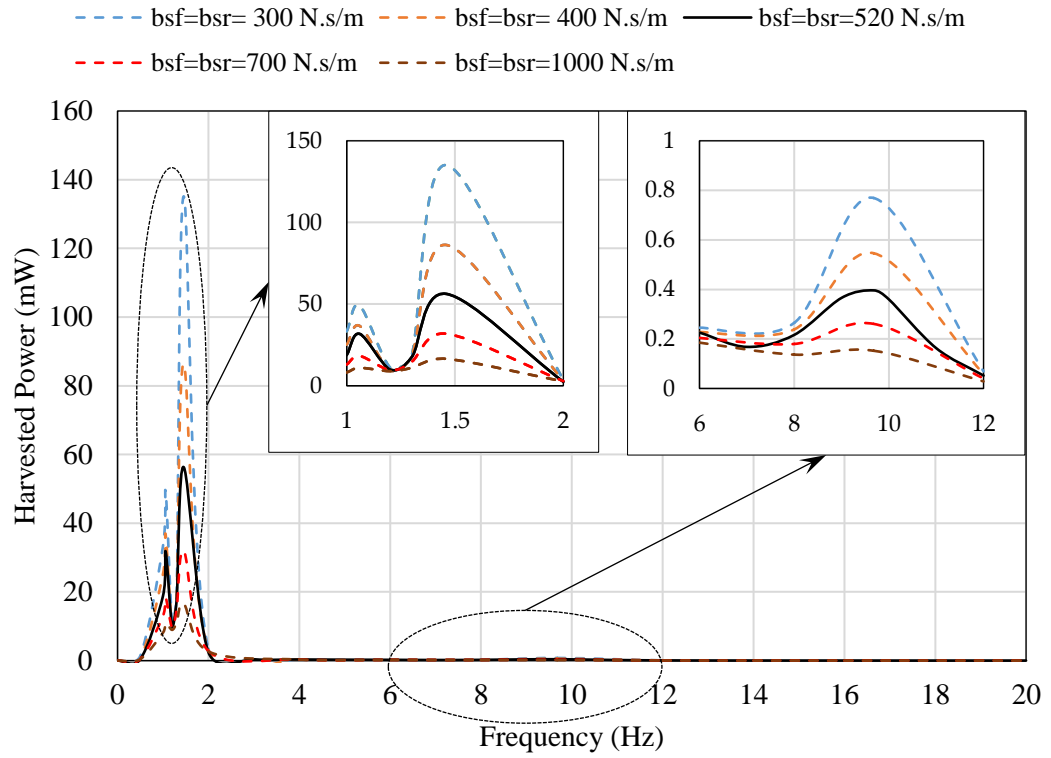


Figure 71: Effect of the sprung damping coefficient on the harvested power.

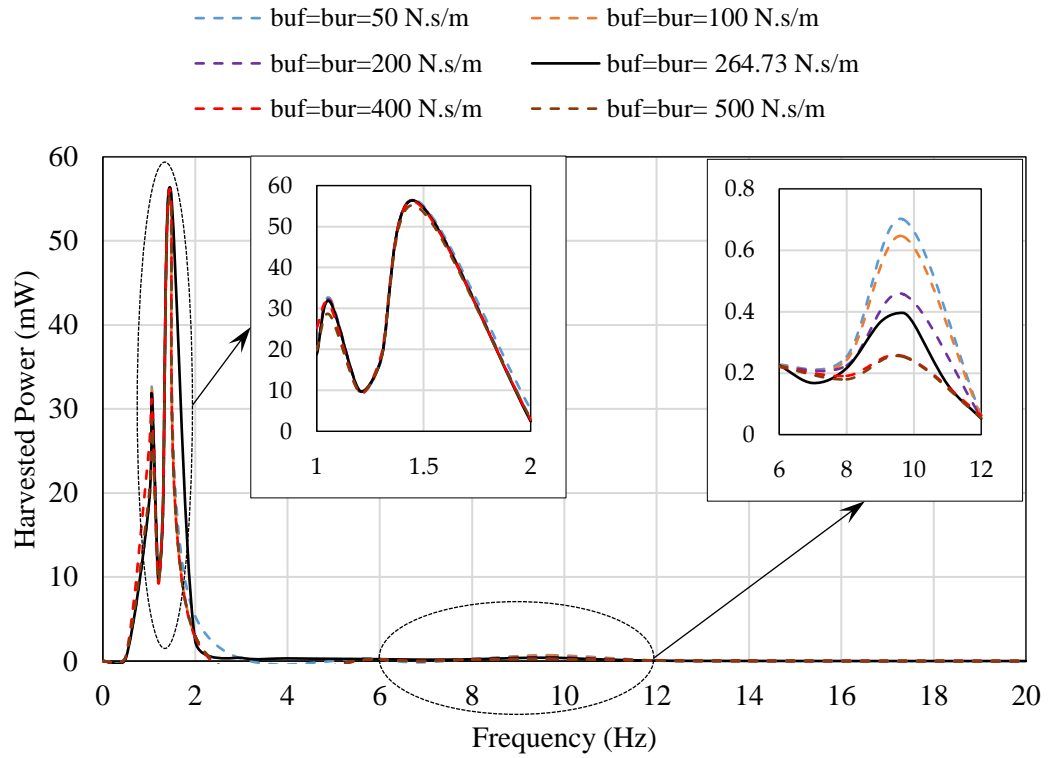


Figure 72: Effect of the unsprung damping coefficient on the harvested power.

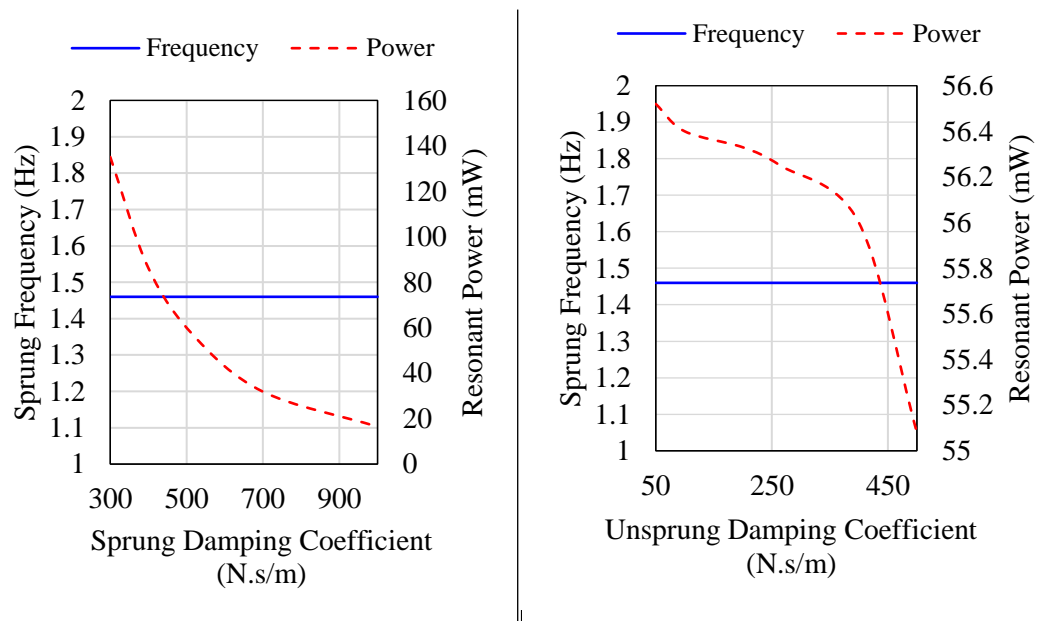


Figure 73: Effect of the sprung/unsprung damping coefficient on the output sprung resonant frequency and power.

For the influence of the sprung and unsprung masses, Figure 74 to Figure 76 show that, increasing both masses will decrease the resonant frequency for each system and this is due to the inverse relationship between the mass and frequency of the system. Although the resonant frequency mode for the both masses was decreased, the output power was kept increasing. The results also show that, the sprung mass is only affecting the sprung bounce frequency, while the unsprung mass is only affecting the unsprung bounce frequency.

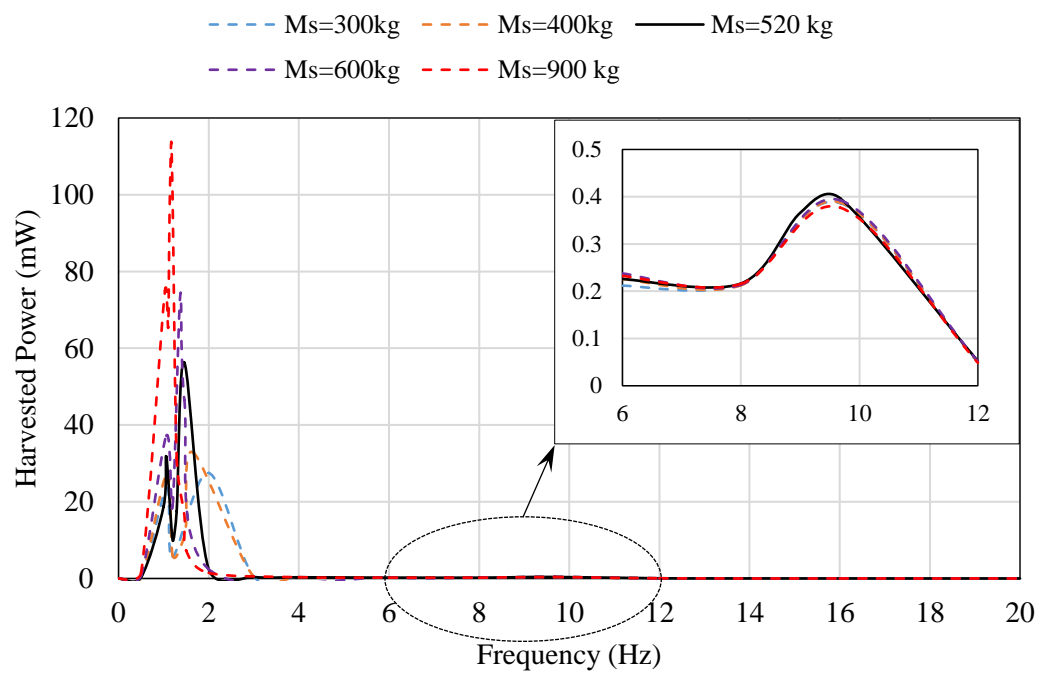


Figure 74: Effect of the sprung mass on the harvested power.

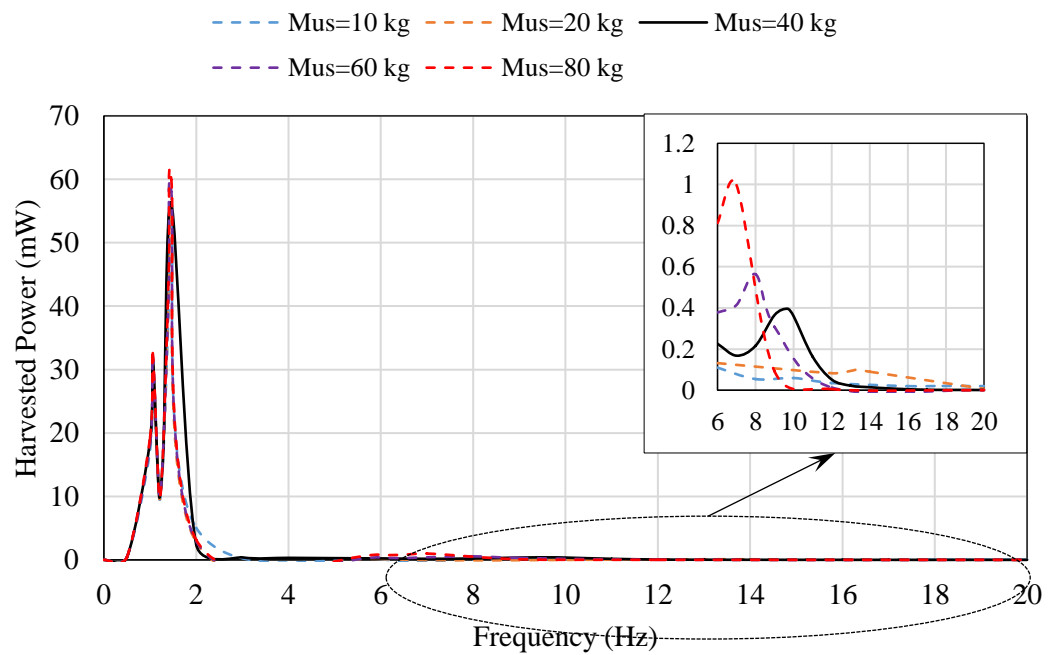


Figure 75: Effect of the unsprung mass on the harvested power.

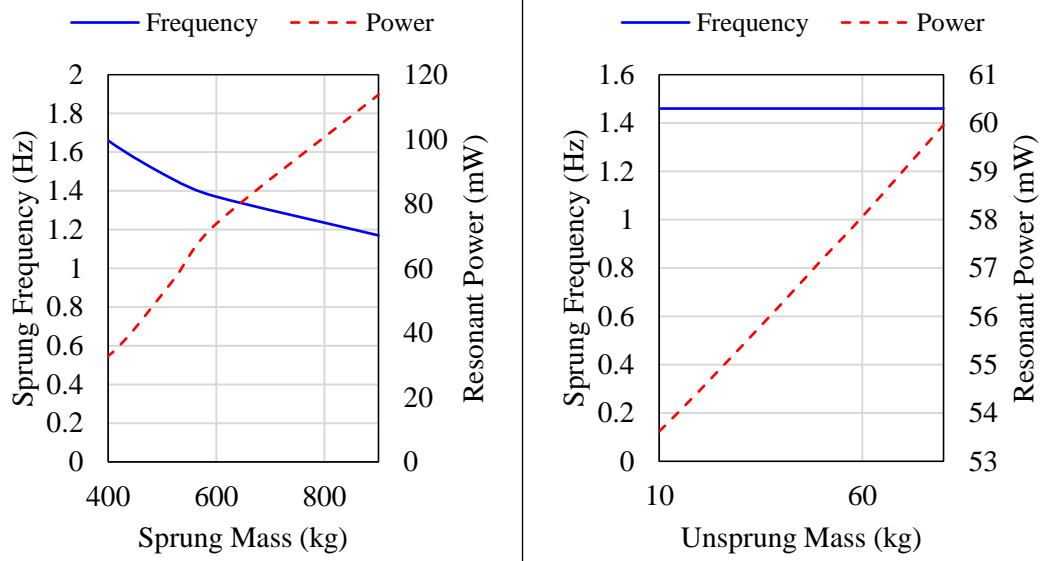


Figure 76: Effect of the sprung and unsprung masses on the output sprung resonant frequency and power.

The previous results showed that, there is a significant potential for harvesting energy from the CSS. The vibrations generated from the road excitation are transmitted to the CSS, and the produced stress/deformation will be applied to the piezoelectric stack material and create a significant amount of an electric charges. Without these harvesters, the vibration energy is wasted and dissipated into heat. Moreover, the CSS and piezoelectric stack parameters have shown an essential impact on the amount of harvested energy.

5.2 Experimental results

The QCM with the experiment parameters shown in Table 13 were investigated theoretically and experimentally. The K_s is the sum of the stiffness values of the four springs located between the sprung and unsprung plates, and K_{us} is the sum of the stiffness values of the four springs located between the unsprung and road plates. The b_s is the sum of the viscous damping coefficient of the two shock absorbers connected

between the sprung and unsprung plates. Moreover, other suspension parameters used in the experiment are listed in Table 13.

Table 13: Suspension parameters used in the experiment.

Type	Parameter	Value	Unit
Sprung mass	M_s	1	kg
Unsprung mass	M_{us}	0.6	kg
Sprung stiffness	K_s	2800	N/m
Unsprung stiffness	K_{us}	6200	N/m
Viscous damping coefficient	b_s	50	N.s/m

The resonant frequencies of the system were calculated theoretically from the roots of the equation (72).

$$(K_{us} - M_{us}\omega^2)(K_s - M_s\omega^2) - K_s M_s \omega^2 = 0 \quad (72)$$

The sprung and unsprung resonant frequencies were found to be 7 Hz and 20 Hz, respectively. These resonant frequencies were validated experimentally from the peak values of the acceleration plot for both sprung and unsprung masses as shown in Figure 77.

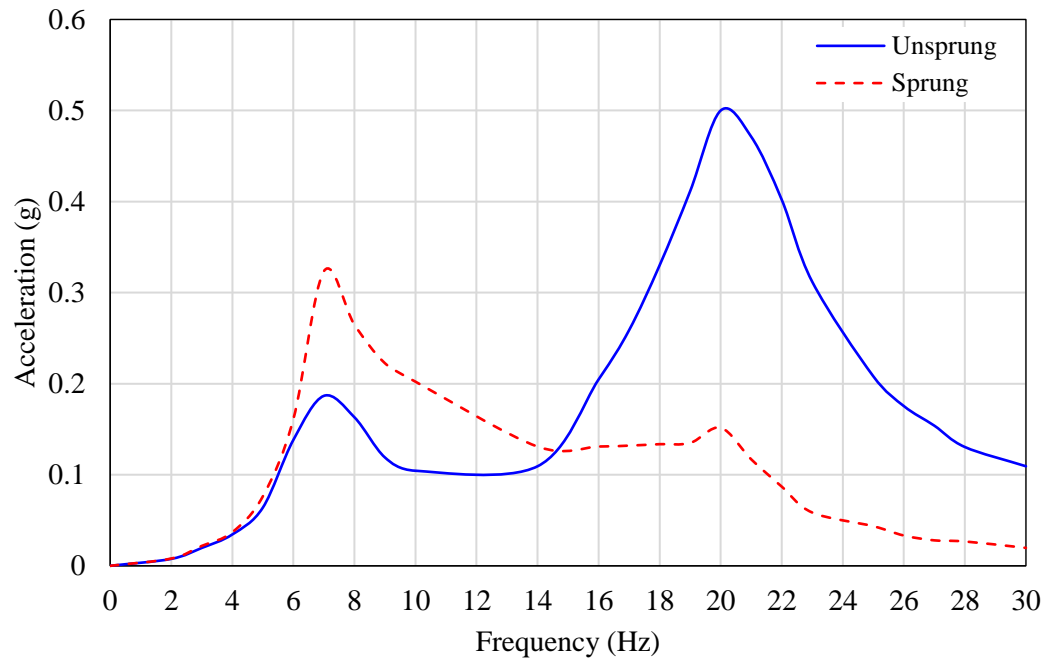


Figure 77: Sprung and unsprung resonant frequencies.

The road input acceleration was measured by the accelerometer located on the first bottom plate (road plate). The excitation amplitude acceleration was kept at 0.05 g (see Figure 66) as the system at this amplitude is stable with different excitation frequencies.

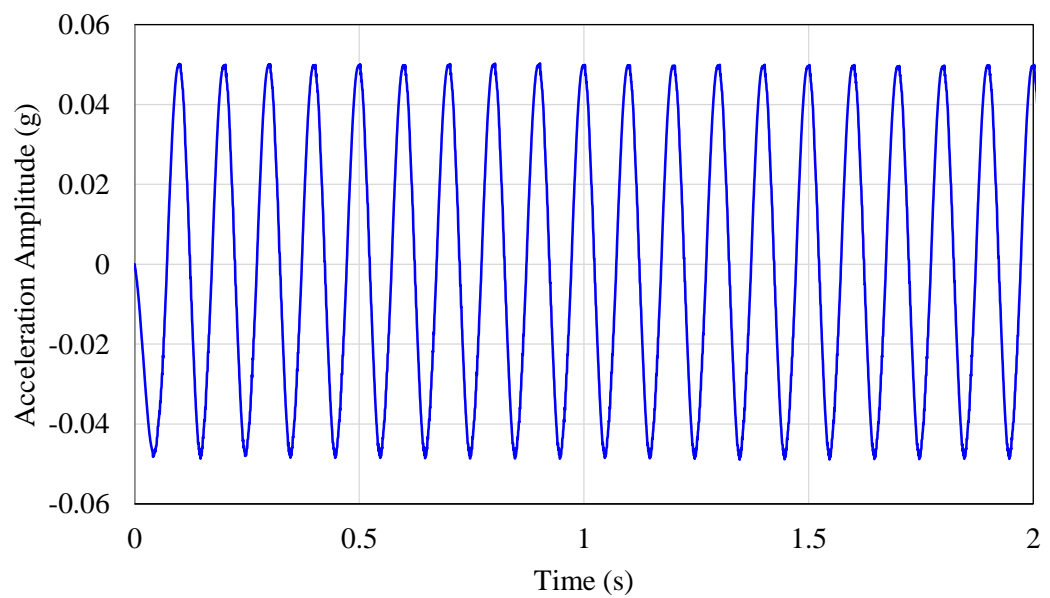


Figure 78: Input road acceleration at 0.05 g.

The analytical and experimental output voltage and power were studied at different excitation frequencies. The analytical output voltage in good agreement with the experimental voltage from piezoelectric stack as shown in Figure 79. The results show that, the greatest voltage output for both analytical and experimental studies was occurred at a sprung resonant frequency of 7 Hz. At this resonant mode, the corresponding analytical voltage was 0.14 V which is slightly higher than the experimental voltage that was recorded as 0.12 V. This small difference with a percentage error of 14% was due to some experimental errors. The errors may be due to not considering the damping coefficient of the PZT stacks in the simulation. Also, the mutual friction between the moving plates could have an effect. However, the second peak was found to be at an unsprung resonant frequency of 20 Hz. At this frequency, the analytical and experimental voltages were almost equal with a value of 0.02 V.

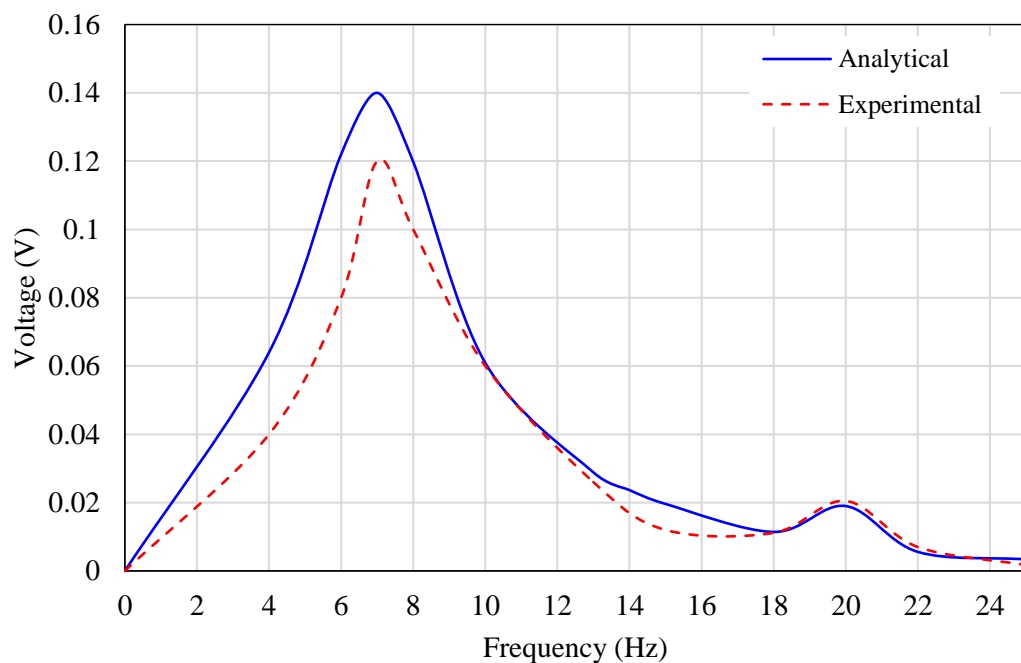


Figure 79: The analytical and experimental voltage in frequency domain for QCM.

In order to calculate the harvested power from the piezoelectric stack, a circuit should be connected to the system. It is worth noting here that, Xiao et al. [115] who evaluated the harvested voltage from the QCM is the only experimental work available in the literature. In this study, since the harvested voltage is relatively small, each piezoelectric stack was connected to the electrical circuit (PDU100B) to magnify the output voltage. As shown in Figure 80, the peak values of 6 V and 1 V are recorded at the resonant frequencies. These voltage values were magnified by a factor of 50 due to the configuration used in this circuit which is the unipolar input with bipolar output type. The output power was also calculated by having the built-in impedance circuit of 100 k Ω for unipolar input type. The results show that, the maximum harvested power from piezoelectric stack was found to be 0.36 mW. However, at the unsprung resonant frequency, the output power was 0.05 mW.

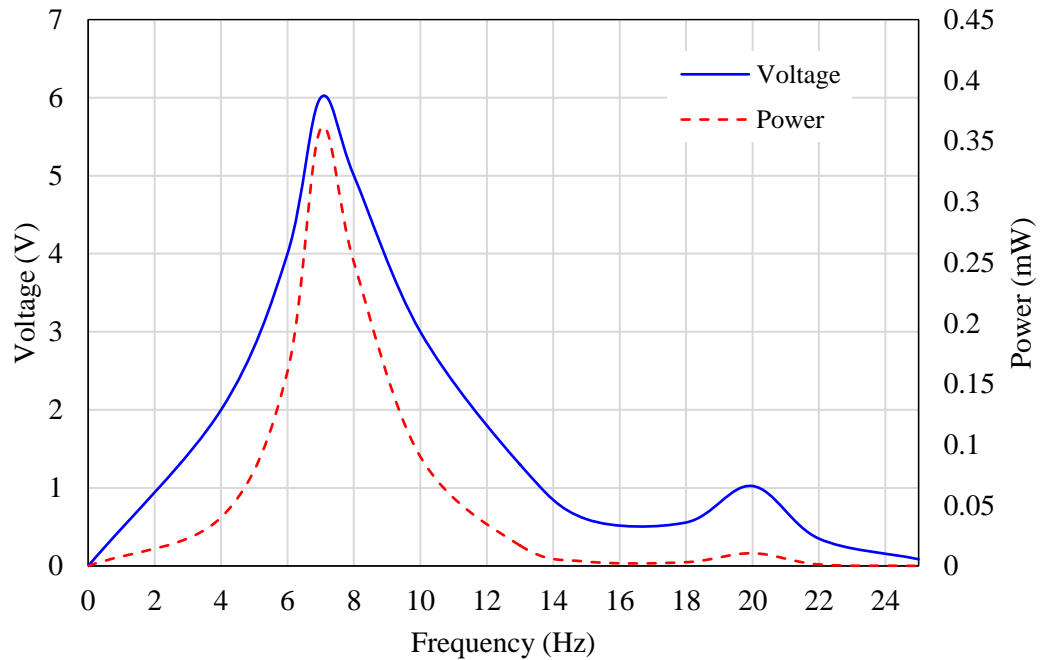


Figure 80: The magnified experimental output voltage and power in frequency domain.

Chapter 6: Conclusion and Recommendations

6.1 Conclusion

Mathematical models of quarter and half car systems with a piezoelectric stack inserted between the sprung and unsprung systems were developed to evaluate the dissipated and harvested voltage and power. The piezoelectric stacks were attached in series with the springs of the sprung mass system. The maximum output voltage and power were generated at the resonant frequencies. When the car was subjected to a harmonic excitation frequency of 1.46 Hz and an acceleration amplitude of 0.5 g, the peak values for the QCM were 19.11 V and 36.74 mW for the generated voltage and power, respectively. However, the HCM produced a harvested voltage of 1.8 and a power of 1.6 times greater than the QCM. The variation of the voltage and power vs. frequency showed a similar trend to that with the car velocity as the velocity and frequency are in direct correlation to each other. The system was also tested at the most common car velocity ranges that corresponded to the non-resonance frequencies. The results showed that, the system could also harvest a remarkable power, out of the resonance frequencies, ranges from 0.24 to 1.5 mW. Both QCM and HCM were subjected to the roughness of road surfaces as well. The results confirmed that, the minimum harvested voltage and power were found at the best road quality (class A), and the maximum harvested voltage and power were found at the poor road quality (class H). The results also illustrated that the harvested voltage and power were increased with car's velocity.

Effect of different factors on the harvested voltage and power of the HCM subjected to harmonic excitation of 0.5 g acceleration amplitude were examined. The findings demonstrated that, the more road unevenness amplitude, the higher the

harvested power. Furthermore, the parameters of the piezoelectric stack (e.g., number of layers and the area to thickness ratio) were found to influence the harvested power significantly. The observations indicated that, increasing these parameters will remarkably increase the harvested power from the piezoelectric stack.

Additionally, car suspension parameters had a considerable effect on the harvested power. Stiffer suspension springs provided higher resonant frequency and higher relative displacement of the car and piezoelectric stack that consequently increased the harvested power. Whereas, stiffer tires decreased the harvested power due to the less suspension movement and hard ride. On the other hand, increasing the damping coefficients of the sprung and unsprung systems reduced the harvested power. This is because of decreasing the unwanted vibrations in the suspension system. However, low damping coefficients produced higher harvested power by providing more stresses on the piezoelectric stack. But it affected negatively the car handling performance and stability. Therefore, it would be recommended in the future work to determine a balance point between both the car handling performance and the amount of the harvested energy. Regarding the effect of car's mass, the results illustrated that the power was increased with an increase of sprung and unsprung mass systems. However, the lightweight cars are preferred for isolating the disturbances from road excitations.

The analytical approach of the QCM was verified experimentally. The QCM was built by having three plates connected by a set of springs and dampers. By fixing the input acceleration at 0.05 g, the output voltages were matched at the second resonant frequency. However, at the first resonant frequency, there was a slight increase in the analytical voltage when compared to the experimental one. In order to

maximize the output voltage, the piezoelectric stacks were connected directly to the electrical circuits. This led to an increase in the output voltage from 0.12 V to 6 V. A value of 0.36 mW for the harvested power was also recorded at the sprung resonant frequency.

It can be observed from the findings as well as the literature results that regardless of the technique used in energy harvesting from the CSS, yet the outcome was still limited (from 0.001 mW to 3.9 W) if compared with the available dissipated energy. Different methods could be suggested here in order to maximize the harvested power. Producing tailored piezoelectric elements with improved material characteristics in converting most of the mechanical vibrations from cars into electrical power (i.e., efficiency) is one of the possible ways. It has also been noticed in this experimental research that, the harvested power was diminishing due to the degradation in the durability and sustainability of the commercially available piezoelectric material. This was also confirmed from the study of the East Japan railway company in Japan station [77]. After three weeks of their study in implementing the piezoelectric material underneath the ticket gate area, the harvested power decreased though the number of passed people increased. It is not only the material of the harvester affects the output power, but also the direction of the applied mechanical force, as well as the energy harvester configuration, play an essential role in increasing the output power. For instance, having the piezoelectric stack geometry helps in amplifying the charge production when compared to the piezoelectric cantilever benders. Developing electric circuits with storage devices like a battery also assists in maximizing the generated power by minimizing the current discharge rate.

6.2 Recommendations for future studies

In this work, the study of both analytical and experimental models was built up to study the harvested energy from CSS. Piezoelectric stack with rectangular cross section was installed in series with the suspension springs. This study can be extended to consider the following points:

- Evaluate the harvested voltage and power theoretically from full car model.
- Build up a setup for a real car suspension system equipped with piezoelectric material to evaluate experimentally the possible harvested power under different conditions.
- Investigate the effect of piezoelectric material in different locations and configurations on the harvested power.
- Evaluate the harvested energy by different harvesting techniques such as electromagnetic and electrostatic and compare the results with piezoelectric material.

References

- [1] M. Z. Jacobson *et al.*, “100% clean and renewable wind, water, and sunlight all-sector energy roadmaps for 139 countries of the world,” *Joule*, vol. 1, no. 1, pp. 108–121, 2017.
- [2] B. P. Heard, B. W. Brook, T. M. Wigley, and C. J. Bradshaw, “Burden of proof: A comprehensive review of the feasibility of 100% renewable-electricity systems,” *Renew. Sustain. Energy Rev.*, vol. 76, pp. 1122–1133, 2017.
- [3] D. Krüger, S. Fischer, and C. Buschmann, “Solar power harvesting—modeling and experiences,” *GIITG KuVS Fachgespr. Drahtlose Sensornetze*, vol. 8, pp. 1–4, 2009.
- [4] V. Raghunathan, A. Kansal, J. Hsu, J. Friedman, and M. Srivastava, “Design considerations for solar energy harvesting wireless embedded systems,” in *Proceedings of the 4th international symposium on Information processing in sensor networks*, p. 64, 2005.
- [5] D. Dondi, A. Bertacchini, L. Larcher, P. Pavan, D. Brunelli, and L. Benini, “A solar energy harvesting circuit for low power applications,” in *2008 IEEE International Conference on Sustainable Energy Technologies*, pp. 945–949, 2008.
- [6] Y. K. Tan and S. K. Panda, “Energy harvesting from hybrid indoor ambient light and thermal energy sources for enhanced performance of wireless sensor nodes,” *IEEE Trans. Ind. Electron.*, vol. 58, no. 9, pp. 4424–4435, 2011.
- [7] A. Cuadras, M. Gasulla, and V. Ferrari, “Thermal energy harvesting through pyroelectricity,” *Sens. Actuators Phys.*, vol. 158, no. 1, pp. 132–139, 2010.

- [8] X. Lu and S.-H. Yang, "Thermal energy harvesting for WSNs," in *2010 IEEE International Conference on Systems, Man and Cybernetics*, pp. 3045–3052, 2010.
- [9] C. Sun, J. Shi, and X. Wang, "Fundamental study of mechanical energy harvesting using piezoelectric nanostructures," *J. Appl. Phys.*, vol. 108, no. 3, pp. 1-11, 2010.
- [10] N. Elvin and A. Erturk, "Introduction and methods of mechanical energy harvesting," in *Advances in Energy Harvesting Methods*, Springer, pp. 3–14, 2013.
- [11] Y. Chen *et al.*, "Mechanical energy harvesting from road pavements under vehicular load using embedded piezoelectric elements," *J. Appl. Mech.*, vol. 83, no. 8, pp. 1-7, 2016.
- [12] N. Wu, Q. Wang, and X. Xie, "Wind energy harvesting with a piezoelectric harvester," *Smart Mater. Struct.*, vol. 22, no. 9, pp. 1-9, 2013.
- [13] J. Sirohi and R. Mahadik, "Harvesting wind energy using a galloping piezoelectric beam," *J. Vib. Acoust.*, vol. 134, no. 1, pp.1-8, 2012.
- [14] B. Li, J. H. You, and Y.-J. Kim, "Low frequency acoustic energy harvesting using PZT piezoelectric plates in a straight tube resonator," *Smart Mater. Struct.*, vol. 22, no. 5, pp. 1-9, 2013.
- [15] B. Li, A. J. Laviage, J. H. You, and Y.-J. Kim, "Acoustic energy harvesting using quarter-wavelength straight-tube resonator," in *ASME 2012 International Mechanical Engineering Congress and Exposition*, pp. 467–473, 2012.
- [16] S. B. Horowitz, M. Sheplak, L. N. Cattafesta III, and T. Nishida, "A MEMS acoustic energy harvester," *J. Micromechanics Microengineering*, vol. 16, no. 9, pp. 174–181, 2006.

- [17] N. Wu, Q. Wang, and X. Xie, "Ocean wave energy harvesting with a piezoelectric coupled buoy structure," *Appl. Ocean Res.*, vol. 50, pp. 110–118, 2015.
- [18] N. V. Viet, N. Wu, and Q. Wang, "A review on energy harvesting from ocean waves by piezoelectric technology," *J. Model. Mech. Mater.*, vol. 1, no. 2, pp. 161–171, 2017.
- [19] K.-H. Kim, S.-B. Cho, H.-D. Kim, and K.-T. Shim, "Wave Power Generation by Piezoelectric Sensor Attached to a Coastal Structure," *J. Sens.*, vol. 2018, pp. 1–7, 2018.
- [20] EIA, "Use of energy in the United States explained, Energy Used for Transportation," Independent Statistics and Analysis, Washington, DC, 2019.
[Online]. Available: <https://www.eia.gov/energyexplained/us-energy-facts/>
[Accessed: 29-Aug-2018]
- [21] P. S. Zhang, "Design of electromagnetic shock absorbers for energy harvesting from vehicle suspensions," Doctoral dissertation, The Graduate School, Stony Brook University: Stony Brook, NY, USA, 2010.
- [22] S. A. Velinsky and R. A. White, "Vehicle energy dissipation due to road roughness," *Veh. Syst. Dyn.*, vol. 9, no. 6, pp. 359–384, 1980.
- [23] C. Wei and H. Taghavifar, "A novel approach to energy harvesting from vehicle suspension system: Half-vehicle model," *Energy*, vol. 134, pp. 279–288, 2017.
- [24] V.-G. Jacota, "Evaluation the Dissipated Energy by the Automobile Dampers," *Glob. J. Res. Eng.*, vol. 16, no. 1, pp. 1–9, 2017.
- [25] M. A. Abdelkareem, L. Xu, M. K. A. Ali, M. A. Hassan, A. Elagouz, and J. Zou, "On-field measurements of the dissipated vibrational power of an SUV car traditional viscous shock absorber," in *ASME 2018 International Design*

Engineering Technical Conferences and Computers and Information in Engineering Conference, 2018.

- [26] L. Segel and X. Lu, "Vehicular resistance to motion as influenced by road roughness and highway alignment," *Aust. Road Res.*, vol. 12, no. 4, pp. 211–222, 1982.
- [27] S. Cao and J. Li, "A survey on ambient energy sources and harvesting methods for structural health monitoring applications," *Adv. Mech. Eng.*, vol. 9, no. 4, pp. 1-14, 2017.
- [28] F. Yildiz, "Potential Ambient Energy-Harvesting Sources and Techniques.," *J. Technol. Stud.*, vol. 35, no. 1, pp. 40–48, 2009.
- [29] P. K. Devi, "Survey on Energy Harvesting Techniques," *Int. J. Sci. Eng. Comput. Technol.*, vol. 4, no. 10, pp. 256–259, 2014.
- [30] C. Knight, J. Davidson, and S. Behrens, "Energy options for wireless sensor nodes," *Sensors*, vol. 8, no. 12, pp. 8037–8066, 2008.
- [31] H. B. Radousky and H. Liang, "Energy harvesting: an integrated view of materials, devices and applications," *Nanotechnology*, vol. 23, no. 50, pp. 1-66, 2012.
- [32] S. Roundy, P. K. Wright, and J. Rabaey, "A study of low level vibrations as a power source for wireless sensor nodes," *Comput. Commun.*, vol. 26, no. 11, pp. 1131–1144, 2003.
- [33] S. Chalasani and J. M. Conrad, "A survey of energy harvesting sources for embedded systems," in *Southeastcon, 2008. IEEE*, pp. 442–447, 2008.
- [34] J. Twiefel and H. Westermann, "Survey on broadband techniques for vibration energy harvesting," *J. Intell. Mater. Syst. Struct.*, vol. 24, no. 11, pp. 1291–1302, 2013.

- [35] S. Priya and D. J. Inman, *Energy harvesting technologies*, Springer, vol. 2, 2009.
- [36] A.-R. El-Sayed, K. Tai, M. Biglarbegian, and S. Mahmud, "A survey on recent energy harvesting mechanisms," in *Electrical and Computer Engineering (CCECE), 2016 IEEE Canadian Conference on*, pp. 1–5, 2016.
- [37] X. D. Xie and Q. Wang, "Energy harvesting from a vehicle suspension system," *Energy*, vol. 86, pp. 385–392, 2015.
- [38] Y. B. Jeon, R. Sood, J.-H. Jeong, and S.-G. Kim, "MEMS power generator with transverse mode thin film PZT," *Sens. Actuators Phys.*, vol. 122, no. 1, pp. 16–22, 2005.
- [39] C. R. Saha, T. O'Donnell, H. Loder, S. Beeby, and J. Tudor, "Optimization of an electromagnetic energy harvesting device," *IEEE Trans. Magn.*, vol. 42, no. 10, pp. 3509–3511, 2006.
- [40] G. Despesse, T Jager, J Chaillout, and J Leger, "Fabrication and characterization of high damping electrostatic micro devices for vibration energy scavenging," *Proceedings of Design, Test, Integration and Packaging of MEMS and MOEMS*, pp. 386-390, 2005.
- [41] C. G. Gonzalez, V. R. Franco, M. J. Brennan, S. Da Silva, and V. L. Junior, "Energy harvesting using piezoelectric and electromagnetic transducers," in *9th Brazilian Conference on Dynamics, Control and Their Applications, Serra Negra, Brazil*, pp. 1166–1171, 2010.
- [42] A. Erturk and D. J. Inman, *Piezoelectric energy harvesting*. John Wiley & Sons, 2011.

- [43] R. T. Aljadiri, L. Y. Taha, and P. Ivey, “Wind energy harvesting systems: A better understanding of their sustainability,” in *2017 3rd International Conference on Control, Automation and Robotics (ICCAR)*, pp. 582–587, 2017.
- [44] M. B. Tayahi, B. Johnson, M. Hotzman, and G. Cadet, “Piezoelectric materials for powering wireless remote sensors,” Technical report, University of Nevada, Reno, pp. 383-386, 2002.
- [45] D. Christin, P. S. Mogre, and M. Hollick, “Survey on wireless sensor network technologies for industrial automation: The security and quality of service perspectives,” *Future Internet*, vol. 2, no. 2, pp. 96–125, 2010.
- [46] J. Chen, X. Cao, P. Cheng, Y. Xiao, and Y. Sun, “Distributed collaborative control for industrial automation with wireless sensor and actuator networks,” *IEEE Trans. Ind. Electron.*, vol. 57, no. 12, pp. 4219–4230, 2010.
- [47] G. Park, T. Rosing, M. D. Todd, C. R. Farrar, and W. Hodgkiss, “Energy harvesting for structural health monitoring sensor networks,” *J. Infrastruct. Syst.*, vol. 14, no. 1, pp. 64–79, 2008.
- [48] J. Ko, C. Lu, M. B. Srivastava, J. A. Stankovic, A. Terzis, and M. Welsh, “Wireless sensor networks for healthcare,” *Proc. IEEE*, vol. 98, no. 11, pp. 1947–1960, 2010.
- [49] W. H. Liao, D. H. Wang, and S. L. Huang, “Wireless monitoring of cable tension of cable-stayed bridges using PVDF piezoelectric films,” *J. Intell. Mater. Syst. Struct.*, vol. 12, no. 5, pp. 331–339, 2001.
- [50] C. F. García-Hernández, P. H. Ibarguengoytia-Gonzalez, J. García-Hernández, and J. A. Pérez-Díaz, “Wireless sensor networks and applications: a survey,” *IJCSNS Int. J. Comput. Sci. Netw. Secur.*, vol. 7, no. 3, pp. 264–273, 2007.

- [51] L. Chalard, D. Helal, L. Verbaere, and A. Wellig, “Wireless sensor networks devices: Overview, issues, state-of the art and promising technologies,” in *ST Journal of Research*, vol. 4, no. 1, pp. 4–8, 2007.
- [52] L. Ruiz-Garcia, L. Lunadei, P. Barreiro, and I. Robla, “A review of wireless sensor technologies and applications in agriculture and food industry: state of the art and current trends,” *sensors*, vol. 9, no. 6, pp. 4728–4750, 2009.
- [53] K. Uchino, *Advanced piezoelectric materials: Science and technology*. Woodhead Publishing, 2017.
- [54] T. R. Meeker, “Publication and proposed revision of ANSI/IEEE standard 176-1987,” *IEEE Trans. Ultrason. Ferroelectr. Freq. Control*, vol. 43, no. 5, pp. 717–772, 1996.
- [55] H. F. Hassan, S. I. S. Hassan, and R. A. Rahim, “Acoustic energy harvesting using piezoelectric generator for low frequency sound waves energy conversion,” *Int. J. Eng. Technol. IJET*, vol. 5, no. 6, pp. 4702–4707, 2014.
- [56] S. R. Anton and H. A. Sodano, “A review of power harvesting using piezoelectric materials (2003–2006),” *Smart Mater. Struct.*, vol. 16, no. 3, pp. 1–21, 2007.
- [57] R. Calìò *et al.*, “Piezoelectric energy harvesting solutions,” *Sensors*, vol. 14, no. 3, pp. 4755–4790, 2014.
- [58] R. Ambrosio, A. Jimenez, J. Mireles, M. Moreno, K. Monfil, and H. Heredia, “Study of piezoelectric energy harvesting system based on PZT,” *Integr. Ferroelectr.*, vol. 126, no. 1, pp. 77–86, 2011.
- [59] P. Kumar, “Piezo-smart roads,” *Int. J. Enhanc. Res. Sci. Technol.*, vol. 2, no. 6, pp. 65–60, 2013.

- [60] N. Makki and R. Pop-Iliev, "Piezoelectric power generation in automotive tires," *Proc. Smart Mater. Struct. Aerospace NDT Can.*, 2011.
- [61] T. H. Ng and W. H. Liao, "Sensitivity analysis and energy harvesting for a self-powered piezoelectric sensor," *J. Intell. Mater. Syst. Struct.*, vol. 16, no. 10, pp. 785–797, 2005.
- [62] H. Liu, J. Zhong, C. Lee, S.-W. Lee, and L. Lin, "A comprehensive review on piezoelectric energy harvesting technology: Materials, mechanisms, and applications," *Appl. Phys. Rev.*, vol. 5, no. 4, pp. 1-35, 2018.
- [63] S.-G. Kim, S. Priya, and I. Kanno, "Piezoelectric MEMS for energy harvesting," *MRS Bull.*, vol. 37, no. 11, pp. 1039–1050, 2012.
- [64] H. Huang and J. F. Scott, *Ferroelectric Materials for Energy Applications*. John Wiley & Sons, 2018.
- [65] B. Yang, H. Liu, J. Liu, and C. Lee, *Micro and Nano Energy Harvesting Technologies*. Artech House, 2014.
- [66] S.-B. Kim, H. Park, S.-H. Kim, H. C. Wickle, J.-H. Park, and D.-J. Kim, "Comparison of MEMS PZT cantilevers based on d31 and d33 modes for vibration energy harvesting," *J. Microelectromechanical Syst.*, vol. 22, no. 1, pp. 26–33, 2012.
- [67] M. Goldfarb and L. D. Jones, "On the efficiency of electric power generation with piezoelectric ceramic," *J. Dyn. Syst. Meas. Control*, vol. 121, no. 3, pp. 566–571, 1999.
- [68] D. J. Leo, *Engineering analysis of smart material systems*. John Wiley & Sons, 2007.
- [69] L. APC International, *Piezoelectric ceramics: principles and applications*. APC International, 2002.

- [70] N. S. Shenck and J. A. Paradiso, "Energy scavenging with shoe-mounted piezoelectrics," *IEEE Micro*, vol. 21, no. 3, pp. 30–42, 2001.
- [71] Y.-M. Choi, M. G. Lee, and Y. Jeon, "Wearable Biomechanical Energy Harvesting Technologies," *Energies*, vol. 10, no. 10, pp. 1-17, 2017.
- [72] M. Leinonen, J. Palosaari, M. Sobocinski, J. Juuti, and H. Jantunen, "Energy harvesting from vibration and walking with piezoelectric materials," Technical report, University of Oulu, Microelectronics and Material Physics Laboratories, Finland, 2019.
- [73] J. Kymissis, C. Kendall, J. Paradiso, and N. Gershenfeld, "Parasitic power harvesting in shoes," in *Digest of Papers. Second International Symposium on Wearable Computers (Cat. No. 98EX215)*, pp. 132–139, 1998.
- [74] W. H. Ko, "Piezoelectric energy converter for electronic implants," US patent 3456134A, US Department of Health and Human Services (HHS), pp. 1-3, 1969.
- [75] J. Selvarathinam and A. Anpalagan, "Energy harvesting from the human body for biomedical applications," *IEEE Potentials*, vol. 35, no. 6, pp. 6–12, 2016.
- [76] P. D. Mitcheson, E. M. Yeatman, G. K. Rao, A. S. Holmes, and T. C. Green, "Energy harvesting from human and machine motion for wireless electronic devices," *Proc. IEEE*, vol. 96, no. 9, pp. 1457–1486, 2008.
- [77] East Japan Railway Company, "Demonstration experiment of the 'Power-Generating Floor' at Tokyo station," Report, JR East, Japan, pp. 1-3, 2008.
- [78] E. Rosenthal, "Partying helps power a dutch nightclub," *The New York Times*, 2008. [Online]. Available: <https://www.nytimes.com/2008/10/24/world/europe/24rotterdam.html>.
[Accessed: 20-Sep-2018]

- [79] Mail reporter, "Britain's first eco-nightclub powered by pounding feet opens its doors," Mail online, 2008. [Online]. Available: <https://www.dailymail.co.uk/sciencetech/article-1027362/Britains-eco-nightclub-powered-pounding-feet-opens-doors.html>. [Accessed: 17-Sep-2018].
- [80] I. Aminzahed, Y. Zhang, and M. Jabbari, "Energy harvesting from a five-story building and investigation of frequency effect on output power," *Int. J. Interact. Des. Manuf. IJIDeM*, vol. 10, no. 3, pp. 301–308, 2016.
- [81] J. Kan, R. J. Ross, X. Wang, and W. Li, "Energy harvesting from wood floor vibration using a piezoelectric generator," *Res. Note FPL–RN–0347 Madison WI US Dep. Agric. For. Serv. For. Prod. Lab. 9 P*, vol. 347, pp. 1-7, 2017.
- [82] A. M. Elhalwagy, M. Y. M. Ghoneem, and M. Elhadidi, "Feasibility Study for Using Piezoelectric Energy Harvesting Floor in Buildings' Interior Spaces," *Energy Procedia*, vol. 115, pp. 114–126, 2017.
- [83] H. M. Yatim, F. M. Ismail, S. E. Kosnan, Z. Mohammad, F. S. Januddi, and A. Bakri, "A Development of Piezoelectric Model as an Energy Harvester from Mechanical Vibration," *Chem. Eng.*, vol. 63, pp. 775-780, 2018.
- [84] X. Jiang, Y. Li, J. Li, J. Wang, and J. Yao, "Piezoelectric energy harvesting from traffic-induced pavement vibrations," *J. Renew. Sustain. Energy*, vol. 6, no. 4, pp. 1-16, 2014.
- [85] L. Rui, Y. C. Xiao, J. Z. Pei, and X. K. Zhao, "The Theoretical Research about the Piezoelectric Materials Generating Capacity on Road," in *Applied Mechanics and Materials*, vol. 470, pp. 807–813, 2014.
- [86] H. Abramovich, E. Harash, C. Milgrom, and U. Amit, "Energy harvesting from airport runway," US patent 20090195124A1, Innowattech Ltd, pp. 1-34, 2009.

- [87] L. A. Edery, "Innowattech: Harvesting Energy and Data; A Standalone Technology," in *Israel National Roads Company, Ltd. First International Symposium. The Highway to Innovation, Tel Aviv, Israel*, 2010, pp. 64–81.
- [88] P. Sharma and S. Rajput, *Sustainable smart cities in India: Challenges and future perspectives*. Springer, 2017.
- [89] A. Vaishnav, M. Sarvaiya, and P. Dhabaliya, "Mathematical Modelling and Comparison of Two Degree of Freedom Suspension System of Quarter Car," *Imp. J. Interdiscip. Res.*, vol. 2, no. 11, pp. 128-137, 2016.
- [90] P. Sharma, N. Saluja, D. Saini, and P. Saini, "Analysis of automotive passive suspension system with Matlab program generation," *Int. J. Adv. Technol.*, vol. 4, no. 2, pp. 115-119, 2013.
- [91] M. S. Jamali, K. A. Ismail, Z. Taha, and M. F. Aiman, "Development of Matlab Simulink model for dynamics analysis of passive suspension system for lightweight vehicle," in *Journal of Physics: Conference Series*, vol. 908, pp. 1-8, 2017.
- [92] A. Florin, M.-R. Ioan-Cozmin, and P. Liliana, "Passive suspension modeling using MATLAB, quarter-car model, input signal step type," *New Technol. Prod. Mach. Manuf. Technol.*, pp. 258–263, 2013.
- [93] G. A. Hassaan, "Car dynamics using quarter model and passive suspension, part i: Effect of suspension damping and car speed," *Int. J. Comput. Tech.*, vol. 1, no. 2, pp. 1–9, 2014.
- [94] S. Prabhakar and K. Arunachalam, "Simulation and analysis of passive suspension system for different road profiles with variable damping and stiffness parameters," *J. Chem. Pharm. Sci. Www Jchps Com ISSN*, vol. 974, pp. 32-36, 2015.

- [95] W. Gao, N. Zhang, and J. Dai, "A stochastic quarter-car model for dynamic analysis of vehicles with uncertain parameters," *Veh. Syst. Dyn.*, vol. 46, no. 12, pp. 1159–1169, 2008.
- [96] M. Salah, "A Laboratory Automotive Suspension Test Rig: Design, Implementation and Integration.," *Jordan J. Mech. Ind. Eng.*, vol. 11, no. 2, pp. 67-71, 2017.
- [97] A. C. Mitra, G. R. Kiranchand, T. Soni, and N. Banerjee, "Design of experiments for optimization of automotive suspension system using quarter car test rig," *Procedia Eng.*, vol. 144, pp. 1102–1109, 2016.
- [98] Y. Mingzhou, "Design, Modelling, and Control of a Quarter-Car Suspension System," University of Hong Kong, 2016.
- [99] L. M. Jugulkar, S. Singh, and S. M. Sawant, "Analysis of suspension with variable stiffness and variable damping force for automotive applications," *Adv. Mech. Eng.*, vol. 8, no. 5, pp. 1-19, 2016.
- [100] S. A. Patil and S. G. Joshi, "Experimental analysis of 2 DOF quarter-car passive and hydraulic active suspension systems for ride comfort," *Syst. Sci. Control Eng. Open Access J.*, vol. 2, no. 1, pp. 621–631, 2014.
- [101] Quanser Innovate and Educate, "Active suspension - Quanser," pp. 1-2, 2013.
- [102] W. Gao, N. Zhang, and H. P. Du, "A half-car model for dynamic analysis of vehicles with random parameters," in *5th Australasian Congress on Applied Mechanics (ACAM 2007)*, vol. 1, pp. 595–600, 2007.
- [103] C. B. Patel, P. P. Gohil, and B. Borhade, "Modelling and vibration analysis of a road profile measuring system," *Int. J. Automot. Mech. Eng.*, vol. 1, no. 1, pp. 13–28, 2010.

- [104] A. Mehmood, A. A. Khan, and A. A. Khan, "Vibration analysis of damping suspension using car models," *Int. J. Innov. Sci. Res.*, vol. 9, no. 2, pp. 202–211, 2014.
- [105] A. Faheem, F. Alam, and V. Thomas, "The suspension dynamic analysis for a quarter car model and half car model," in *3rd BSME-ASME International Conference on Thermal Engineering*, pp. 20–22, 2006.
- [106] B. Sapiński and P. Martynowicz, "Vibration control in a pitch-plane suspension model with MR shock absorbers," *J. Theor. Appl. Mech.*, vol. 43, no. 3, pp. 655–674, 2005.
- [107] S. P. Chavan, S. H. Sawant, and J. A. Tamboli, "Experimental Verification of Passive Quarter Car Vehicle Dynamic System Subjected to Harmonic Road Excitation with Nonlinear Parameters," *IOSR J. Mech. Civ. Eng. IOSR-JMCE*, pp. 39–45, 2013.
- [108] B. S. Institution, *Guide to measurement and evaluation of human exposure to whole-body mechanical vibration and repeated shock*. British Standards Institution, 1999.
- [109] A. Mitra, N. Benerjee, H. A. Khalane, M. A. Sonawane, D. R. Joshi, and G. R. Bagul, "Simulation and Analysis of Full Car Model for various Road profile on a analytically validated MATLAB/SIMULINK model," *IOSR J Mech Civ Eng IOSR-JMCE*, pp. 22–33, 2013.
- [110] A. B. Raju and R. Venkatachalam, "Analysis of Vibrations of Automobile Suspension System Using Full-car Model," *Int. J. Sci. Eng. Res.*, vol. 4, no. 9, pp. 2105–2111, 2013.

- [111] R. Rajale, K. K. Jagtap, S. C. Ahmednagar, and M. P. Nagarkar, "Mathematical Modelling and Simulation of Full Car Suspension System." in *ICITDCEME'15 Conference Proceedings*, pp. 1-8, 2014.
- [112] A. R. Iyer, R. Venkatachalam, and A. Balaraju, "Analysis of Optimum Suspension Parameters of a Semi-Independently Suspended Automobile," *Int. J. Innov. Res. Sci. Eng. Technol.*, vol. 3, no. 5, pp. 12047-12053, 2014.
- [113] K. M. Mahala, P. Gadkari, and A. Deb, "Mathematical models for designing vehicles for ride comfort," in *ICORD 09: Proceedings of the 2nd International Conference on Research into Design, Bangalore, India 07.-09.01. 2009*, 2009.
- [114] L. Zuo and P.-S. Zhang, "Energy harvesting, ride comfort, and road handling of regenerative vehicle suspensions," *J. Vib. Acoust.*, vol. 135, no. 1, pp. 295-302, 2013.
- [115] H. Xiao, X. Wang, and S. John, "A dimensionless analysis of a 2DOF piezoelectric vibration energy harvester," *Mech. Syst. Signal Process.*, vol. 58, pp. 355–375, 2015.
- [116] D. Al-Yafeai, T. Darabseh, and A.-H. I. Mourad, "Quarter vs. Half Car Model Energy Harvesting Systems," in *2019 Advances in Science and Engineering Technology International Conferences (ASET)*, IEEE, pp. 1–5, 2019. doi: 10.1109/ICASET.2019.8714433.
- [117] A. Azizi and P. G. Yazdi, "*White Noise: Applications and Mathematical Modeling*," in *Computer-Based Analysis of the Stochastic Stability of Mechanical Structures Driven*, Springer, pp. 25–36, 2019.
- [118] B. Lafarge, S. Grondel, C. Delebarre, and E. Cattan, "A validated simulation of energy harvesting with piezoelectric cantilever beams on a vehicle suspension using Bond Graph approach," *Mechatronics*, vol. 53, pp. 202–214, 2018.

- [119] M. M. Behera, "Piezoelectric Energy Harvesting from Vehicle Wheels," *Int. J. Eng. Res. Technol.*, vol. 4, no. 05, pp. 1-4, 2015.
- [120] L. Gu and C. Livermore, "Passive self-tuning energy harvester for extracting energy from rotational motion," *Appl. Phys. Lett.*, vol. 97, no. 8, pp. 1-3, 2010.
- [121] Y. Hu, C. Xu, Y. Zhang, L. Lin, R. L. Snyder, and Z. L. Wang, "A Nanogenerator for Energy Harvesting from a Rotating Tire and its Application as a Self-Powered Pressure/Speed Sensor," *Adv. Mater.*, vol. 23, no. 35, pp. 4068–4071, 2011.
- [122] Y. Zhang, R. Zheng, K. Shimono, T. Kaizuka, and K. Nakano, "Effectiveness testing of a piezoelectric energy harvester for an automobile wheel using stochastic resonance," *Sensors*, vol. 16, no. 10, pp. 1-16, 2016.
- [123] A. Consortium, "Intelligent tyre for accident-free traffic," *Tech. Res. Cent. Finl. VTT Tech Rep*, pp. 1-64, 2003.
- [124] H. Lee, H. Jang, J. Park, S. Jeong, T. Park, and S. Choi, "Design of a piezoelectric energy-harvesting shock absorber system for a vehicle," *Integr. Ferroelectr.*, vol. 141, no. 1, pp. 32–44, 2013.
- [125] B. Lafarge, C. Delebarre, S. Grondel, O. Curea, and A. Hacala, "Analysis and optimization of a piezoelectric harvester on a car damper," *Phys. Procedia*, vol. 70, pp. 970–973, 2015.
- [126] S. F. Ali and S. Adhikari, "Energy harvesting dynamic vibration absorbers," *J. Appl. Mech.*, vol. 80, no. 4, pp. 1-9, 2013.
- [127] C. Madhav and S. F. Ali, "Harvesting energy from vibration absorber under random excitations," *IFAC-Pap.*, vol. 49, no. 1, pp. 807–812, 2016.
- [128] M. Arizti, "Harvesting energy from vehicle suspension," Master of Science Thesis, Tampere University of Technology, Tampere, 2010.

- [129] W. Hendrowati, H. L. Guntur, and I. N. Sutantra, "Design, modeling and analysis of implementing a multilayer piezoelectric vibration energy harvesting mechanism in the vehicle suspension," *Engineering*, vol. 4, no. 11, pp. 728-738, 2012.
- [130] P. Můčka, "Energy-harvesting potential of automobile suspension," *Veh. Syst. Dyn.*, vol. 54, no. 12, pp. 1651–1670, 2016.
- [131] H. A. Sodano, D. J. Inman, and G. Park, "Comparison of piezoelectric energy harvesting devices for recharging batteries," *J. Intell. Mater. Syst. Struct.*, vol. 16, no. 10, pp. 799–807, 2005.
- [132] H. A. Sodano, D. J. Inman, and G. Park, "Generation and storage of electricity from power harvesting devices," *J. Intell. Mater. Syst. Struct.*, vol. 16, no. 1, pp. 67–75, 2005.
- [133] S. Priya, "Advances in energy harvesting using low profile piezoelectric transducers," *J. Electroceramics*, vol. 19, no. 1, pp. 167–184, 2007.
- [134] M. J. Guan and W. H. Liao, "On the efficiencies of piezoelectric energy harvesting circuits towards storage device voltages," *Smart Mater. Struct.*, vol. 16, no. 2, pp. 498–505, 2007.
- [135] G. Ottman, A. Bhatt, H. Hofmann, and G. Lesieutre, "Adaptive piezoelectric energy harvesting circuit for wireless, remote power supply," in *IEEE Transactions on Power Electronics*, vol. 17, no. 5, pp. 669-676, 2002.
- [136] G. K. Ottman, H. F. Hofmann, and G. A. Lesieutre, "Optimized piezoelectric energy harvesting circuit using step-down converter in discontinuous conduction mode," in *IEEE Transactions on Power Electronics*, vol. 18, no. 2, pp. 696-703, 2003.

- [137] M. Umeda, K. Nakamura, and S. Ueha, "Energy storage characteristics of a piezo-generator using impact induced vibration," *Jpn. J. Appl. Phys.*, vol. 36, no. 5S, pp. 3146–3151, 1997.
- [138] A. Kasyap *et al.*, "Energy reclamation from a vibrating piezoceramic composite beam," in *Proceedings of 9th International Congress on Sound and Vibration*, vol. 9, pp. 36–43, 2002.
- [139] T. Starner, "Human-powered wearable computing," *IBM Syst. J.*, vol. 35, no. 3.4, pp. 618–629, 1996.
- [140] N. G. Elvin, A. A. Elvin, and M. Spector, "A self-powered mechanical strain energy sensor," *Smart Mater. Struct.*, vol. 10, no. 2, pp. 293–299, 2001.
- [141] H. A. Sodano, E. A. Magliula, G. Park, and D. J. Inman, "Electric power generation from piezoelectric materials," in *Proceedings of the 13th International Conference on Adaptive Structures and Technologies*, pp. 7–9.
- [142] H. Chen, T. N. Cong, W. Yang, C. Tan, Y. Li, and Y. Ding, "Progress in electrical energy storage system: A critical review," *Prog. Nat. Sci.*, vol. 19, no. 3, pp. 291–312, 2009.
- [143] F. Casciati, L. Faravelli, and R. Rossi, "Architecture optimization for wireless sensor networks," in *Smart Structures and Materials 2005: Sensors and Smart Structures Technologies for Civil, Mechanical, and Aerospace Systems*, vol. 5765, pp. 253–258, 2005.
- [144] X. Jiang, J. Polastre, and D. Culler, "Perpetual environmentally powered sensor networks," *IPSN 2005. Fourth International Symposium on Information Processing in Sensor Networks*, Boise, ID, USA, pp. 463–468, 2005.

- [145] Z. Zhao, S. Wang, and C. You, "Piezoelectric micro-power generation to charge supercapacitor with optimized duty cycle," *J. Intell. Mater. Syst. Struct.*, vol. 21, no. 11, pp. 1131–1140, 2010.
- [146] H. Li, C. Tian, and Z. D. Deng, "Energy harvesting from low frequency applications using piezoelectric materials," *Appl. Phys. Rev.*, vol. 1, no. 4, pp. 1–20, 2014.
- [147] M. J. Guan and W.-H. Liao, "Characteristics of energy storage devices in piezoelectric energy harvesting systems," *J. Intell. Mater. Syst. Struct.*, vol. 19, no. 6, pp. 671–680, 2008.
- [148] R. Kötz and M. Carlen, "Principles and applications of electrochemical capacitors," *Electrochimica Acta*, vol. 45, no. 15–16, pp. 2483–2498, 2000.
- [149] M. S. Halper and J. C. Ellenbogen, "Supercapacitors: A brief overview," *MITRE Corp. McLean Va. USA*, pp. 1–34, 2006.
- [150] I. M. Tolentino and M. R. Talampas, "Design, development, and evaluation of a self-powered GPS tracking system for vehicle security," in *sensors*, pp. 1–4, 2012.
- [151] T Singh, "Piezoelectric energy generating roads proposed for California," Report, Inhabitate, Innovation, Renewable Energy, 2011. [Online]. Available: <https://inhabitat.com/piezoelectric-energy-generating-roads-proposed-for-california/> [Accessed: 05-Oct-2018]
- [152] Inhabitate, "Researchers roll out energy generating roads," Report, Inhabitate, Innovation, Renewable Energy, 2008. [Online]. Available: <https://inhabitat.com/energy-generating-roads-by-innowattech/> [Accessed: 06-Oct-2018]

- [153] E. Lefeuvre, A. Badel, C. Richard, L. Petit, and D. Guyomar, “A comparison between several vibration-powered piezoelectric generators for standalone systems,” *Sens. Actuators Phys.*, vol. 126, no. 2, pp. 405–416, 2006.
- [154] PiezoDrive, “PiezoDrive 200V Stack Actuators,” Manual and Specifications, University Drive, Australia, pp. 1-3, 2011.
- [155] X. Jiang, Y. Li, J. Li, J. Wang, and J. Yao, “Piezoelectric energy harvesting from traffic-induced pavement vibrations,” *J. Renew. Sustain. Energy*, vol. 6, no. 4, pp. 1-16, 2014.
- [156] Y. K. Ramadass and A. P. Chandrakasan, “An efficient piezoelectric energy harvesting interface circuit using a bias-flip rectifier and shared inductor,” *IEEE J. Solid-State Circuits*, vol. 45, no. 1, pp. 189–204, 2010.
- [157] T. J. Kazmierski and S. Beeby, *Energy harvesting systems*. Springer, 2014.
- [158] A. Agharkakli, G. S. Sabet, and A. Barouz, “Simulation and analysis of passive and active suspension system using quarter car model for different road profile,” *Int. J. Eng. Trends Technol.*, vol. 3, no. 5, pp. 636–644, 2012.
- [159] C.-Y. Lin, “Material characterization and modeling for piezoelectric actuation and power generation under high electromechanical driving levels,” PhD Thesis, Massachusetts Institute of Technology, 2002.
- [160] M. Z. Hossain and M. N. A. Chowdhury, “Ride Comfort of a 4 DOF NonLinear Heavy VehicleSuspension,” *ISESCO J Sci Technol*, vol. 8, pp. 80–85, 2012.
- [161] C. W. De Silva, F. Khoshnoud, M. Li, and S. K. Halgamuge, *Mechatronics: Fundamentals and Applications*. CRC Press, 2015.

- [162] ISO 13473-1, “Characterization of pavement texture by use of surface profiles–Part 1: Determination of mean profile depth,” *Eur Stand ICS 1714030 Eur Comm Stand Bruss.*, pp. 1-47, 1997.
- [163] K. Ahlin and N. J. Granlund, “Relating road roughness and vehicle speeds to human whole body vibration and exposure limits,” *Int. J. Pavement Eng.*, vol. 3, no. 4, pp. 207–216, 2002.
- [164] F. Tyan, Y.-F. Hong, S.-H. Tu, and W. S. Jeng, “Generation of random road profiles,” *J. Adv. Eng.*, vol. 4, no. 2, pp. 1373–1378, 2009.
- [165] A. G. Ambekar, *Mechanical vibrations and noise engineering*. PHI Learning Pvt. Ltd., 2006.
- [166] ISO 8608. “Mechanical vibration – road surface profiles – reporting of measured data”. Geneva, Switzerland: ISO, pp. 1-36, 1995.
- [167] L. He, G. Qin, Y. Zhang, and L. Chen, “Non-stationary random vibration analysis of vehicle with fractional damping,” in *2008 international conference on intelligent computation technology and automation (ICICTA)*, vol. 2, pp. 150–157, 2008.
- [168] X. Chen and Y. Zhou, “Modelling and analysis of automobile vibration system based on fuzzy theory under different road excitation information,” *Complexity*, vol. 2018, pp. 1-9, 2018.
- [169] C. S. Namuduri, Y. Li, T. J. Talty, R. B. Elliott, and N. McMahon, “Harvesting energy from vehicular vibrations using piezoelectric devices,” US patent 8143766B2, GM Global Technology Operations LLC, 2012.
- [170] X. Wang, *Frequency analysis of vibration energy harvesting systems*. Academic Press, 2016.

List of Publications

- [1] D. Al-Yafeai, T. Darabseh, and A.-H. I. Mourad, "Quarter vs. Half Car Model Energy Harvesting Systems," in *2019 IEEE Advances in Science and Engineering Technology International Conferences (ASET)*, pp. 1–5, 2019. doi: 10.1109/ICASET.2019.8714433.
- [2] D. Al-Yafeai, T. Darabseh, A.-H. Mourad, "Energy Harvesting from Car Suspension System Subjected to Random Excitation," in *2020 IEEE Advances in Science and Engineering Technology International Conferences (ASET)*, pp. 1–5, 2020. (Accepted for Publishing).